Towards satellite-assisted quantum communication with reconfigurable networks and frequency-bin qubits

by

Stéphane Vinet

A thesis
presented to the University of Waterloo
in fulfillment of the
thesis requirement for the degree of
Doctor of Philosophy
in
Physics (Quantum Information)

Waterloo, Ontario, Canada, 2025

© Stéphane Vinet 2025

Examining Committee Membership

The following served on the Examining Committee for this thesis. The decision of the Examining Committee is by majority vote.

External Examiner:	Liang Jiang Professor, Department of Molecular Engineering, Pritzker School of Molecular Engineering, University of Chicago
Supervisor(s):	Thomas Jennewein Adjunct Faculty, Dept. of Physics & Astronomy, University of Waterloo, Professor, Dept. of Physics, Simon Fraser University
Internal Member:	Norbert Lütkenhaus Professor, Dept. of Physics & Astronomy, University of Waterloo
Internal-External Member:	Michal Bajcsy Associate Professor, Dept. of Electrical and Computer Engineering, University of Waterloo
Other Member(s):	Graeme Smith Associate Professor, Dept. of Applied Mathematics, University of Waterloo

Author's Declaration

This thesis consists of material all of which I authored or co-authored: see Statement of Contributions included in the thesis. This is a true copy of the thesis, including any required final revisions, as accepted by my examiners.

I understand that my thesis may be made electronically available to the public.

Statement of Contributions

I am the sole author of Chapters 1 and 6 which were written under the supervision of Prof. Thomas Jennewein. Chapters 2 to 5 of this thesis are based on, respectively, references [1, 2, 3, 4]. Chapter 5 is the result of a collaboration with the Università di Pavia. Below, I outline my contributions to these works.

Research presented in Chapter 2:

Based on work published in:

[1] **S. Vinet**, R. Tannous, T. Jennewein, 2025: "A reconfigurable entanglement distribution network suitable for connecting multiple ground nodes with a satellite", EPJ Quantum Technol. 12, 8 .

- All authors contributed to the network architecture design. I performed all of the numerical analysis, drafted the manuscript and implemented the referee revisions.

Research presented in Chapter 3:

Based on work published in:

[2] **S. Vinet**, D. England, C.-Q. Xu, T. Jennewein, 2025: "Demonstration of a reconfigurable ground to space quantum networking scheme", arXiv:2506.00194

- Thomas Jennewein and I conceived the design of the quantum network architecture. I developed the experimental setup, I performed the data acquisition and analysis, and I drafted the paper. All authors contributed to the integrated source design and revisions to the manuscript.

Research presented in Chapter 4:

Based on work published in:

[3] **S. Vinet**, W. Wu, Y. Zhang, T. Jennewein, 2025: "Feasibility study of frequency-encoded photonic qubits over a free-space channel", Opt. Express 33, 40437-40449.

- All authors contributed to the experimental design. Jeongwan Jin built the field widened interferometer while I constructed the remainder of the experimental setup. I performed the experiments with the assistance of Wilson Wu and Yujie Zhang. I analyzed the results and wrote the manuscript. All authors reviewed the paper.

Research presented in Chapter 5:

Based on work published in:

[4] **S. Vinet**, M. Clementi, M. Bacchi, Y. Zhang, M. Giacomin, L. Neal, P. Villoresi, M. Galli, D. Bajoni & T. Jennewein, 2025: "Time-resolved certification of frequency-bin entanglement over multi-mode channels", arXiv:2508.10200

- Yujie Zhang, Thomas Jennewein, Daniele Bajoni, Matteo Galli, Marco Clementi and I conceived the time-resolved detection scheme and experimental idea. I designed and developed the interferometers at the University of Waterloo with assistance from Massimo Giacomin, Luke Neal and Kaylee Sherk. The interferometers were then shipped to the lab of Profs. Matteo Galli and Daniele Bajoni in Pavia, where Marcello Bacchi and Marco Clementi developed the entangled photon source. Marco Clementi, Marcello Bacchi, Massimo Giacomin and I performed the experiments. I performed the data analysis with the assistance of Yujie Zhang. I wrote the paper draft with the help of Yujie Zhang and Marco Clementi.

Abstract

The development of quantum networks will enable advanced applications in quantum cryptography, quantum-enhanced metrology, and quantum computing. Central to this vision is the ability to reliably distribute quantum entanglement between distant nodes. To date, quantum networks have been largely confined to metropolitan scales and a small number of nodes with predominantly static implementations, constraining their scalability and adaptability for broader deployment. Satellites provide a promising platform for distributing entanglement over global distances. However, the integration of satellites into terrestrial quantum networks poses significant challenges, including intermittent connectivity and high link attenuation during orbital passes.

In this thesis, we first propose a reconfigurable quantum network architecture that dynamically adapts its topology according to satellite availability. This reconfiguration ensures efficient and continuous operation while accommodating satellite links within a metropolitan quantum network. We demonstrate this network architecture, using a correlated photon source specifically designed for Canada's Quantum Encryption and Science Satellite (QEYSSat) mission. Using both frequency and time multiplexing, we demonstrate a linear performance improvement with minimal resource overhead. Moreover, we propose an integrated source design to facilitate deployment in realistic scenarios.

Second, we investigate frequency-encoded quantum communication over free-space channels. We propose a novel approach that leverages linear interferometry and time-resolved detectors to decode frequency-bins without any adaptive optics or modal filtering. Furthermore, we investigate the phase stability requirements so that frequency-bin encoding could be feasible for satellite to ground quantum links. A proof-of-concept experiment is conducted over a turbulent free-space channel.

Third, we distribute frequency-bin entangled photons over multi-mode channels and test their non-local correlations. We report, to the best of our knowledge, the first measurement of the joint temporal intensity between frequency-bin entangled photons revealing a rich temporal structure. By combining time-resolved detection with energy-correlation measurements, we perform full quantum state tomography and further certify our source's non-classicality via a violation of the time-energy entropic uncertainty relations. We extend this scheme to higher-dimensional frequency-bin states, opening new possibilities for high-capacity robust quantum communication and quantum information processing.

The concepts, protocols, and experimental demonstrations presented in this thesis establish new approaches to utilize frequency-bin entanglement and contribute to the development of satellite-assisted quantum networks thus paving the way towards the realization of a global quantum network.

Acknowledgements

First and foremost, I would like to express my deepest gratitude to my supervisor, Prof. Thomas Jennewein, for his invaluable mentorship over the past four years. Thank you, Thomas, for your guidance, support, and encouragement throughout my graduate studies.

I am also sincerely grateful to my Advisory Committee—Prof. Norbert Lütkenhaus, Prof. Michael Reimer, and Prof. Jon Yard—for their insightful feedback and thoughtful discussions. I thank Prof. Michal Bajcsy and Prof. Graeme Smith for kindly agreeing to serve on my Examining Committee on short notice, and Prof. Liang Jiang for serving as the external examiner of my defense.

To the past and present members of the Quantum Photonics Laboratory, thank you for your collaboration, discussions, and technical advice over the years. Special thanks to my office mates, Ramy Tannous and Wilson Wu, for fostering such a supportive and enjoyable work environment. Ramy, thank you for patiently teaching me how to align lasers and for being a constant source of encouragement. Wilson, I have thoroughly enjoyed our wide-ranging conversations, from quantum physics to finance to everyday life. I was fortunate to collaborate with Yujie Zhang on frequency-encoded quantum communication. Thank you, Yujie, for many helpful discussions and your feedback.

I would like to gratefully acknowledge Julien Beaudoin-Bertrand, from Spectra-Physics, for his generous help with the Tsunami laser.

To my friends in Montreal, thank you for your curiosity about my work, for listening to my stories about lasers and quantum mechanics, and for your encouragement. Despite the distance, your constant support made it feel like you were never far away.

I gratefully acknowledge the financial support that allowed me to fully focus on my research: the NSERC Canadian Graduate Scholarship and the University of Waterloo President's Graduate Scholarship.

I would also like to thank Prof. Matteo Galli and Prof. Daniele Bajoni for welcoming me into their research group during my visit to Pavia. I had the pleasure of working with Marco Clementi and Marcello Bacchi, from whom I learned a great deal about integrated frequency-entangled photon sources and microring resonators. I am thankful to Massimo Giacomin for his dedication and assistance with the alignment of the field-widened interferometers, both in Waterloo and in Pavia.

To Sarah Kordlouie, thank you for your love, patience, and steadfast support—you are my rock.

Finally, none of this would have been possible without the unconditional love and encouragement of my family. Thank you to my parents, Luc and Letitia, my siblings, Jean-François, Laurent, and Sophie-Andrée, and our beloved dog, Zoé.

Dedication

À ma famille.

Table of Contents

Examining Committee ii

Author's Declaration iii

Statement of Contributions iv

Abstract vi

Acknowledgements vii

Dedication ix

List of Figures xiv

List of Tables xxi

List of Abbreviations xxiii

1 Introduction 1

1.1 Quantum networks 1

1.1.1 Quantum channels 2

1.1.2 Satellite-based quantum communication 2

1.2 Quantum network benchmarking 4

1.3 Quantum Key Distribution 5
1.3.1 Prepare-and-measure quantum key distribution 6
1.3.2 Entangled-based quantum key distribution 7
1.4 Outline 9

2 A reconfigurable entanglement distribution network suitable for connecting multiple ground nodes with a satellite 12
2.1 Introduction 12
2.1.1 Multiplexing and hyper-entanglement 13
2.2 Network architecture 15
2.3 Performance estimation 18
2.3.1 Quantum Encryption and Science Satellite mission 22
2.4 Summary 25

3 Demonstration of a reconfigurable ground to space quantum networking scheme 27
3.1 Introduction 27
3.2 Experimental setup 28
3.2.1 Materials and methods 29
3.2.2 An alternative frequency-to-time mapping 31
3.3 Experimental results 33
3.4 Discussion 37
3.4.1 Scaling potential 37
3.4.2 Integrated source design 38
3.5 Summary 39

4 Frequency-encoded quantum communication 41
4.1 Motivation 41
4.2 Theory 43

4.2.1 Frequency-bin encoding . . . 43
4.2.2 Timing jitter . . . 47
4.2.3 Moving platforms . . . 48
4.3 Field-widened interferometers . . . 51
4.4 Proof-of-concept demonstration . . . 54
4.5 Conclusion . . . 59

5 Entanglement-based frequency-bin quantum communication 60
5.1 Time-resolved detection scheme . . . 60
5.1.1 Preliminary: joint temporal intensity measurement . . . 61
5.1.2 Preliminary: interferometric σ_Z-basis measurement . . . 62
5.2 Experimental setup . . . 64
5.2.1 Interferometric alignment . . . 66
5.3 Source characterization . . . 67
5.3.1 Equatorial basis measurement . . . 67
5.3.2 $\sigma_Z\sigma_Z$-basis . . . 71
5.3.3 Cross-basis (Equatorial-σ_Z-basis) . . . 73
5.4 Results . . . 75
5.4.1 Quantum State Tomography . . . 75
5.4.2 Steering inequality and entropic uncertainty relation . . . 76
5.4.3 Quantum Key Distribution . . . 78
5.5 Summary and outlook . . . 79

6 Conclusions 82
6.1 Summary of results and research outlook . . . 82

References 86

APPENDICES 121

A Quantum Key Distribution Simulation **122**

A.1 Squashing model 122

A.2 Secure key rate calculation 124

B Joint Spectral Intensity Simulation **127**

C Interferometric demultiplexing **131**

C.1 MZI frequency demultiplexing 131

D Frequency-bin post-processing (prepare-and-measure scheme) **133**

E Estimation of multi-mode characteristics **137**

E.0.1 Modal decomposition analysis code 139

F Frequency-bin post-processing (entanglement-based scheme) **142**

List of Figures

2.1 Conceptual sketch for wavelength division multiplexing as described in Eq. 2.2. Each color-coded EPS corresponds to a single correlated frequency channel. 14

2.2 (a) Communication layer and wavelength allocation for a satellite pass over two ground stations e.g. over Waterloo and Montreal. (b) Waterloo is in view of the satellite and takes the multipoint-to-point satellite pass configuration whereas Montreal is in a fully connected ground topology (c). At a later time, with the satellite now in view of Montreal, the two cities will adopt the opposite topology by redistributing the frequency-time correlated pairs $\{\lambda_i, \Lambda_i\}$ between the nodes. During the satellite pass Alice and Bob are connected by two frequency-time channels and thus enjoy a higher key rate. 15

2.3 Conceptual physical layout of the hybrid quantum network. The EPS consists of a nonlinear crystal (NC) pumped by a pulsed laser to create entangled photon pairs via spontaneous parametric down-conversion. During the satellite pass (flip mirror (FM) up) the signal is sent through a frequency-to-time encoder $\tau(\lambda)$ in an uplink to the satellite (Sat) via the OGS. Outside of the satellite pass (flip mirror down) the signal is rerouted with the idler through telecom fibre to the various ground nodes thus enabling a fully connected topology. 17

2.4 Scaling behaviour of the ground-to-satellite QKD scenarios for (a) with the time-frequency mapping. The time and frequency multiplexing leads to a linear key rate improvement. (b) Without the $\tau(\lambda)$ frequency-to-time encoder, there is no discrimination made between the wavelength channels jointly recorded at the satellite resulting in an increase in accidental counts and reduction in key rate. The squeezing parameter χ in Eq. 2.3 was optimized for every channel setting to maximize the SKR as shown in Fig. 2.6b. Realistic detector parameters were considered and can be found in Table 2.2. 21

2.5 Initial proposal for the physical layout of the hybrid quantum network. The EPS is pumped by a continuous-wave laser and the idler photons are frequency demultiplexed to the ground nodes. Without the FTM no temporal discrimination is possible at the satellite node. 21

2.6 Optimized squeezing parameter for (a) a symmetric link where $\eta_s = \eta_i$ and (b) an antisymmetric link where the satellite link loss is fixed $\eta_s = 40$. The remaining simulation parameters were chosen in accordance with Table 2.2. 22

2.7 Secure key rate performance comparison between PNR and Bucket detectors for the ground user nodes. The simulation parameters considered can be found in Table 2.2. 23

2.8 The spectrum of the signal (a) and the idler (b) were calculated from the Sellmeier equations for PPLN assuming a 2 nm pump bandwidth centered at 521.4 nm and a 15 mm crystal [5]. Wavelength correlated pairs $\{\lambda_i, \Lambda_i\}$ are denoted by the same color in both spectrums and were chosen in accordance with Fig. 2.2. The idler channels match the ITU DWDM 100 GHz grid. . 24

2.9 Scaling behaviour of the ground configuration (Fig. 2.2c) for the QEYSSat compatible scenario considered in Table 2.3 with the detector parameters given in Table 2.2. 25

3.1 Experimental implementation of the reconfigurable quantum network for **(a)** the satellite configuration and **(b)** the ground configuration. A PPLN waveguide was pumped by a pulsed laser with a repetition rate of 80 MHz to create highly correlated photon pairs via type-0 spontaneous parametric down conversion. During a satellite pass, a frequency-to-time mapping is implemented using a fibre Bragg grating array as a dispersive component. Outside of the satellite pass, an active switch reconfigures the network into a three node ground network formed via wavelength division multiplexing. In both scenarios, the idler is frequency demultiplexed using off-the-shelf telecommunication components such as optical circulators and fibre Bragg gratings. To emphasize the differences between the two configurations, optical elements not used in each configuration are depicted in grey. The quantum correlation layer for each scenario is respectively shown in **(c)** and **(d)**. (SHG: second-harmonic generation, DM: dichroic mirror, HWP: Half-wave plate, BPF: band-pass filter, WG: waveguide, LPF: long-pass filter, Circ: circulator, FBG: fibre Bragg grating, SNSPD: superconducting nanowire single photon detector, Si-APD: silicon avalanche photodetector) 30

3.2 The measured spectrum of the signal **(a)** and idler **(b)** photons. Wavelength correlated channels are denoted with the same color in both spectrums. 1 nm guard bands are used between the signal channels to minimize cross-talk between the channels. 31

3.3 Photographs of the waveguide coupling stage. (a)-(b) The waveguide coupling setup. (c) An image of the input fibre-waveguide coupling taken with the Leica M125 C stereo microscope. 32

3.4 Photograph of the idler demultiplexing stage. 33

3.5 (a) Alternative implementation of the frequency-to-time mapping in free-space (b) Angle of incidence required to align a narrowband bandpass filter with central wavelength 522.125 nm and 0.25 nm bandwidth to each of the four wavelength channels spanning 520.5 nm to 522.25 nm. 34

3.6 Multiplexing scheme performance estimation. In **(a)**, the coincidence-to-accidentals ratio is measured as a function of the pump power. In **(b)**, **(c)**, and **(d)** the two-photon interference visibility, QBER, and secure key rate are respectively estimated from the measured CAR. For the ground DEMUX scenario shown in **(a)**, coincidences at low pump power were measured using a SNSPD and APD detector per user, due to the SNSPD's poor detection efficiency at 780 nm. At higher pump power, signal and idler photons were jointly detected on a single SNSPD channel per user. 36

3.7 Trade-off between the number of frequency-time multiplexed channels and the repetition rate. 37

3.8 Schematic for the proposed integrated networkable quantum source. . . . 38

3.9 Simulated joint spectrum intensity (JSI) for the entangled photon source depicted in Fig. 3.8. Each JSI represents the spectral correlations between signal and idler photons for a specific frequency-time channel. 40

4.1 Multi-mode frequency-bin analyzer. The MM fibre input provides increased coupling efficiency and enhanced robustness to pointing errors and distorted point spread functions. 42

4.2 Dual-rail logical qubit encoding: a single photon corresponds to $|0\rangle$ or $|1\rangle$ depending on which frequency mode it occupies. 43

4.3 Frequency-bin encoding. Photons are encoded in spectral bands $|\omega_0\rangle$ ($|\omega_1\rangle$) with bandwidth σ_0 (σ_1) separated by $\Delta\omega$. For $\langle\omega_0|\omega_1\rangle = 0$, $|\omega_0\rangle$ ($|\omega_1\rangle$) correspond to logical bits $|0\rangle_L$ ($|1\rangle_L$). 46

4.4 (a) Poincaré sphere. The time dependence, described in Schrödinger picture, $|\Psi(t)\rangle = \frac{1}{\sqrt{2}}(|\omega_0\rangle + e^{i\Delta\omega t}|\omega_1\rangle)$ leads to an oscillation around the equator at angular velocity $\Delta\omega = \omega_1 - \omega_0$ as depicted at times $t = 0$ and $t = \tau$. 47

4.5 Limitations on the beat note visibility due to (a) the beat note's frequency spacing for a fixed timing resolution of 100 ps, (b) the detector's time jitter for a fixed frequency spacing of 260 MHz. We assume a laser linewidth of 300 kHz [6], and a visibility of 95% at $\Delta t = 0$. 49

4.6 (a) Relay-optics enhanced and (b) field-widened interferometer designs. For the former a $4f$ imaging system in each arm reproduces the field mode at the same position in each arm thus removing the path distinguishability. For the latter, a 10 cm BK7 glass rod is used to compensate for spatial distortions of the optical mode of the frequency-bin qubit. In both cases, the interferometer performs the σ_Z-basis projection by demultiplexing frequencies ω_0 and ω_1. The basis choice is implemented via an optical shutter in the short arm of the interferometer. 52

4.7 Stress-induced birefringence in the glass rod. (a) Image of polarized light from a computer screen (b) same image but observed through the glass rod, revealing stress-induced birefringence along the mounting screws. 53

4.8 Polarization extinction measurement for the glass rod. (LD: laser diode, LP: linear polarizer) 53

4.9 Photographs of the (a) idler photon's frequency-bin analyzer: the FWI has a single-mode fibre input, (b) the signal photon's frequency-bin analyzer: the FWI has a multi-mode fibre input (CCR: corner cube retro-reflector). 54

4.10 Simplified experimental setup: The DL-Pro generates 780 nm light which is modulated into two frequency-bins via an AOM driven by an arbitrary waveform generator at 260 MHz. Two mechanical shutters are used to encode the frequency-bins which are spatially combined at a polarization-maintaining fibre beam-splitter and sent across a 2 meter free-space bridge to the receiver. The frequency-bin analyzer consists of a field-widened multi-mode interferometer which is used to demultiplex the frequency-bins. The basis choice at the receiver is performed via a mechanical shutter in the long arm of the interferometer. The outputs from the frequency-bin analyzer are coupled into multi-mode fibres connected to Si-APDs. A 500 kHz marker pulse from the AWG provides a time reference to the time-tagging unit. 55

4.11 Photograph of the frequency-bin generation setup. A double-pass configuration through the AOM was used to achieve a total frequency shift of 260 MHz while driving the AOM at 130 MHz. 56

4.12 (a) Frequency-bin encoding scheme. A repeated sequence $\{|\omega_0\rangle, \frac{1}{\sqrt{2}}[|\omega_0\rangle + e^{i\Delta\omega t}|\omega_1\rangle], |\omega_1\rangle, |vac\rangle\}$ is encoded via two mechanical shutters driven by squares waves $\pi/2$ out of phase. Frequency-bin decoding scheme for the rectilinear basis: $|\omega_0\rangle$ and $|\omega_1\rangle$ are measured on detectors 0 and 1 in (b) and (c) respectively. 56

4.13 Frequency-bin decoding scheme for the superposition basis. To evaluate the integrity of the quantum channel, the receiver blocks the long arm of the interferometer and measures a beat note at the photon detector. (a) If the sender prepared a state in the σ_X basis, a beat note corresponding to $\frac{1}{\sqrt{2}}[|\omega_0\rangle + e^{i\Delta\omega t}|\omega_1\rangle]$ can be observed. (b) Whenever the sender encoded in the rectilinear basis only one frequency is received and no beat note is observed. The histogram bin size corresponds to the time-tagger resolution. 58

5.1 Joint temporal intensity for (a) frequency-bin entangled photons in the ideal limit where $\gamma \ll \Delta\omega$, (b) joint temporal intensity for the classical bichromatic pump. 63

5.2 Pictorial representation of the projections for (a) the equatorial basis measurement presented in Sec 5.3.1, (b) the $\sigma_Z\sigma_Z$-basis in Sec 5.3.2 and (c)-(d) the cross-basis measurements presented in Sec 5.3.3. 63

5.3 The experimental setup is broken down into five different stages: (a) the entangled photon pair generation, (b)-(d) representing three different detection scenarios, and (e) a detailed schematic of the field-widened interferometer. (b) and (c) represent a direct detection scheme for the equatorial basis measurement where the signal is detected over single- and multi-mode fibre respectively. (d) $\sigma_Z\sigma_Z$-basis measurement: the field-widened interferometers demultiplex $|0_{s(i)}\rangle$ and $|1_{s(i)}\rangle$. 64

5.4 Experimental setup for the time-of-flight interferometric calibration. . . . 66

5.5 Time-of-flight measurement for the two MZIs. Gaussian functions were fitted to the early-early (EE), early-late (EL), late-early (LE) and late-late (LL) pulses. 67

5.6 Joint temporal intensity. (a) Theoretical JTI for $1/\gamma = 581.4$ ps, the counts were scaled to match the experimental data, (b) Measured JTI over single-mode fibre, with a fitted ringdown time $1/\gamma_{fit} = 581.3(9)$ ps^{-1}, (c) diagonal profile of the measured JTI, a biphoton temporal beating can be observed in the coincidences whereas the singles exhibit no oscillation highlighting the non-local nature of the correlations, (d) antidiagonal profile of measured JTI, the cavity lifetime leads to a double exponential decay proportional to γ. 68

5.7 Correlation function $\langle \sigma_\phi \sigma_\phi \rangle$ as a function of the absolute time τ for different relative time delays $\Delta t = t_s - t_i$. Here ϕ denotes the azimuthal angle on the equator of the Poincaré sphere. Due to the cavity lifetime, the amplitude of the oscillation decays proportional to $|t_s - t_i|$ suggesting under-corrections in our time-dependent detector modeling. The time axis spans 0 to 610 ps, corresponding to one beat period $T_b = \pi/\Delta\omega$. 69

5.8 CHSH Bell inequality for frequency-bin entangled photons. (a) Expectation values $\langle A_i B_j \rangle$, $i, j \in \{0, 1\}$ for $\Delta t = 0$, and (b) Bell parameter S as a function of detection time τ. The time axis spans 0 to 610 ps, corresponding to one beat period $T_b = \pi/\Delta\omega$. 70

5.9 $\sigma_Z\sigma_Z$-basis measurement. Counts C_{ij}, for $i, j \in \{0, 1\}$, in (a) through (d) correspond to the projections $|00\rangle\langle 00|, |01\rangle\langle 01|, |10\rangle\langle 10|, |11\rangle\langle 11|$ respectively. Note that detections C_{i1} were taken with the InGaAs APD. 71

5.10 $\langle \sigma_Z\sigma_Z \rangle(t)$: phase fluctuations in both interferometers lead to an exponential decay of $\langle \sigma_Z\sigma_Z \rangle$. 73

5.11 In (a) and (b) the equatorial-basis measurement was done with the MPD and the Z-basis measurement was done with the SM-MZI for $|0_i\rangle$ and $|1_i\rangle$ respectively. In (c) and (d) the MM-MZI implemented the Z-basis measurement (for $|0_s\rangle$ and $|1_s\rangle$ respectively) and the equatorial-basis measurement was done with an SNSPD detector. 74

5.12 Quantum state tomography. A 91(1)% fidelity to the $|\Phi^+\rangle$ state was obtained. 75

5.13 C-parameter and secure key rate calculated according to Eq. 5.14-5.16. . . 79

5.14 Simulated JTI for the qutrit projection defined in Eq. 5.17. 81

E.1 (a) Image, captured with a beam-profiling camera (WinCamD-UCD12), of the multi-mode beam in the analyzer in Fig. 4.10, after propagation through 2 meters of free space and a 1-meter long step-index multi-mode fiber (Thorlabs M43L01). (b) Reconstruction of the point spread function from modal decomposition using the first 100 Hermite-Gaussian modes. Each pixel corresponds to 5.2μm. 138

E.2 (a) Point spread function, imaged with a beam-profiling camera (*New Imaging Technologies WiDy SenS 640*), of the multi-mode beam in the analyzer in Fig. 5.3, after propagation through a 5-meter long graded-index (GRIN) multi-mode fibre (*Thorlabs GIF625*). (b) Reconstruction of the point spread function from modal decomposition using the first 30 Hermite-Gaussian modes. 139

F.1 Conceptual representation of the projectors defined in Eq. 5.3 shown overlaid on a subsection the joint temporal amplitude (JTA) in Fig. 5.6b for illustrative purposes. Each color defines a different equatorial basis considered for the quantum state tomography. 144

List of Tables

2.1 Proposed network connectivity and wavelength allocation. Wavelength correlated pairs are denoted as $\{\lambda_i, \Lambda_i\}$ for signal and idler respectively. The specific wavelengths considered in Figs. 2.8-2.9 are provided in parentheses with their associated ITU channel number. 19

2.2 Experimental assumptions for QKD modeling 20

2.3 Entangled photon source assumptions 23

2.4 Generated key rate over a one-month period for both network configurations 26

4.1 Detector models used in Fig. 4.5b and their corresponding nominal full width at half maximum (FWHM) timing resolution (δt^{FWHM}). The MPD and Excelitas detectors were used in pair with a UQD Logic16 time-tagger with a resolution of 78.125 ps [7]. A conservative upper bound for the timing resolution of the LeCroy waveRunner 640Zi used in combination with a LeCroy OE425 [8] is provided. The total resolution of the detection system (δT^{FWHM}) is estimated from the summation in quadrature of each component. 50

4.2 Comparing satellite-based quantum protocols using different degrees of freedom (DOF), sensitivity quantifies how fast the compensation scheme should be. 50

4.3 Experimental parameters for the prepare-and-measure demonstration. . . 59

5.1 $\sigma_Z\sigma_Z$ measurement statistics. The counts were normalized by the channel efficiency and the integration time was 60 seconds. A detailed breakdown of the channel losses is given in Table 5.2. 72

5.2 Channel efficiencies for the σ_Z-basis measurements. 72

5.3 Quantum state tomography fidelities, purities and CHSH S-parameters obtained using equatorial basis measurements performed over single-mode or multi-mode fibre. All remaining basis measurements were performed over multi-mode fibre in both configurations as depicted in Fig. 5.3d. 76

5.4 Steering inequality violation for the single-mode and multi-mode channels. Note that the $\langle \sigma_Z \sigma_Z \rangle$ was measured in both scenarios using the InGaAs APD detector. 77

5.5 Entropic uncertainty relation for the single-mode and multi-mode channels. Note that the $H(\sigma_Z^s \mid \sigma_Z^i)$ was measured in both scenarios using the InGaAs APD detector. 78

List of Abbreviations

AOI angle of incidence 31–33, 51, 57

APD Avalanche Photodetector 57, 65, 66, 70

AWG arbitrary waveform generator 55

BPF bandpass filter 31–33

CAR coincidence-to-accidental ratio 33–35, 65, 70, 73, 84

CFBG chirped fibre Bragg grating 16

CHSH Clauser–Horne–Shimony–Holt 7, 8, 69, 79

CSA Canadian Space Agency 3

EOM electro-optic modulator 64, 83

EPS entangled photon source 13, 41, 83, 84

FBG fibre Bragg grating 16, 29, 31

FFT Fast Fourier Transform 137

FTM frequency-to-time mapping 14, 28, 29, 31–33, 38, 39

FWHM full width at half maximum 61

FWI field-widened interferometers 9, 51, 84

GDD group delay dispersion 14, 16

GPS Global Positioning System 50

InGaAs indium gallium arsenide 65, 66, 70

ITU International Telecommunication Union 23, 65, 83

JSI joint spectral intensity 39, 127

JTA joint temporal amplitude 143

JTI joint temporal intensity 10, 60, 62, 67, 73, 80

LEO low Earth orbits 2, 49, 50

LOQC linear optical quantum computation 83, 84

LP linear polarizer 52

MM multi-mode 42

MZI Mach-Zehnder interferometer 42, 44–46, 51, 55, 61, 66, 131, 132

OGS optical ground station 24

OPL optical path length 31, 32, 51, 52, 66, 131

PDC parametric down-conversion 19

PNR photon-number resolving 18, 22

PPLN periodically poled magnesium-oxide doped lithium niobate 22, 27–29, 39

PSF point spread function 137, 139

QBER quantum bit error rate 7, 18, 20, 22, 34, 78

QEYSSat Quantum Encryption and Science Satellite 3, 10, 15, 22, 23, 25, 27, 28, 37, 83

QKD quantum key distribution 1, 3, 5, 6, 9, 34, 78, 122

QMAN quantum metropolitan-area networks 15, 16, 82

QPL Quantum Photonics Laboratory 9

RFI reference frame independent 9, 78, 79

Si-APD Silicon Avalanche Photodetectors 16, 19, 23, 28, 54

SiN silicon nitride 10, 84

SKR secure key-rate 19, 20, 34

SLR Satellite Laser Range 50

SLSQP sequential least squares programming 20, 126

SNSPD superconducting nanowire single-photon detector 19, 28, 35, 65, 66, 69, 83

SPDC spontaneous parametric down-conversion 13, 18, 25, 28, 33, 39, 122

SWaP size, weight, and power 42, 60, 78, 85

TDM time division multiplexing 13, 82

TFGKP time-frequency Gottesman-Kitaev-Preskill 84

TOF time of flight 66

WCPs weak coherent pulses 7

WDM wavelength division multiplexing 13, 28, 31, 38, 82

Chapter 1

Introduction

A significant research undertaking in the field of quantum technologies is the creation of a global communication network known as the *Quantum Internet* [9, 10]. The distribution of quantum resources through such a network enables exciting new applications in quantum communication [11, 12], distributed quantum computing [13, 14], and quantum sensing [15, 16]. In this chapter, we briefly review its history, focusing on results relevant to this thesis.

1.1 Quantum networks

The history of quantum communication dates back to Stephen Wiesner's seminal work [17] in the 1970s, which showed how quantum mechanical principles could be exploited to produce an uncounterfeitable currency [18]. Building upon Wiesner's *quantum money*, Charles Bennett and Gilles Brassard proposed a quantum key distribution (QKD) protocol in 1984 [11, 19]. These pioneering contributions established the theoretical basis for information-theoretically secure quantum communication and initiated the development of quantum networking schemes.

During the past three decades, several experimental advances have validated and expanded these theoretical frameworks [20, 21, 22, 23, 24, 25]. Early milestones include demonstrations of quantum key distribution [24, 26, 27], quantum teleportation [20, 21], entanglement swapping [28, 22, 29], and preliminary field implementations of quantum networks [25, 30, 31]. Commercial grade QKD systems now operate across metropolitan fibre networks [32, 33, 34], while free-space quantum communication has been demonstrated over

significantly longer distances [35, 36, 37, 38]. The 2016 launch of China's Micius satellite enabled landmark demonstrations of satellite-based intercontinental quantum key distribution and entanglement distribution [39, 40, 41, 42, 43]. However, there are still significant technical obstacles in the way of implementing quantum networks [10, 44, 45]. In contrast to classical information, the no-cloning theorem [46] prevents quantum information from being duplicated. While the no-cloning theorem underpins the security of quantum cryptography, it makes signal attenuation and decoherence particularly restrictive for extended quantum transmission distances.

1.1.1 Quantum channels

A quantum network requires coherent quantum information transfer between stationary qubits at distant quantum nodes. These nodes are connected via flying qubits using photons as information carriers. Photons are transmitted over optical fibres or free-space. In a lossy propagation medium, the channel transmission efficiency scales exponentially as $\eta = O(e^{-\alpha d})$, where α is the medium's attenuation coefficient and d the communication distance. In standard telecommunications optical fibre [47], $\alpha \approx 0.2$ dB/km at a wavelength of 1550 nm, primarily due to photon absorption and scattering losses. This exponential loss constrains fibre-based quantum networks to metropolitan-scale distances [48, 49, 50]. Free-space channels, where light propagates in the air, exhibit modest attenuation (e.g. on the order of 0.1 dB/km at 1 atmosphere pressure for 785 nm [51]). The propagation medium (predominantly vacuum), provides space-based quantum networks with an inherent advantage compared to ground-based networks [52]. The principal mechanism of loss arises from beam divergence: when the beam spot exceeds the receiving aperture, the fraction of the optical field outside the detector is effectively lost [45]. Thus, through free-space the channel efficiency scales quadratically $\eta = O(\frac{1}{d^2})$, which is far more favourable than the exponential scaling encountered in fibre.

1.1.2 Satellite-based quantum communication

Satellite-enabled quantum communication offers favourable loss scaling, however, it presents significant engineering challenges such as atmospheric turbulence, pointing errors, background light, and limited availability. To date, only a handful of quantum satellites are currently operational [39, 53, 54, 55] or are planned for future deployment [56, 57, 58, 59]. Most of these satellites operate in Sun-synchronous low Earth orbits (LEO) providing a visibility window at a given optical ground station of only a few minutes per day. Quantum

satellite constellations have been proposed as a solution to provide continuous global coverage [60, 61, 62]. Yet, such a constellation remains a daunting prospect as it would require the deployment of hundreds if not thousands of individual satellites [45, 60]. While the technical intricacies remain unclear, a vision for the realization of the Quantum Internet is taking shape. It will be a heterogeneous network of quantum processing units (QPUs) connected through intra-city sub-networks over fibre, with inter-city connections using a fibre backbone and quantum repeaters [63, 64, 65] and ultra-long distance communication established via satellite links [66, 67].[1] It is therefore crucial to efficiently integrate quantum satellites with the optical fibre network on the ground to enable a practical global Quantum Internet.

Quantum Encryption and Science Satellite

The Quantum Encryption and Science Satellite (QEYSSat) mission, funded by the Canadian Space Agency (CSA), aims to demonstrate long distance QKD and entanglement distribution in an uplink configuration where photons are transmitted from ground to satellite. The QEYSSat science team, at the University of Waterloo, has been developing quantum light sources and a quantum optical ground station. Uplink configurations, such as QEYSSat, offer many practical advantages, including reduced onboard complexity and the ability to test a range of quantum light sources from the ground. Furthermore, in this configuration, quantum signals can be rerouted through terrestrial infrastructure whenever the satellite is unavailable, thereby enabling more efficient resource allocation for the source and network provider. While spatial mode geometry is well preserved in optical fibres, free-space links are subject to distortions arising from atmospheric effects [51]. Several design considerations must thus be taken into account to ensure the seamless integration of satellite links within ground-based quantum networks. Notably, the QEYSSat optical payload accepts uplink signals between 780 and 795 nm [51, 68]. This wavelength range was chosen for high atmospheric transmission, compatibility with existing single-photon sources, and high-efficiency space-ready detectors [69]. Another important factor is the physical degree of freedom used for encoding quantum information. For its primary mission, QEYSSat functions as a trusted node receiver that measures four linear polarization states in two mutually unbiased bases [70, 71]. However, polarization encoding is generally unsuitable for long-distance fibre transmission. Stress-induced birefringence, environmental perturbations, and imperfections in fibre geometry or optical components, lead to polarization rotations, polarization mode dispersion, and polarization-dependent loss that degrade the

[1] For a more detailed overview of the required components, challenges, and roadmap toward a *Quantum Internet*, the reader is encouraged to consult Refs. [9, 10, 45].

fidelity of the transmitted state [72, 73]. Addressing these issues requires active polarization tracking and fast compensation systems [74]. Consequently, alternative degrees of freedom, intrinsically insensitive to polarization fluctuations, such as time-bin encoding, are generally preferable for fibre-based quantum communication [75, 76]. Careful consideration of these constraints is essential when designing scalable network architectures.

1.2 Quantum network benchmarking

There is no universal standard for evaluating quantum network performance, as the usefulness of a given architecture varies significantly depending on the target application. Nevertheless, several key metrics can provide insight into a network's utility:

1. **Number of nodes:** One key metric for assessing a network's functionality and connectivity is the number of connected nodes. Metcalfe's law states that the utility of a classical network increases quadratically with the number of nodes in the network [77]. More specifically, a network's value can be quantified economically via the users' willingness to pay for the applications enabled by connecting people and devices, forming a system whose overall utility is more than the sum of its parts. Quantum networks similarly benefit from additional nodes through more complex network topologies, multi-party protocols and increased quantum computing power. Expanding beyond point-to-point links remains a major goal towards scalable quantum networks.

2. **Geographical scale:** The Quantum Internet envisions a global quantum network. The capacity to span long distances is essential for implementing applications such as global quantum key distribution, quantum clock synchronization [78], and quantum-enhanced long baseline telescopy [15]. The physical extent of a quantum network is thus an important parameter to consider when evaluating its performance. Note that, a network's range is typically reported alongside an entanglement distribution rate. The two values being intrinsically tied by the channel's efficiency and described via a *entanglement distribution rate region* [77].

3. **Heterogeneity:** As discussed in section 1.1.2, a scalable quantum network must support heterogeneity across various levels: quantum nodes, communication channels, and network topologies. This encompasses the capacity to combine various quantum hardware platforms such as solid-state emitters, superconducting qubits and trapped ions into a single network. Significant research efforts are underway to ensure smooth

interoperability between these modalities through efficient quantum interfaces and transduction mechanisms [79, 80, 81]. Additionally, in order to accommodate various use cases and deployment restrictions, a scalable quantum network must support different topologies and hybrid architectures.

4. **Resource cost:** The economical cost is another important consideration. Resource-efficient architectures that optimize quantum channel usage and reduce hardware redundancy are more viable for real-world implementations. Consequently, it is essential to minimize resource overhead and device complexity.

5. **Security level:** In principle, quantum key distribution is said to provide information-theoretic security. Practically, trust assumptions between the device performance and the theoretical model determine the security level of the protocol. A protocol is said to be ϵ-secure if the probability it behaves differently from a perfect device is at most ϵ [82]. When designing a quantum network, several vulnerabilities such as side-channel attacks [83, 84, 85, 86], resistance to eavesdropping, and trusted nodes must be taken into account.

6. **Uptime:** The availability of the network is a fundamental indicator of overall performance. The uptime is particularly relevant when discussing satellite-enabled quantum networks due to their sparse availability.

As QKD remains the most near-team application of quantum networks, its secure key rate is often used to assess the performance of a quantum network architecture. In the following section 1.3 we briefly review prepare-and-measure and entanglement-based quantum key distribution.

1.3 Quantum Key Distribution

Classical encryption schemes are founded on the assumption that certain mathematical operations are difficult to invert. However, the rapid advancement of computational power, in particular the advent of quantum computers, poses a serious threat to the security of such encryption methodologies [87]. Quantum key distribution harnesses quantum mechanical principles to provide, in principle, information-theoretic security i.e. security against adversaries with unlimited computing resources and time [88]. Quantum cryptography leverages several quantum mechanics phenomena, including the inherent randomness of quantum measurements and the no-cloning theorem [89]. In practice, the security of the

protocol's implementation depends on assumptions made about the physical devices, which are often assumed to be flawless. However, realistically, these devices are imperfect, leading to deviations from the idealized model assumed in the security proof. The *implementation security* analyzes the gaps between the actual device, the quantum optical model and the security proof to rectify any discrepancies that might weaken the security of the protocol [90, 91].

QKD protocols are typically divided into two families: prepare-and-measure (PM) and entanglement-based (EB) schemes. While the *source-replacement scheme* [92, 93] provides an equivalence between PM and EB schemes from a security perspective (thus simplifying the analysis of the former), their physical implementation can differ drastically. In both scenarios, two remote users, traditionally named Alice and Bob, want to generate a secure key that can then be used to protect their communication from an eavesdropper, usually called Eve [89, 94]. We follow the security definition given in [82] where a protocol is said to be $\epsilon-$secure if the trace distance between the output state and the ideal state is less than ϵ, i.e. $\frac{1}{2}||\rho_{KE}^{\text{real}} - \rho_{KE}^{\text{ideal}}||_1 \leq \epsilon$, where $\rho_{KE}^{\text{ideal}} = \frac{1}{|\mathcal{S}|}(\sum_{s\in\mathcal{S}} |s\rangle\langle s| \otimes |s\rangle\langle s|) \otimes \rho_E$ and $\rho_{KE}^{\text{real}} = \sum_{s,s'\in\mathcal{S}} p(s,s')\big(|s\rangle\langle s| \otimes |s'\rangle\langle s'| \otimes \rho_E^{s,s'}\big)$. More intuitively, the ideal output of the QKD protocol has the following properties:

1. $K_A = K_B$, where K_A and K_B denote Alice and Bob's keys, respectively
2. All keys must be equally likely, in other words K is uniformly distributed $p(K) = \frac{1}{|K|}$
3. Eve is uncorrelated from the key.

1.3.1 Prepare-and-measure quantum key distribution

For PM schemes such as BB84, the procedure is as follows.

1. Alice prepares single-photon quantum states in different polarization or phase states and sends them over the quantum channel to Bob.
2. Bob then performs measurements in mutually unbiased randomly selected bases.
3. Once the photon transmission phase of the protocol is complete, Alice and Bob reveal their prepare-and-measure bases, respectively, for every round of the protocol by communicating over a classical authenticated channel. They then keep the results of the photon exchange only if the preparation and measurement basis was the same.

4. Alice and Bob then compare a subset of the resulting sifted key to perform the parameter estimation. In this step, they test a random subset of the sifted key e.g. by estimating the quantum bit error rate (QBER). Supposing the measured QBER is above a pre-defined threshold, determined by the parameters of the protocol, an eavesdropper (Eve) is assumed to be strongly correlated to the sifted key and the protocol is aborted.

5. Otherwise, Alice and Bob proceed with classical post-processing steps including error correction and privacy amplification.

In PM schemes, the security arises from the notion that the measurement changes the quantum states i.e. the eavesdropper's inability to measure non-orthogonal states without introducing detectable errors which lead to the abortion of the protocol. Note that while the protocol requires single-photon sources, it is usually implemented using attenuated lasers that produce weak coherent pulses (WCPs). WCPs offer easy implementation and fast operation speed. However, they are vulnerable to photon-number splitting [95] and side-channel attacks [96, 97, 98] that reduce the secure key rates. Decoy-state protocols largely mitigate the effect of these attacks, for a more detailed discussion, the reader is encouraged to consult Refs.[99, 100, 101].

1.3.2 Entangled-based quantum key distribution

In 1991, Artur Ekert proposed a novel protocol that directly uses entanglement to establish a secret key between Alice and Bob [12]. In EB protocols, a source generates entangled photon pairs and distributes them to Alice and Bob. Contrary to PM schemes, here we assume that Eve prepares some arbitrary state ρ_{ABE}, where the A and B systems are made of N qubits. Eve distributes system A and B to Alice and Bob, respectively, and keeps system E for herself. Alice and Bob each measure their respective N qubits in a randomly selected basis. Alice and Bob pick a random subset of the N rounds of the protocol and test the correlations between their measurement results. In practice, for the E91 protocol, this test is implemented using the Clauser–Horne–Shimony–Holt (CHSH) non-local game [102]. If Alice and Bob can statistically violate the CHSH inequality, then Alice and Bob must share an entangled state. By monogamy of correlations [82, 103], Eve's system must then be uncorrelated, i.e. $\rho_{ABE} = \rho_{AB} \otimes \rho_E$, she thus cannot gain information from Alice and Bob's systems.

Clauser-Horne-Shimony-Holt inequality

A convenient way to present Bell's theorem is by playing non-local games [104]. More specifically, let us consider the CHSH game in which we have two participants, which we shall again refer to as Alice and Bob. Alice and Bob receive input bits, s and t and must produce output bits a and b. Alice and Bob win the game if $a + b \mod 2 = s \cdot t$. In other words, if Alice and Bob are asked questions s and t, their goal is to provide answers a and b such that $a + b \mod 2 = s \cdot t$. Evidently, this game has some rules. First, the questions sent to Alice and Bob are chosen with uniform probability, i.e. $p(s = 0) = p(s = 1) = 1/2$ similarly $p(t = 0) = p(t = 1) = 1/2$. Furthermore, while players can agree on a strategy beforehand, once the game starts, players are no longer allowed to communicate. In a classical setting, the optimal strategy consists of Alice and Bob answering $a = b = 0$ each round, in which case they win with probability 3/4. This bound can be expressed as a property of the output bits a_0, a_1, b_0, b_1, where $a_i = i$ corresponds to Alice's answer and similarly for Bob. The CHSH inequality then states that for any $A_0, A_1, B_0, B_1 \in \{-1, 1\}$, where $A_i = (-1)^{a_i}, B_i = (-1)^{b_i}$, it holds that [102, 105]:

$$S = A_0B_0 + A_0B_1 + A_1B_0 - A_1B_1 \leq 2. \tag{1.1}$$

Returning to the non-local game, it turns out that if Alice and Bob share some entangled state, they can do much better. The idea is quite simple, Alice and Bob each apply some rotation to their qubit depending on the question they are asked. They then measure the qubit and answer the question based off the measurement outcome. Suppose, for instance, the entangled state shared between Alice and Bob is the $|\Phi^-\rangle = \frac{1}{\sqrt{2}}(|00\rangle - |11\rangle)$ state. After the rotations, the resulting state will be

$$R(\theta_s) \otimes R(\theta_t) |\Phi^-\rangle = \cos(\theta_s + \theta_t) |\Phi^-\rangle + \sin(\theta_s + \theta_t) |\Phi^+\rangle ,$$

where $|\Phi^+\rangle = \frac{1}{\sqrt{2}}(|00\rangle + |11\rangle)$. The probability then that $a + b \mod 2 = 0$ is $\cos^2(\theta_s + \theta_t)$. Similarly, $p(a + b \mod 2 = 1) = \sin^2(\theta_s + \theta_t)$. Consider now the following strategy: for s (t) equal to 0 Alice (Bob) applies a $R(-\frac{\pi}{16})$ rotation, whereas for s (t) equal to 1, Alice (Bob) applies a $R(\frac{3\pi}{16})$ rotation. The success probability is then given by $\cos^2(\frac{\pi}{8}) \approx 0.85$, beating the classical bound. This strategy results in a violation of the inequality in Eq. 1.1 and has profound implications for nonlocality and quantum communication that will be revisited in chapter 5.

1.4 Outline

Over the past four years since I joined the Quantum Photonics Laboratory (QPL) led by Professor Thomas Jennewein, I had the opportunity to contribute to research projects focused on enabling technologies towards a Quantum Internet.

In September 2021, I joined the QPL and supported the demonstration of a fully passive, reference frame independent (RFI) time-bin QKD protocol over a moving free-space channel led by Dr. Ramy Tannous [106]. In January 2022, I started working on the *High-Rate and Networkable Quantum entanglement Source* (HiRaNQS) project in collaboration with Dr. Duncan England, from the National Research Council, and Professor Chang-qing Xu, from McMaster University. The goal of the project at the onset was to develop a compact, chip-based entangled photon source with multichannel capability to overcome current satellite-based quantum communication limitations by enabling high signal throughput and simultaneous connectivity. My first task on the project was to develop a numerical simulation framework to benchmark the performance of different source designs for various link scenarios. Once the source design was finalized in January 2023 [1], I began working on its experimental demonstration [2]. I was fortunate to have the opportunity to visit Professor Chang-qing Xu group at McMaster University, where I familiarized myself with their waveguide coupling techniques and gained hands-on experience with their alignment procedures. During this process, I also worked closely with and supervised undergraduate researcher Garen Simpson, who contributed to the assembly and testing of the experimental setup. From January 2022 to June 2025, I led the experimental demonstration of a reconfigurable quantum network architecture, designed to integrate satellite links into metropolitan quantum networks.

In June 2023, I joined the *HyperSpace* project, a joint Canada-EU collaboration, aiming to distribute entangled photons between Canada and Europe. My role was to investigate the feasibility and potential of frequency-bin quantum communication over free-space channels. Together with Wilson Wu and Yujie Zhang, I demonstrate a proof-of-concept implementation of frequency-bin quantum communication over free-space leveraging a field-widened interferometers (FWI) to decode the frequency-bins without any spatial filtering thereby enabling high-throughput quantum communication over turbulent, multi-spatial mode channels [107]. From September 2024 to March 2025, visiting student Massimo Giacomin and I built two FWIs for a frequency-bin entanglement distribution experiment. Kaylee Sherk and Luke Neal also contributed to the design of the interferometers. After characterizing the interferometers in Waterloo, we shipped them to the Università di Pavia, where Marcello Bacchi, Dr. Marco Clementi and Professors Matteo Galli and Daniele Bajoni developed an integrated frequency-bin entangled photon source based on micro-ring

resonators in silicon nitride (SiN). Massimo Giacomin and I traveled to Pavia in February 2025. Together with Massimo Giacomin, Marcello Bacchi, and Dr. Marco Clementi, I demonstrated frequency-bin entanglement distribution over multi-mode channels exploiting a novel time-resolved detection scheme paired with passive linear interferometry. Our approach also enabled, to the best of my knowledge, the first measurement of the joint temporal intensity (JTI) of frequency-bin entangled photons revealing rich temporal correlations. Since March 2025, I have also supported the work of Dr. Ramy Tannous on a Herriott cell interferometer which enables long time delays in a compact form factor while remaining compatible with multi-spatial-mode input light—making it well suited for free-space quantum communication channels. My experimental activities for this thesis ended in April 2025.

A subset of these activities is presented in this thesis, and an outline of each chapter is given below. Note that, in the remaining chapters, I will use "we" rather than "I" in accordance with scientific writing conventions. The reader is kindly referred to the Statement of Contributions for details regarding my contributions to each project.

Chapter 2 introduces a reconfigurable quantum network architecture to efficiently integrate satellite links into metropolitan quantum networks. In chapter 3, we experimentally demonstrate this adaptive quantum network using a correlated photon pair source specifically designed for the QEYSSat mission. Exploiting both frequency and time multiplexing, we obtain a significant performance increase without additional resource overhead, thereby showcasing the scalability potential of our approach.

In chapters 4-5 we then focus on frequency-bin quantum communication, a promising encoding scheme that offers unique advantages for quantum networking. Thus far, frequency-bin demonstrations have been limited to single-spatial-mode operation. In chapter 4 we propose and demonstrate a multi-mode compatible detection scheme leveraging time-resolved detectors and field-widened interferometers. Our analyzer is purely passive and does not require spatial filtering or adaptive optics, making it well suited for quantum communication over fluctuating channels. Chapter 5 continues our exploration of frequency-bin quantum communication, this time in the context of entanglement distribution. Compact, adaptable, and cost-effective technologies will be essential to scale quantum networks toward global deployment. Using a simple time-resolved detection scheme, we distribute entangled frequency-bins generated from a photonic integrated circuit over multi-spatial mode channels and achieve high fidelity quantum state tomography and entanglement certification.

We conclude with a summary in chapter 6, highlighting the main findings and suggesting directions for future research. Please note that chapters 2-5 of this thesis correspond to

work published in [1, 2, 3, 4].

Chapter 2

A reconfigurable entanglement distribution network suitable for connecting multiple ground nodes with a satellite

This chapter is based on reference [1] and overlaps with its text.

2.1 Introduction

As discussed in chapter 1, a primary objective of quantum communication is the distribution of entanglement between distant parties [10]. In recent years, significant research efforts have focused on expanding the scalability of quantum networks beyond two communicating parties. To this extent, multiple network architectures have been proposed, notably trusted-node networks consisting of a mesh of point-to-point links, where each node acts as a trusted relay to establish a complete two-party communication set-up [30, 34, 49, 50, 108]. While such a scheme is compatible with heterogeneous quantum links and can be used to increase the communication distance arbitrarily, it comes with a significant security cost as one must ensure the privacy of every relay site. Alternatively, active switch quantum networks [31, 109, 110, 111, 112] allow for dynamically reconfigurable networks, yet are vulnerable to device failure. Furthermore, the distribution rate is limited by the switch's operating speed. Hence, an all-passive solution is preferred where all users can be connected simultaneously.

Two main approaches have previously been considered to create fully connected quantum networks relying either on high-dimensional entanglement or bi-partite entanglement and multiplexing [49, 67, 113, 114, 115, 116, 117]. In the multipartite method, each user pair shares a different subspace of the overall network's Hilbert space, which is used to generate their keys. However, adding or subtracting users from the network requires changing the dimensionality of the state produced by the source, making this approach impractical. The multiplexing approach is described in the following section.

2.1.1 Multiplexing and hyper-entanglement

Multiplexing is a standard approach in classical communications to increase the communication rate and share resources,such as bandwidth, time, or physical paths (e.g. optical fibres), between channels [118]. There are two main approaches to multiplexing exploiting time division multiplexing (TDM) or wavelength division multiplexing (WDM). In the former, different channels are encoded in different time slots, whereas in the latter, different channels correspond to different wavelengths. In the quantum picture, multiplexing exploits the inherent hyper-correlations produced by an entangled photon source and can be used to increase the communication channel capacity or deterministically separate correlated photon pairs to different users. Consider, for instance, a spontaneous spontaneous parametric down-conversion (SPDC) entangled photon source (EPS) producing polarization entangled photons in the $|\Psi^-\rangle$ state [116]. Due to energy conservation of the nonlinear process, the frequency domain is also entangled. Consequently, the output state is hyper-entangled:

$$|\Psi^-\rangle \approx \int \alpha(\omega_s, \omega_i)\, |\omega_s, \omega_i\rangle \otimes \frac{1}{\sqrt{2}}\Big(|HV\rangle - |VH\rangle \Big) d\omega_s d\omega_i, \tag{2.1}$$

where $\omega_s + \omega_i = \omega_p$ and $\alpha(\omega_s, \omega_i)$ is a continuous function characterizing the spectrum of the SPDC source. As the spontaneous parametric down-conversion produces well-defined correlations in discrete spectral regions, with proper filtering we can express the resulting state as:

$$|\Psi^-\rangle_{MUX} \approx \Pi_{k=1}^{N} \otimes \frac{1}{\sqrt{2}}\Big(|H_{\omega_k^s} V_{\omega_k^i}\rangle - |V_{\omega_k^s} H_{\omega_k^i}\rangle \Big), \tag{2.2}$$

where N is the total number of frequency pairs contributing independently to the overall output. We can thus interpret the multiplexed source as effectively comprising N independent entangled photon sources, as depicted in Fig. 2.1 each operating at a distinct demultiplexed frequency pair (ω_k^s, ω_k^i). This architecture eliminates the need to trust the

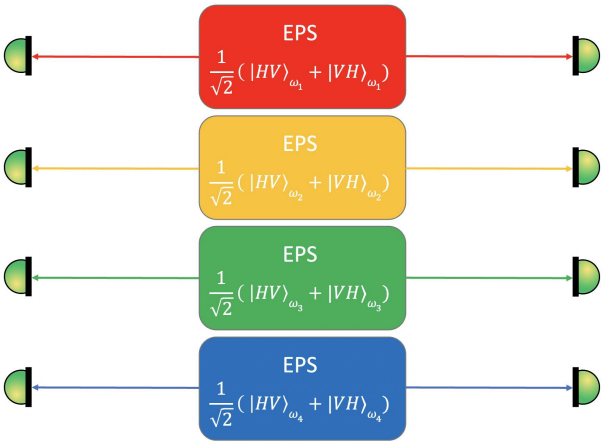


Figure 2.1: Conceptual sketch for wavelength division multiplexing as described in Eq. 2.2. Each color-coded EPS corresponds to a single correlated frequency channel.

service provider and is easily scalable as the number of users in the network can be modified without any change to the photon source. Nevertheless for an n-node network to be fully connected, $\mathcal{O}(n^2)$ multiplexed channels are required. Consequently, there remains an important hardware requirement as each channel requires a decoder and detector module to be fully distinguishable. Otherwise an increase in accidental counts will deteriorate the performance of the network as was shown in [49, 116]. Recently, [48, 119, 120, 121] utilized beamsplitters in addition to multiplexing to increase the scalability of their network, but at the expense of the key generation rate. An interesting solution proposed by [49], uses a pulsed source to recover the channel distinguishability despite limited detector resources. This implementation requires an additional gating signal to be sent to each user, and results in noise reduction by a factor equal to the gating duty cycle. However, this scheme is unsuitable for mobile nodes as the delays to every other node would need to be continuously compensated by each user thus restricting the reach of these quantum networks to metropolitan areas.

In this chapter we present a scalable quantum network architecture that includes a mobile satellite node with minimal hardware requirements. To interface the fibre-optical network with the satellite link, we consider a pulsed non-degenerate entangled photon source in conjunction with a frequency-to-time mapping (FTM) [122, 123]. Using a medium with a high group delay dispersion (GDD), one can carefully map the frequency distribution of pulsed light onto temporal modes such that each frequency channel obtains a distinct time delay within the resolution of the detector. The satellite node is then able to unambigu-

ously separate the channels while using a single detector module. The rest of the chapter is organized as follows. In Section 2.2, we introduce the reconfigurable quantum network architecture. In Section 2.3 we analyze the performance of the proposed network configuration and benchmark its potential by studying its use case for the Canadian QEYSSat quantum satellite mission [71]. A summary of our results and various extensions are given in Section 2.4.

2.2 Network architecture

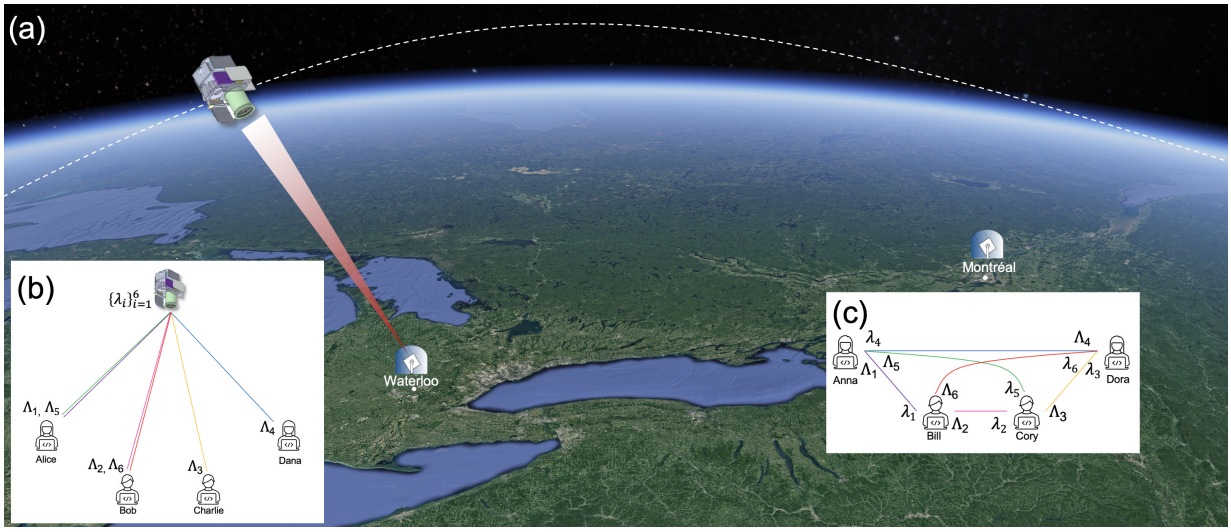


Figure 2.2: (a) Communication layer and wavelength allocation for a satellite pass over two ground stations e.g. over Waterloo and Montreal. (b) Waterloo is in view of the satellite and takes the multipoint-to-point satellite pass configuration whereas Montreal is in a fully connected ground topology (c). At a later time, with the satellite now in view of Montreal, the two cities will adopt the opposite topology by redistributing the frequency-time correlated pairs $\{\lambda_i, \Lambda_i\}$ between the nodes. During the satellite pass Alice and Bob are connected by two frequency-time channels and thus enjoy a higher key rate.

The proposed network architecture is depicted in Fig. 2.2. It allows two reconfigurable quantum metropolitan-area networks (QMAN), for example in Waterloo and Montreal, Canada, to be connected by ground-to-satellite quantum links. As the satellite passes over Waterloo in Fig. 2.2b, the network adopts a multipoint-to-point topology from the N ground nodes to the satellite. Consequently, allowing for a substantive increase of the key

generation during the satellite pass via multiplexing. Meanwhile, the Montreal network in Fig. 2.2c is arranged into a pairwise configuration where every user is connected to each other. As the satellite travels out of reach of Waterloo and within reach of Montreal, each network reconfigures itself into the opposite topology to optimize its functionality throughout the day. This rearrangement is enabled by the hybrid quantum network design in Fig 2.3. For a satellite uplink, the idler is kept on the ground and distributed to the network users. During the satellite pass, the signal is sent through a frequency-to-time encoder $\tau(\lambda)$ to assign a time delay to each wavelength channel. This mapping can be accomplished by wavelength-dependent group delay dispersion e.g. in a chirped fibre Bragg grating (CFBG) [122, 124, 125], where different wavelengths are reflected at different positions along the grating resulting in a wavelength-dependent time delay, or by using a fibre Bragg grating (FBG) array with suitable spacing between each FBG to obtain the desired time delay [123]. Outside of the satellite pass, the active switch, here implemented using a flip mirror, redirects the signal to the ground nodes.

The minimal time separation between each channel for the frequency-to-time mapping is determined by the timing jitter of the satellite single-photon detector and readout electronics which is typically on the order of $\sim$ 130 ps full-width at half-maximum for Silicon Avalanche Photodetectors (Si-APD) [126, 127, 128, 129]. Thus, for a 80 MHz pump repetition rate, the satellite network configuration is limited to a maximum of ~ 95 frequency-time channels within the 12.5 ns pulse train. To ensure the channel distinguishability, the GDD must then be greater than $\sim$ 325 ps/nm. Additionally, guard bands can be utilized to minimize cross-talk between the channels but at the expense of the achievable channel density [130]. For a given device length, the GDD and the CFBG's reflection bandwidth are inversely proportional: a larger dispersion requires higher reflectivities, resulting in a narrower resonance and bandwidth [131, 132]. However, this limitation can be circumvented by using longer CFBGs or by using a CFBG array, i.e. inscribing or splicing multiple CFBGs with adjacent reflection windows in succession [122].

While the number of channels depends on the entangled photon source's brightness and bandwidth, for simplicity we assume four nodes in each QMAN in Fig. 2.2. To create a fully connected N-user communication network, $\binom{N}{2}$ links are needed. Consequently, in the satellite configuration shown in Fig. 2.2b the six channels are distributed to the users such that Alice and Bob each receive two frequency-time channels and therefore attain an increased secure key rate. For the pairwise fully connected topology in Fig. 2.2c, each node receives 3 wavelength channels to allow communication with every other node. The network connectivity and the wavelength allocation for the two different configurations: satellite (flip mirror up) and ground (flip-mirror down) are summarized in Table 2.1.

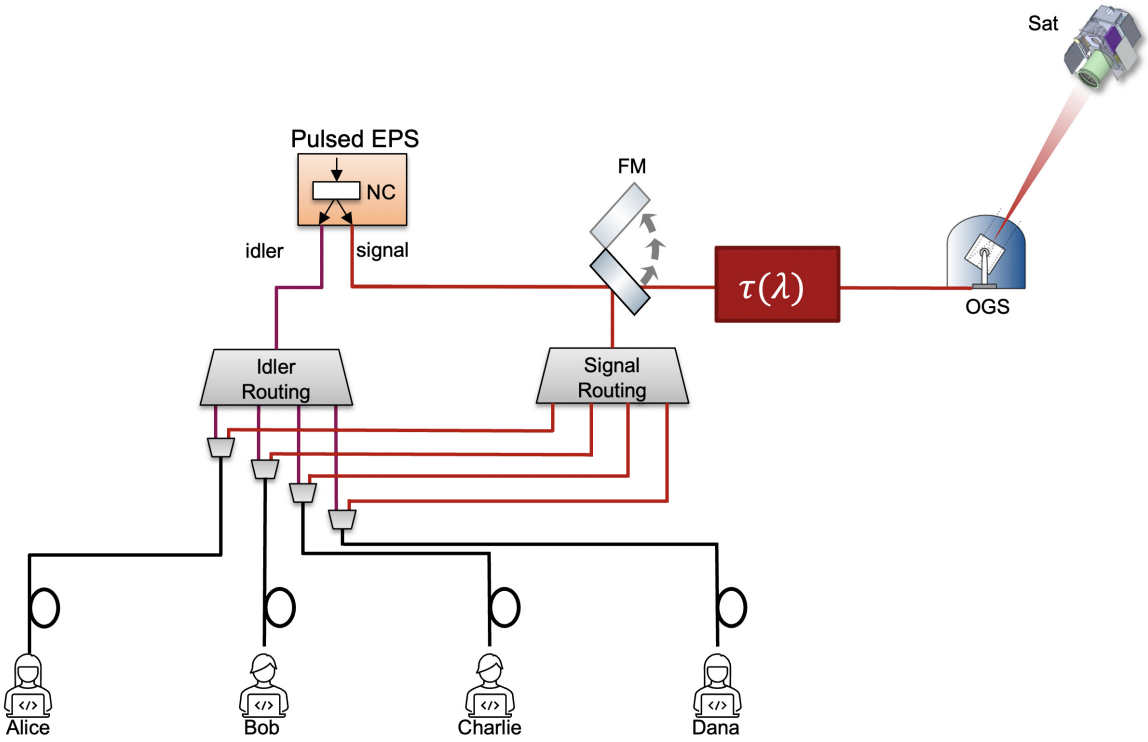


Figure 2.3: Conceptual physical layout of the hybrid quantum network. The EPS consists of a nonlinear crystal (NC) pumped by a pulsed laser to create entangled photon pairs via spontaneous parametric down-conversion. During the satellite pass (flip mirror (FM) up) the signal is sent through a frequency-to-time encoder $\tau(\lambda)$ in an uplink to the satellite (Sat) via the OGS. Outside of the satellite pass (flip mirror down) the signal is rerouted with the idler through telecom fibre to the various ground nodes thus enabling a fully connected topology.

2.3 Performance estimation

We simulated the key rate for various quantum key distribution scenarios using the approaches introduced by Ma *et al.* [133] and Holloway *et al.* [134]. The simulation code and a more detailed description are provided in the Appendix A. Our entangled state is constructed from the following SPDC Hamiltonian:

$$H = i\chi(a_H^\dagger b_V^\dagger - a_V^\dagger b_H^\dagger) + \text{H.c.}, \tag{2.3}$$

where the subscripts H and V denote the horizontal and vertical polarizations, H.c. the Hermitian conjugate and χ is the squeezing parameter, a coupling constant proportional to the crystal nonlinearity and the amplitude of the pump beam [135]. We assume the protocol is symmetric with respect to the σ_X and σ_Z bases, thus all calculations for the rectilinear (σ_Z) basis can be applied to the superposition (σ_X) basis. Expectation values for the detector operators applied to the SPDC state are used in a squashing model to determine the two-fold coincidence rates and QBER [136, 137]. For practical computation, we restrict the receiver's (Bob) measurements to a finite Hilbert space. More specifically, the quantum key distribution protocol we consider is designed for qubit systems, whereas its implementation is carried out using optical modes described by infinite-dimensional Hilbert spaces [138]. A squashing model addresses this discrepancy by inserting an additional physical channel Λ between the quantum channel Φ and the receiver such that the infinite-dimensional states are reduced to finite-dimensional *squashed* states. The receiver then measures these states with a new set of measurements that reproduce the original statistics. Note that, the adversary is assumed to have full control of this squashing map. For a more detailed discussion of squashing maps, the reader is referred to Refs. [139, 140, 141]. We analyze the performance of both bucket detectors (Eq. 2.4) and photon-number resolving (PNR) detectors (Eq. 2.5) whose positive operator-valued measure (POVM) are, respectively, given by [142]:

$$\hat{E}^{(\text{click})} = \sum_{m=0}^{\infty} [1 - D(0)(1-\eta)^m] \left|m\right\rangle \left\langle m\right|, \tag{2.4}$$

and

$$\hat{E}^{(n)} = \sum_{m=0}^{\infty} \sum_{k=0}^{n} D(k) \binom{n-k+m}{m} \eta^{n-k} (1-\eta)^m \left|n+m-k\right\rangle \left\langle n+m-k\right|, \tag{2.5}$$

where η is the detector efficiency and $D(k)$ the dark count distribution. We model the detection probabilities of the signal and idler photons as independent such that the overall

transmittance for an n photon pair is $\eta_n = [1-(1-\eta_A)^n][1-(1-\eta_B)^n]$, where η_A and η_B represent the channel transmittance for Alice and Bob (including both channel losses and detection efficiency) [133]. For the satellite pass configuration, we assume the satellite detector to be a Si-APD [143] with a detector dead time of 1 μs whereas we assume the ground detector to be an superconducting nanowire single-photon detector (SNSPD) with a dead time of 10 ns [144, 145].

Table 2.1: Proposed network connectivity and wavelength allocation. Wavelength correlated pairs are denoted as $\{\lambda_i, \Lambda_i\}$ for signal and idler respectively. The specific wavelengths considered in Figs. 2.8-2.9 are provided in parentheses with their associated ITU channel number.

Network Connection	Satellite configuration		Ground configuration	
	signal	idler	signal	idler
Alice-Satellite	λ_1, λ_5	Λ_1, Λ_5	-	-
Bob-Satellite	λ_2, λ_6	Λ_2, Λ_6	-	-
Charlie-Satellite	λ_3	Λ_3	-	-
Dana-Satellite	λ_4	Λ_4	-	-
Alice-Bob	-	-	λ_1 (786.75 nm)	Λ_1 (Ch40 = 1545.32 nm)
Bob-Charlie	-	-	λ_2 (787.03 nm)	Λ_2 (Ch41 = 1544.53 nm)
Charlie-Dana	-	-	λ_3 (787.32 nm)	Λ_3 (Ch42 = 1543.73 nm)
Alice-Dana	-	-	λ_4 (787.63 nm)	Λ_4 (Ch43 = 1542.14 nm)
Alice-Charlie	-	-	λ_5 (787.93 nm)	Λ_5 (Ch44 = 1542.14 nm)
Bob-Dana	-	-	λ_6 (788.24 nm)	Λ_6 (Ch45 = 1541.35 nm)

Due to the dead time, the photon count rate is no longer linearly proportional to the impinging photon flux but is given by:

$$N_{count} = \frac{N_{ideal}}{1 + N_{ideal} T_D / T_{INT}}, \tag{2.6}$$

where T_D corresponds to the dead time, T_{INT} to the integration time, N_{ideal} to the number of photons impinging on the detector and N_{count} the number of resolved photons [146]. The secure key-rate (SKR) for the entangled parametric down-conversion (PDC) protocol [133] is then obtained via

$$SKR = q\{Q_\lambda[1 - f(\delta_b)H_2(\delta_b) - H_2(\delta_p)]\} \tag{2.7}$$

where q is the basis reconciliation factor, the subscript λ denotes the expected photon number per mode, Q_λ is the overall gain, δ_b (δ_p) is the bit (phase) error rate, $f(x)$ is the

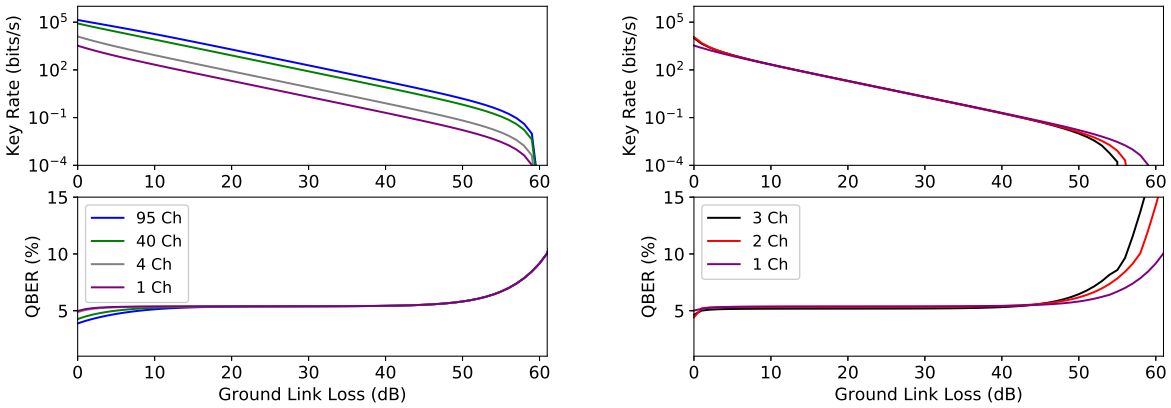
Table 2.2: Experimental assumptions for QKD modeling

Sat-APD dark count rate	1000 cps
Ground detector dark count rate	100 cps
Sat-APD timing jitter	130 ps
Sat-APD dead time	1 μs
Ground detector dead time	10 ns
coincidence time window	1 ns
Error correction factor	1.17
Satellite link loss	40 dB
Basis reconciliation factor (q)	1/2

bidirection error correction efficiency and $H_2(x)$ is the binary entropy function,

$$H_2(x) = -x \log_2(x) - (1-x) \log_2(1-x). \tag{2.8}$$

A summary of the experimental parameters assumed throughout the simulation can be found in Table 2.2. At low ground link loss (< 10 dB) in Fig. 2.4a, detector saturation at the satellite node partially limits the scaling performance. However, in the higher loss regime one obtains a linear key rate increase whilst maintaining the same QBER. This scaling stems from the deterministic separation of the multiplexed channels resulting in independent communication channels with the same signal-to-noise ratio [49]. To achieve this deterministic scenario, the frequency-to-time mapping $\tau(\lambda)$ plays a crucial role. This is particularly apparent, in Fig. 2.4b where we only consider wavelength multiplexing. In fact, in our initial network design shown in Fig. 2.5, the idler photons were demultiplexed on the ground but the signal photons were recorded at the satellite detector without any channel discrimination. Surprisingly, demultiplexing solely the idler at the ground stations provides little advantage and, in fact, results in a maximal tolerable loss decrease compared to the single channel scenario. This is due to an increase in accidental coincidences that results in a loss of fidelity caused by the detection of several channels on the single satellite detector [116]. Therefore, the signal-to-noise ratio decreases proportionally to the number of users added. The squeezing parameter χ in Eq. 2.3 was optimized for every channel setting to maximize the SKR using a sequential least squares programming (SLSQP) algorithm, as shown in Fig. 2.6. At high losses, the dark count rate contribution to the QBER becomes significant, ultimately leading to a sharp drop in the secure key rate. This behaviour is visible in typical QKD key rate curves (see Fig. 2.7). For fixed squeezing, the error ratio associated with multi-pair emissions remains constant. Consequently, the effective maximum loss budget of the system is determined by the dark count rate. In our



(a) With time-frequency mapping

(b) Without time-frequency mapping

Figure 2.4: Scaling behaviour of the ground-to-satellite QKD scenarios for (a) with the time-frequency mapping. The time and frequency multiplexing leads to a linear key rate improvement. (b) Without the $\tau(\lambda)$ frequency-to-time encoder, there is no discrimination made between the wavelength channels jointly recorded at the satellite resulting in an increase in accidental counts and reduction in key rate. The squeezing parameter χ in Eq. 2.3 was optimized for every channel setting to maximize the SKR as shown in Fig. 2.6b. Realistic detector parameters were considered and can be found in Table 2.2.

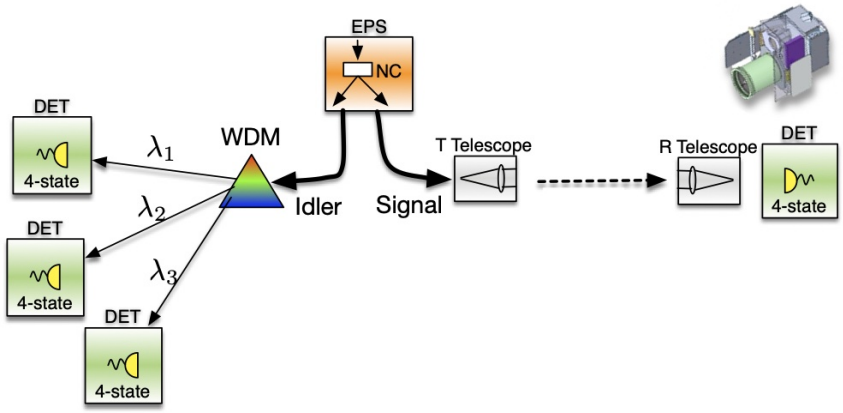
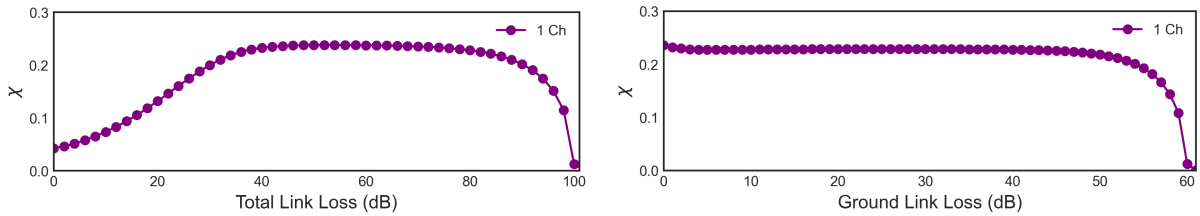


Figure 2.5: Initial proposal for the physical layout of the hybrid quantum network. The EPS is pumped by a continuous-wave laser and the idler photons are frequency demultiplexed to the ground nodes. Without the FTM no temporal discrimination is possible at the satellite node.



(a) **(b)**

Figure 2.6: Optimized squeezing parameter for (a) a symmetric link where $\eta_s = \eta_i$ and (b) an antisymmetric link where the satellite link loss is fixed $\eta_s = 40$. The remaining simulation parameters were chosen in accordance with Table 2.2.

simulation, the squeezing parameter is reduced at high losses, to suppress errors due to multi-photon emissions and remain below the QBER threshold for positive key rate. In the numerical simulation, the squashing map probabilistically assigns multi-photon events to qubit outcomes. This probabilistic assignment leads to errors due to the detection of uncorrelated channels and constitutes the dominant error mechanism in the low-loss regime. Consequently, at low loss (see Fig. 2.6b), the squeezing is also kept low to avoid detector saturation and minimize the multi-photon contribution. Between these extremes, the optimal squeezing increases with channel loss to compensate for reduced transmission, until it reaches a plateau. This plateau represents a trade-off between the multi-pair emissions and the pair-production rate.

At low loss, the one-sided multiplexing approach yields a slight key rate increase due to detector load management bypassing the dead time of the detector. Nonetheless, for realistic loss scenarios detector saturation has negligible significance. We investigate in Fig. 2.7 the use of PNR detectors at the ground user nodes. Interestingly, we find that PNR detectors offer no significant key rate advantage compared to bucket detectors. This can be readily seen in the high loss regime from considering the series expansion of $\hat{E}^{(1)}$ for $D(1) \ll 1, \eta \to 0$ at which point one finds that $\hat{E}^{(1)} \to \hat{E}^{(\text{click})}$.

2.3.1 Quantum Encryption and Science Satellite mission

To further benchmark the potential of our network proposal, we analyze its performance for the QEYSSat mission use case. For this purpose, we assume the entangled photon source consists of a 15 mm long periodically poled magnesium-oxide doped lithium niobate (PPLN) waveguide pumped by a mode-locked pulsed laser centered at 521.4 nm with a

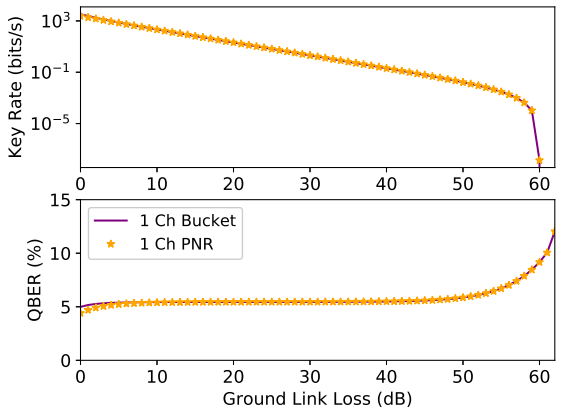


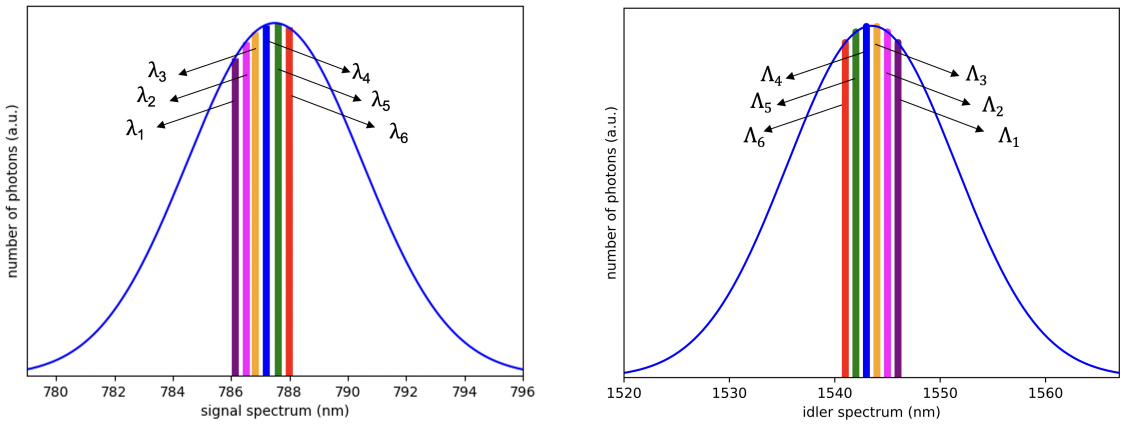
Figure 2.7: Secure key rate performance comparison between PNR and Bucket detectors for the ground user nodes. The simulation parameters considered can be found in Table 2.2.

bandwidth of 2 nm and a repetition rate of 80 MHz which produces polarization entangled photon pairs at 787.5 nm (signal) and 1543.2 nm (idler) via spontaneous parametric down-conversion with respectively 15 nm and 39 nm of bandwidth. These assumptions on the entangled photon source are summarized in Table 2.3. The required wavelength channels

Table 2.3: Entangled photon source assumptions

Repetition rate	80 MHz
Pump central wavelength	521.4 nm
Pump bandwidth	2 nm
Signal central wavelength	787.5 nm
Signal bandwidth	15 nm
Idler central wavelength	1543.2 nm
Idler bandwidth	39 nm

for a hypothetical 4-node ground network and QEYSSat are illustrated in Fig. 2.8. The color coding is done in accordance with the channel allocation depicted in Fig. 2.2. The idler wavelength channels were chosen for compatibility with the standard International Telecommunication Union (ITU) 100 GHz grid. The corresponding correlated signal channel around 787.5 nm was selected for low-loss transmission through the atmosphere and compability with mature high-efficiency Si-APDs [51, 147]. Outside of the satellite pass,



(a) (b)

Figure 2.8: The spectrum of the signal (a) and the idler (b) were calculated from the Sellmeier equations for PPLN assuming a 2 nm pump bandwidth centered at 521.4 nm and a 15 mm crystal [5]. Wavelength correlated pairs $\{\lambda_i, \Lambda_i\}$ are denoted by the same color in both spectrums and were chosen in accordance with Fig. 2.2. The idler channels match the ITU DWDM 100 GHz grid.

the 787.5 nm signal is rerouted to the ground users through standard telecom infrastructure. Whilst the telecom fibre is slightly multimode for the 787.5 nm light, Meyers-Scott *et al.* have shown that there is minimal crosstalk between the spatial modes over several kilometers resulting in a well-preserved polarization state and timing signature [148]. In spite of the greater fibre losses for the 787.5 nm light ($\sim$ 3 dB/km), the 32 km range shown in Fig. 2.9 is large enough to span a metropolitan area network. Furthermore, the range for the ground configuration could be expanded with a telecom-band degenerate entangled photon source [48] or via quantum frequency conversion of the signal to telecom [149]. As the ground user nodes are not resource-limited, we can circumvent the detector timing limitation via frequency demultiplexing to extend the linear performance increase to the low-loss regime. Table 2.4 shows the estimated key produced per month between ground users (ground configuration), and between a satellite and ground users (satellite configuration). Assuming that over a one-month period, one would typically have around 10 satellite passes with a typical 100 seconds quantum link duration, we estimate the total key generated monthly in both configurations by a user located 16 kilometres equidistant from all other users in the network and the optical ground station (OGS). In the ground configuration, the 95 channels can connect up to 14 users with two preferred connections.

The average key generated by a given user pair is then $\sim 1.9 \times 10^{11}$ bits. For the satellite configuration, the link loss will vary throughout the pass. Based off of the link loss data from [51], we compute a conservative estimate by assuming an upper quartile pass with 45 dB average link loss, which corresponds to a generated key of $\sim 4.1 \times 10^{7}$ bits. The proposed design presents a considerable scaling potential as the entire SPDC spectrum can be utilized. Assuming detector time resolutions as low as 35 ps [150], a 80 MHz repetition rate and an ultra-dense WDM (UDWDM) with 12.5 GHz spacing, one could employ up to ~ 350 channels. The number of available frequency-time channels could be further increased by reducing the pulse repetition rate but at the expense of the single channel key rate.

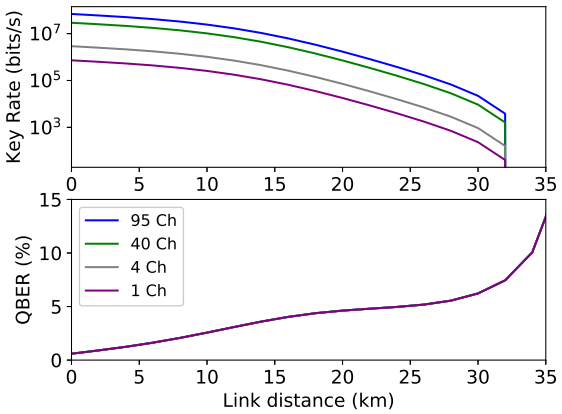


Figure 2.9: Scaling behaviour of the ground configuration (Fig. 2.2c) for the QEYSSat compatible scenario considered in Table 2.3 with the detector parameters given in Table 2.2.

2.4 Summary

In this chapter, we proposed and analyzed a reconfigurable architecture suitable for serving both metropolitan networks and ground-satellite links. Our approach is uniquely designed to optimize the efficiency of satellite uplink scenarios such as QEYSSat, where the satellite receiver is only available for a few minutes every 24 hours. During the satellite pass, the secure key rate is improved through time and frequency multiplexing with no additional hardware requirements on the satellite. Additionally, the network's utility outside of the

Table 2.4: Generated key rate over a one-month period for both network configurations

User-to-user ground distance	16 km
Number of ground users in the network	14
User to OGS distance	16 km
Average number of passes	10
Average satellite pass duration	100 s
Average satellite link loss	40 dB
Total key generated per ground user pair	1.9×10^{11} bits
Total key generated between a ground node and satellite	4.1×10^{7} bits

satellite pass is optimized by rerouting the signal to form a ground-based metropolitan network. The satellite can be exploited as a trusted node station to interconnect two metropolitan areas and extend the reach of quantum networks to a global scale. Its scalability and simplicity make our network architecture a good candidate for commercial quantum communication networks.

Chapter 3

Demonstration of a reconfigurable ground to space quantum networking scheme

This chapter is based on reference [2] and overlaps with its text.

3.1 Introduction

In this chapter, we experimentally demonstrate the network reconfiguration, introduced in chapter 2, using correlated photon pairs generated from a PPLN waveguide specifically designed for the QEYSSat uplink scenario [56, 71]. In particular, non-degenerate broadband photon pairs at 1550 and 785 nm are produced from spontaneous parametric down-conversion to optimize both the ground-based optical fibre and the ground-to-space free-space link. Moreover, by leveraging time multiplexing, we demonstrate a linear performance increase for the up-link configuration with minimal satellite hardware requirements. In particular, a pulsed pump in conjunction with a frequency-to-time mapping assigns a distinct time delay to each spectral channel such that the signal can be demultiplexed from a single detector channel thus significantly reducing the satellite payload overhead [122, 151]. This resource alleviation extends to the ground configuration where only one detector per user is required. Indeed, the pulsed pump allows for channel discrimination by defining fixed time slots for the arrival of each channel at the detector thus reducing the number of accidental coincidences [49].

3.2 Experimental setup

The experimental setup is shown in Fig. 3.1. A mode-locked titanium-sapphire laser (*Tsunami Spectra-Physics*) with a repetition rate of 80 MHz produces 1042 nm light, which is upconverted in a BBO crystal (*Castech Inc.*) via second-harmonic generation and filtered down to a ~ 2 nm bandwidth centered around 521.4 nm. These upconverted photons then pump a 15 mm long PPLN waveguide (*HC Photonics Corp.*) such that broadband photon pairs at 787.5 nm (signal) and 1543.2 nm (idler) are produced via non-degenerate type-0 SPDC. PPLN waveguides offer high brightness, compactness, and compatibility with integrated devices [152]. After correction for losses, the brightness of the SPDC source was estimated to be $> 7.8 \times 10^7$ pairs/sec/mW. A temperature controller was used to maintain the PPLN's temperature at 30 °C so that the phase matching of the SPDC process is optimized to maximize photon generation within the QEYSSat passband chosen for high atmospheric transmission and compatibility with high efficiency space-ready detectors [69]. Signal and idler photons are separated at a dichroic mirror and coupled into polarization-maintaining (PM) fibres. The signal fibre output is connected to two different detection scenarios depending on the satellite's availability. For a satellite uplink, the idler photons remain on the ground and are routed to the various users. This is accomplished via WDM using concatenated telecom FBGs (*O/E Land Inc.*) and optical circulators (*OZ Optics*).

For the satellite configuration shown in Fig. 3.1a, a FTM unit enables a time-resolved detection of the distinct frequency channels on the same Si-APD detector. This FTM is implemented using a fibre Bragg grating array that inscribes a distinct time of arrival to each spectral channel, enabling multipoint-to-point communication with the satellite as depicted in Fig. 3.1c. For the ground network shown in Fig. 3.1b, a fully-connected topology between Alice, Bob and Charlie is established by WDM using individual FBGs, while Dana is excluded due to experimental resource constraints. Although the connections in Fig. 3.1b are established asynchronously using an active switch, they could be implemented simultaneously by adding an optical circulator to passively demultiplex all three signal wavelengths. To optimize detection efficiencies around both 780 and 1550 nm, Bob and Charlie were equipped with a Si-APD and SNSPD detector (*Quantum Opus*). This requirement could be overcome by using a broadband detector [153], thus eliminating the need for multiple detectors tailored to specific wavelengths, thereby reducing the system complexity. To demonstrate this scalable approach, the 1550 and 780 nm photons, corresponding respectively to channels 1 and 2 in Fig. 3.1d, are combined into the same single-mode fibre (*Thorlabs SMF-28*) using a 1550/780 nm wavelength division multiplexer (*Seagnol Photonics*) and jointly recorded on Alice's SNSPD detector. Although the 780 nm photons will be slightly multimode and suffer significant optical loss in the telecom

fibre, Meyers-Scott *et al.* [148] demonstrated the high-fidelity transmission is nonetheless possible and Vinet *et al.* [1] showed that positive nonzero key rates can be generated for up to 32 km, enough to span a metropolitan area network.

3.2.1 Materials and methods

The total optical loss in the experimental setup arises from several distinct stages. At the chip interface, light was coupled into and out of the waveguide with 532 nm and 1550 nm polarization-maintaining flat cleaved and lensed fibres (*OZ Optics*) respectively, incurring a coupling loss of approximately 4.5 dB. The waveguide coupling stage is shown in Fig. 3.3. The input and output fibres were mounted on three-axis translation stages (*MAX313D, Thorlabs*), each controlled by a piezo controller (*BPC203, Thorlabs*), to enable precise positional adjustment. The input fibre was flat cleaved using a fibre cleaver (*Vytran LDC-400*) and butt coupled to the waveguide. In other words, the fibre and waveguide facet were end-to-end aligned such that the fibre core and waveguide were in direct contact (or close proximity) as shown in Fig. 3.3c. To facilitate the alignment process, 1064 nm light was backpropagated and up-converted via second-harmonic generation to 532 nm through the waveguide. The upconversion was optimized by tuning the position of the output fiber and monitoring the 532 nm power at the waveguide input. Once the placement of the output fiber was optimal, the input cleaved fiber was introduced and carefully aligned to maximize the overall throughput. The waveguide was mounted in its oven (*HC Photonics*) and placed on a two-axis (vertical and horizontal) translation stage for precise positioning. The coupling process was monitored via an overhead stereo microscope (*Leica M125 C*) with a tunable magnification between 12.8 and 160X.

The waveguide used in the experiment was a PPLN ridge waveguide fabricated on a z-cut substrate. The chip dimensions were $15 \times 0.5 \times 1.5$ mm (length $\times$ width $\times$ thickness), with the waveguide defined on the z-facet at a depth of approximately 2.8μm. The width of the channel was 6μm and the mode field diameter were 4.83 and 4.16μm for the transverse y- and z-directions respectively. Following the down conversion, a free-space bridge separated the signal and idler photons, with measured coupling efficiencies of 44% (3.57 dB loss) for idler photons and 16% (7.96 dB loss) for signal photons. The reduced coupling efficiency for the latter was due to spatial mode filtering from the PM780 fibre (*Thorlabs*) as the $\sim$ 780 nm light is slightly multi-modal in the 1550 nm fibre at the output of the waveguide. The FTM unit introduced a significant insertion loss of 10 dB, due to the loss of 3 dB from the optical circulator and 7 dB attributed to the FBG array. On the idler path, demultiplexing was performed using a cascaded assembly of circulators and FBGs, as shown in Fig. 3.4, resulting in insertion losses of 4.86 dB, 7.73 dB, 10.48 dB, and 8.51

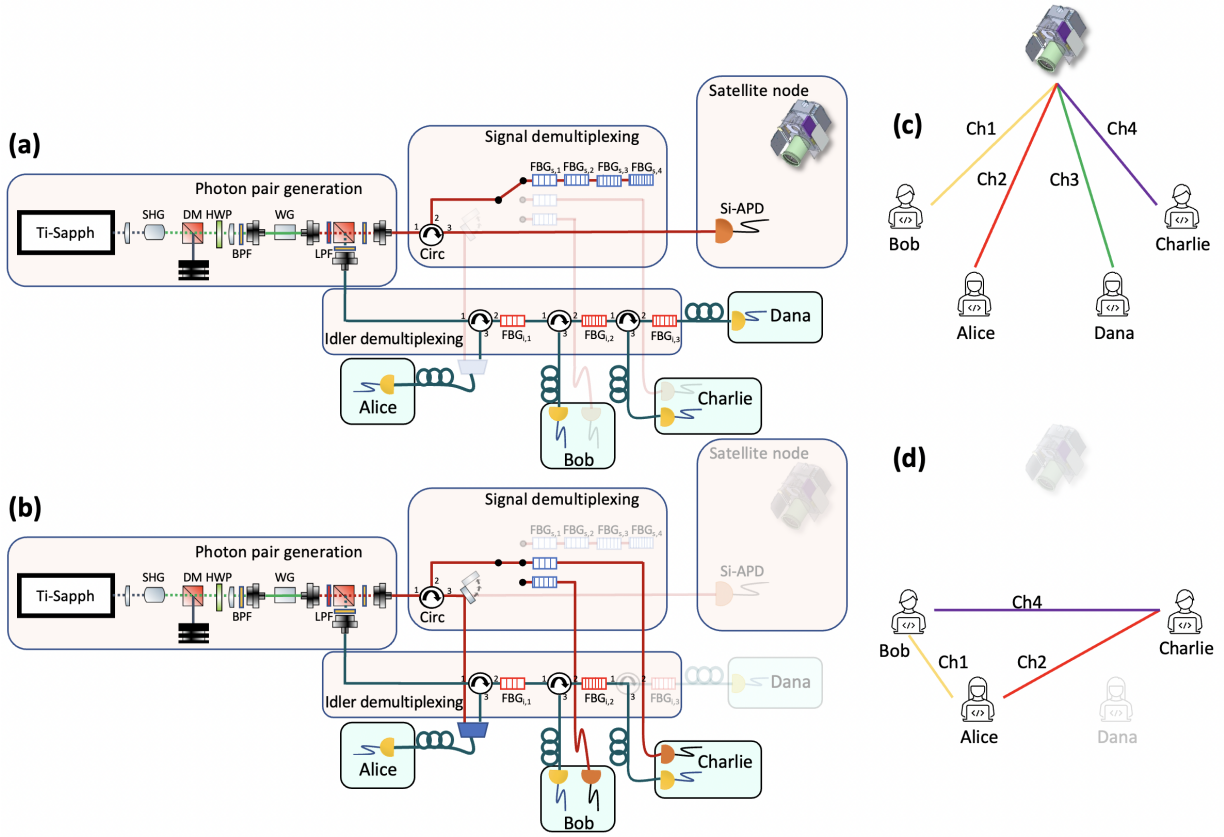
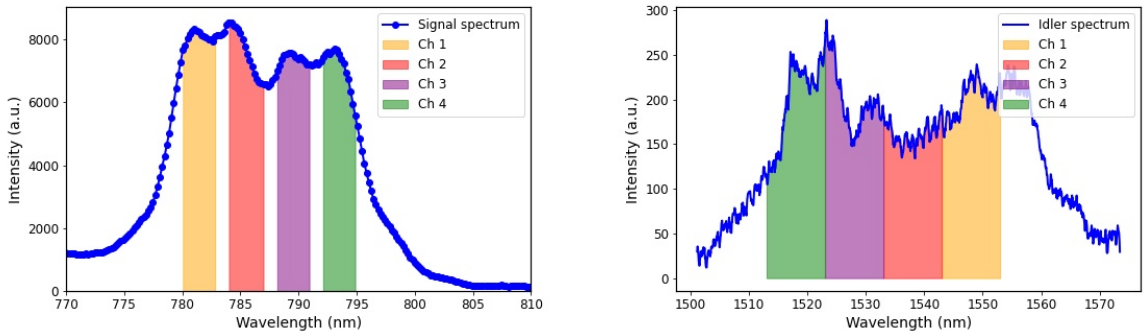


Figure 3.1: Experimental implementation of the reconfigurable quantum network for **(a)** the satellite configuration and **(b)** the ground configuration. A PPLN waveguide was pumped by a pulsed laser with a repetition rate of 80 MHz to create highly correlated photon pairs via type-0 spontaneous parametric down conversion. During a satellite pass, a frequency-to-time mapping is implemented using a fibre Bragg grating array as a dispersive component. Outside of the satellite pass, an active switch reconfigures the network into a three node ground network formed via wavelength division multiplexing. In both scenarios, the idler is frequency demultiplexed using off-the-shelf telecommunication components such as optical circulators and fibre Bragg gratings. To emphasize the differences between the two configurations, optical elements not used in each configuration are depicted in grey. The quantum correlation layer for each scenario is respectively shown in **(c)** and **(d)**. (SHG: second-harmonic generation, DM: dichroic mirror, HWP: Half-wave plate, BPF: band-pass filter, WG: waveguide, LPF: long-pass filter, Circ: circulator, FBG: fibre Bragg grating, SNSPD: superconducting nanowire single photon detector, Si-APD: silicon avalanche photodetector)



(a) **(b)**

Figure 3.2: The measured spectrum of the signal **(a)** and idler **(b)** photons. Wavelength correlated channels are denoted with the same color in both spectrums. 1 nm guard bands are used between the signal channels to minimize cross-talk between the channels.

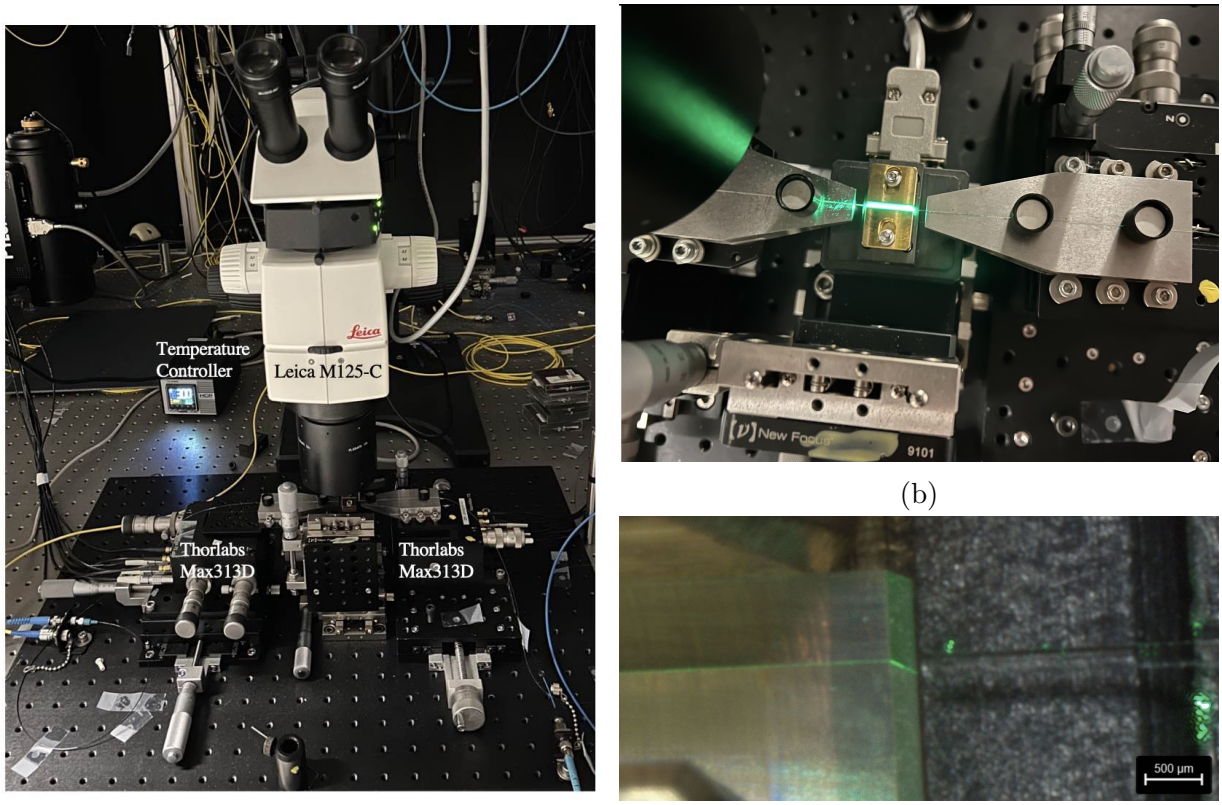
dB for the Alice, Bob, Charlie, and Dana channels, respectively. The 1550/780 WDM unit used for the ground configuration in Fig. 3.1b had an insertion loss of 0.97 and 3.02 dB at 1550 and 780 nm respectively.

3.2.2 An alternative frequency-to-time mapping

Although we opted for a fibre-based inline FTM using a series of FBGs to optimize compactness and ensure compatibility with standard telecom components, a free-space implementation could offer lower insertion loss, which may be advantageous in loss-sensitive applications. In Fig. 3.5a, we outline an alternative FTM approach in free-space. A pulsed laser diode produces an optical pulse which is sent through a grating. The grating spatially separates the input pulse into multiple diffraction orders, labeled 0 to 3. Each diffracted beam is directed toward a narrow bandpass filter (BPF) at a distinct angle of incidence (AOI), resulting in angle-dependent spectral filtering. Indeed, the central transmission wavelength (λ_θ) of the BPF exhibits a blue shift with increasing AOI, according to Eq. 3.1 [154], due to the change in effective optical path length (OPL) through the filter's interference layers

$$\lambda_\theta = \lambda_0 \sqrt{1 - (n_0 n_i^{-1} \sin\theta)^2}, \tag{3.1}$$

where λ_0 is the nominal central transmission wavelength, n_0 is the refractive index outside the filter, n_i is the effective refractive index of the filter and θ is the AOI. Consequently,



(a) (b) (c)

Figure 3.3: Photographs of the waveguide coupling stage. (a)-(b) The waveguide coupling setup. (c) An image of the input fibre-waveguide coupling taken with the Leica M125 C stereo microscope.

each diffraction order experiences a different spectral selection after which the beams are reflected by mirrors back to the grating, where they recombine into a single output mode. By carefully selecting different OPLs for each diffraction order, we can create a FTM unit where each frequency component has a distinct time delay. Consider, for example, four 0.25 nm pump channels ranging from 520.5 to 522.25 nm with 0.25 nm guard bands. Fig. 3.5b shows the AOI required to tune a BPF with a central wavelength of 522.125 nm to align with each of the four wavelength channels. Unfortunately, in our implementation, the narrow angular separation required significant propagation distances to individually resolve each diffraction order. Moreover, standard diffraction gratings exhibit a non-uniform intensity distribution across diffraction orders, leading to unequal service quality across the quantum

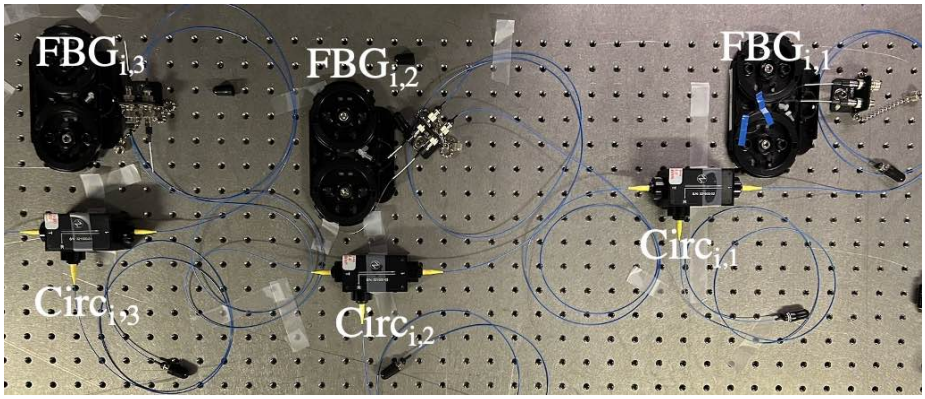
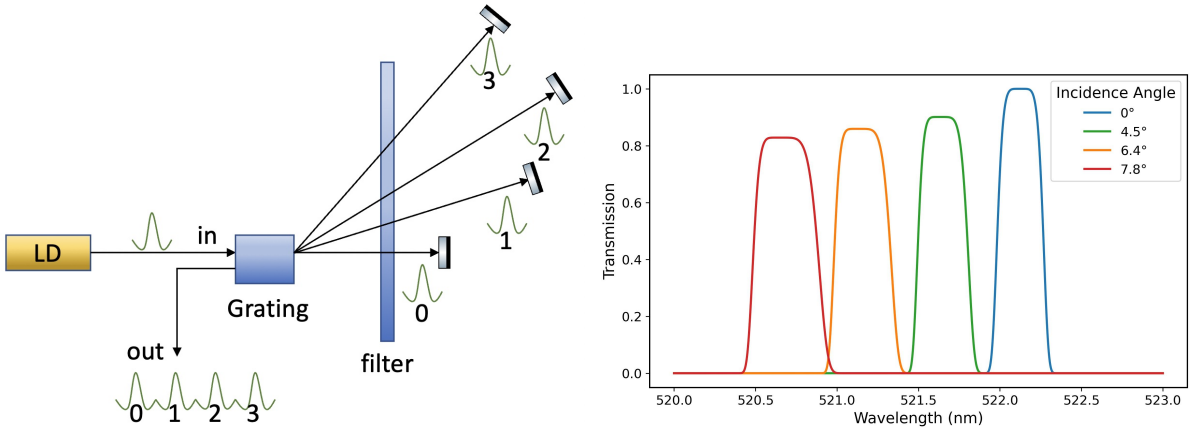


Figure 3.4: Photograph of the idler demultiplexing stage.

network. While diffractive beam splitters offer more uniform power distribution, they produce equally spaced output angles, which are incompatible with the non-uniform AOI tuning required for BPFs. Furthermore, fabricating 0.25 nm-wide BPFs is challenging. Such narrow filters are typically custom-made and not readily available off-the-shelf. At nonzero AOIs, the multilayer dielectric structure of the BPF causes Fresnel reflections at the interface of each layer, resulting in polarization-dependent effects where $s-$ and $p-$polarized light undergo different effective optical paths. This polarization splitting leads to transmission loss and distorted passbands at higher AOIs as illustrated in Fig. 3.5b [155, 156]. These combined constraints rendered the free-space FTM bulky and impractical for our intended application.

3.3 Experimental results

To demonstrate the multiplexing advantage, we measured the coincidence-to-accidental ratio (CAR) in both scenarios (Fig. 3.1a-b) using up to four correlated channels specified within the broadband spectrum of the SPDC source, see Fig. 3.2. The CAR was calculated from $\mathrm{CAR} = \mathrm{R_m}/\mathrm{R_{um}}$, where R_m and R_{um} are the coincidence rates at matched and unmatched slots as defined in [157]. The former corresponding to true coincidences caused by photons generated in the same pump pulse whereas the latter represents accidental coincidences arising from multi-pair emissions or detector dark counts. Exploiting time and frequency multiplexing at the satellite and ground nodes, accidental coincidences, due to uncorrelated channel detections, are filtered leading to a CAR improvement in accordance with the theoretical expectation as shown in Fig. 3.6a. More explicitly, one can calculate



(a) (b)

Figure 3.5: (a) Alternative implementation of the frequency-to-time mapping in free-space (b) Angle of incidence required to align a narrowband bandpass filter with central wavelength 522.125 nm and 0.25 nm bandwidth to each of the four wavelength channels spanning 520.5 nm to 522.25 nm.

the CAR from the correlated photon pair rate (μ_c), the transmittance of the signal (α_s) and idler channels (α_i), and the average signal (c_s) and idler (c_i) count rate according to:

$$\mathrm{CAR} = \frac{\mu_c \alpha_s \alpha_i}{c_s c_i} + 1. \tag{3.2}$$

Assuming N multiplexed channels, $\mathrm{CAR} - 1 \xrightarrow{\mathrm{MUX}} \frac{(\mu_c/N)\alpha_s\alpha_i}{(c_s/N)(c_i/N)} = \frac{N\mu_c\alpha_s\alpha_i}{c_s c_i}$ resulting in a linear CAR improvement [158]. To limit the cross-talk between the channels, 1 nm guard bands between the signal channels were used to limit their spectral overlap.

From the CAR, we approximate the two-photon interference visibility using the relation $V = \frac{\mathrm{CAR}-2}{\mathrm{CAR}-1}$ derived in [159]. The multiplexing scheme enhances the visibility in Fig. 3.6b, allowing increased coincidence rates at higher pump powers. To contextualize these results for practical applications, we estimate the QBER according to $\mathrm{QBER} = \frac{1-V}{2}$ and the asymptotic SKR for the entanglement-based QKD protocol outlined in [133, 134]. These results are respectively presented in Figs. 3.6c-3.6d. Again, multiplexing allows for a reduction of the QBER and a higher attainable secure key rate. This method thus presents a scalable approach to enhance the entanglement generation rate in a multipoint-to-point quantum link during the satellite pass. Moreover, additional users can be incorporated to the ground network without compromising the quality of service or pairwise entanglement

generation rate - and with minimal resource overhead. By allocating a distinct temporal window to each channel within the pulse train [49], each user can unambiguously discriminate between frequency channels using a single detector. Accordingly, coincidences, for the ground configuration at high pump power in Fig. 3.6a, were measured with only one detector channel per user. Despite the limited detection efficiency of the SNSPD at 780 nm ($\eta_{780} \sim 6\%$), temporally resolving each channel still yields a twofold CAR improvement.

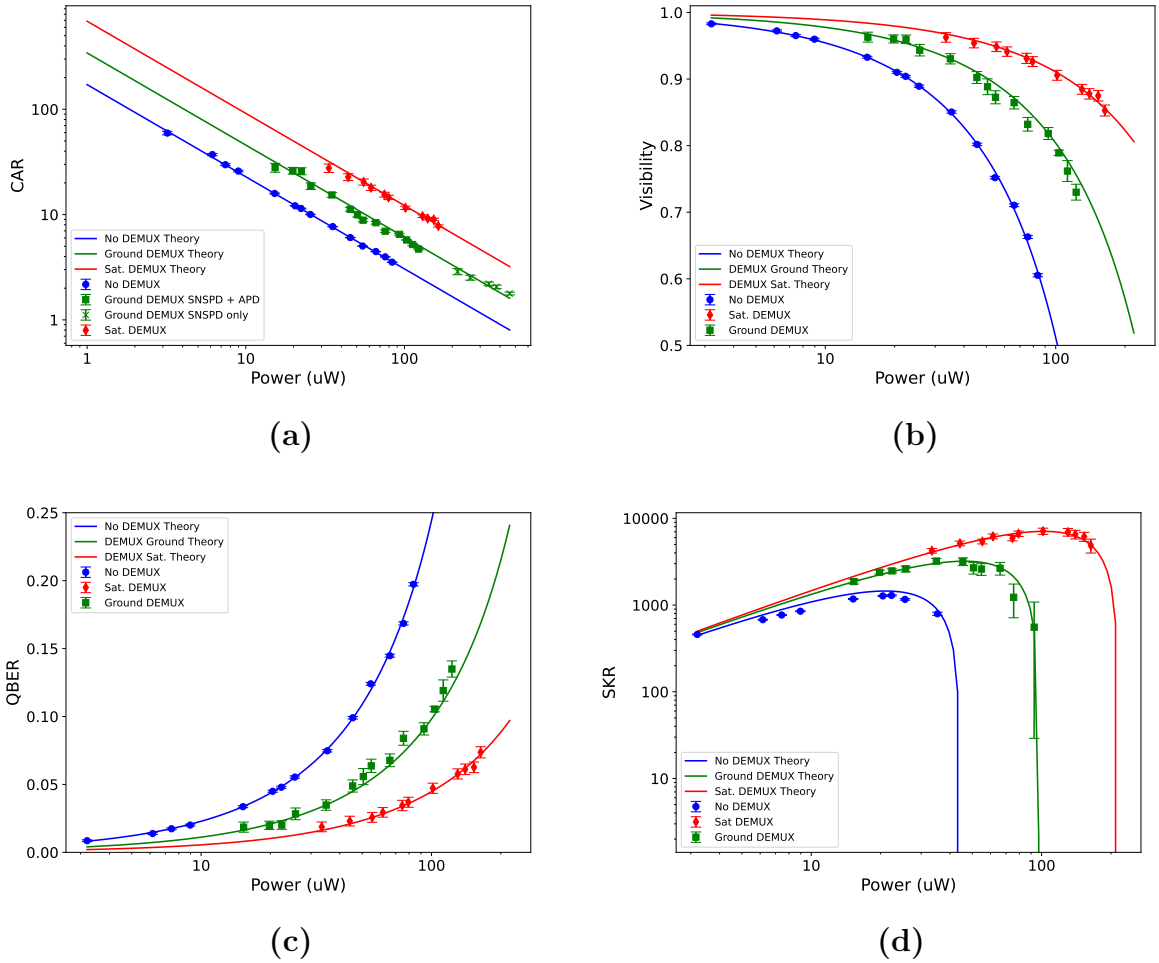


Figure 3.6: Multiplexing scheme performance estimation. In **(a)**, the coincidence-to-accidentals ratio is measured as a function of the pump power. In **(b)**, **(c)**, and **(d)** the two-photon interference visibility, QBER, and secure key rate are respectively estimated from the measured CAR. For the ground DEMUX scenario shown in **(a)**, coincidences at low pump power were measured using a SNSPD and APD detector per user, due to the SNSPD's poor detection efficiency at 780 nm. At higher pump power, signal and idler photons were jointly detected on a single SNSPD channel per user.

3.4 Discussion

3.4.1 Scaling potential

Photon bandwidth and detector timing resolution underpin, respectively, the capacity for wavelength and time multiplexing. Consequently, for the satellite configuration, the number of channels is bounded by $(R \times \delta t_j)^{-1}$, where R is the pulse repetition rate and δt_j is the timing resolution of the detection system, including synchronization-induced jitter. There is a clear compromise between the pulsed laser repetition rate and the number of available time-multiplexed channels. This trade-off is illustrated in Fig. 3.7 for our source, assuming a pump power of 100 μW, channel loss of 30 dB, detector dead time of 1 μs, 1000 counts per second dark count rate and timing jitter of 130 ps.

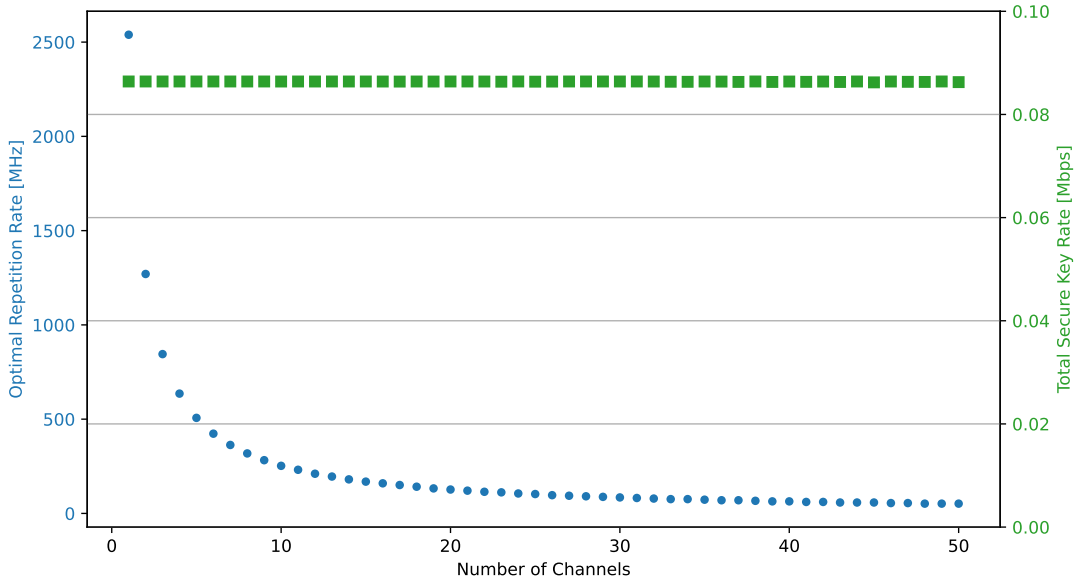


Figure 3.7: Trade-off between the number of frequency-time multiplexed channels and the repetition rate.

Owing to the requirement for spectral compatibility with the QEYSSat payload, the signal bandwidth of the ground configuration is restricted to the satellite acceptance window of 780–795 nm. Nevertheless, in contrast to the planned primary QEYSSat source [160], which is limited by its intrinsically narrow spectral bandwidth and supports essentially single-channel operation, our configuration leverages the full 15 nm acceptance

window. Assuming 100 GHz spacing between channels, this allows for up to 72 parallel channels, markedly enhancing the performance during the satellite pass. The network could be further optimized by using flexible grid technology [161]: employing a wavelength selective switch or reconfigurable optical add-drop multiplexer [162] would not only simplify the experimental design but also enable adaptive bandwidth management beyond the two configurations showcased in Fig. 3.1. Moreover, under flex-grid channel allocation, entanglement distribution losses are fixed and independent of the number of users. This provides a significant scalability advantage over the standard WDM approach.

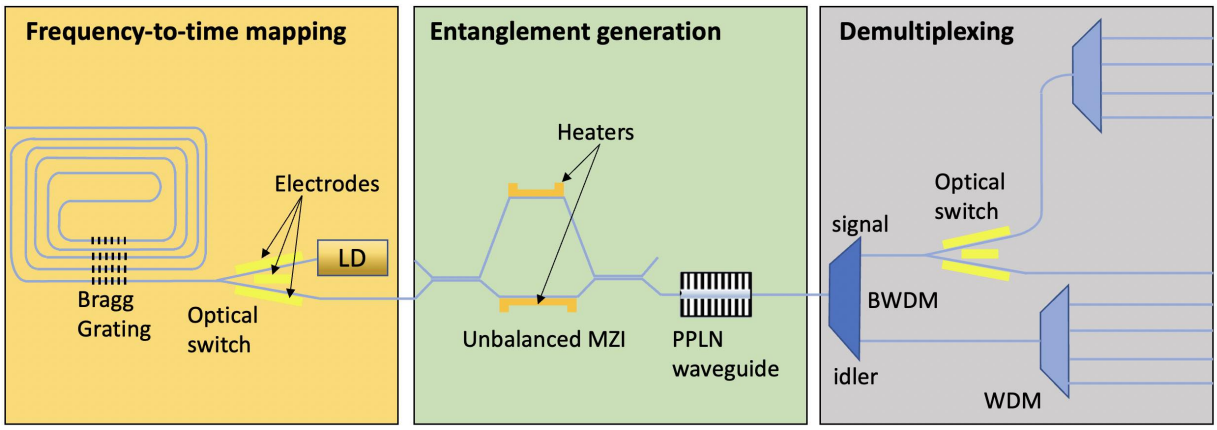


Figure 3.8: Schematic for the proposed integrated networkable quantum source.

3.4.2 Integrated source design

Compact, adaptable, and cost-effective technologies will be essential to scale quantum networks toward global deployment. However, the current design has a large form factor, as shown in Figs. 3.3 and 3.4. Recent work on integrated photonic entangled photon sources has shown significant improvements in stability, energy efficiency, and miniaturization paving the way toward scalable quantum networking systems [163, 164, 165]. Motivated by these efforts, we propose in Fig. 3.8 an integrated entangled photon source design. The design emphasizes practicality and compatibility with satellite-enabled quantum networks. To minimize size and cost, the titanium-sapphire in Fig. 3.1 is replaced by a gain-switched laser diode (LD) that produces broadband optical pulses. The frequency-to-time mapping is applied on the pump field using a Y-branched digital optical switch [166] in combination with a spiral waveguide containing an array of on-chip Bragg gratings. By encoding the FTM on the pump photons, the insertion loss associated to its optical components can

be compensated. After reflection, the temporally stretched pulse is directed through a thermally tuned unbalanced Mach-Zehnder interferometer, where a coherent superposition of early and late time-bins is encoded. The resulting pulse is then coupled into a PPLN waveguide, where time-bin entangled signal and idler photon pairs are generated via SPDC. These photon pairs are subsequently separated by a band-wavelength division multiplexer (BWDM). A second optical switch toggles between the satellite and ground configurations, rerouting the signal to a WDM for the latter. To evaluate the required guard bands for suppressing cross-talk in the frequency-to-time mapping stage, Fig. 3.9 shows a simulated joint spectral intensity (JSI) calculated from the SPDC process of the proposed integrated entangled photon source. The simulation code is provided in Appendix B. Using parameters consistent with the demonstration presented in Section 3.2, a 1.75 nm pump was divided into four frequency channels, each 0.25 nm wide. 0.25 nm spectral gaps were inserted between the Bragg grating reflection bands. This configuration was found to reduce interchannel cross-talk to below -30 dB, ensuring that the down-converted photon pairs generated from different pump channels remain spectrally and temporally well separated. This design could easily be extended to additional channels by increasing the number of Bragg gratings in the FTM unit. Such a source would enable quantum communication nodes that are portable, power-efficient, and suitable for deployment in real-world settings. The design consolidates the frequency-to-time mapping [167, 168], phase control, nonlinear photon-pair generation [169, 170, 171], and demultiplexing onto a single photonic chip [172, 173], significantly reducing size, alignment overhead, and sensitivity to environmental noise.

3.5 Summary

To conclude this chapter, we revisit some of the benchmarking metrics outlined in Section 1.2. In particular, our proposed network architecture integrates heterogeneous links in the same quantum network with minimal resource cost whilst providing continuous network uptime. Leveraging both time and frequency multiplexing, we demonstrate an increased coincidence-to-accidental ratio without additional resource overhead. In particular, as all channels are defined within the same entangled source and each user requires a single detector channel, the network scales linearly. To contextualize these experimental findings, we projected their performance in a quantum key distribution scenario and outlined a feasible route towards field deployment. The network can be easily scaled to accommodate numerous nodes and its range could be expanded using hollow core fibres [174] or quantum frequency conversion of the 785 nm signal to telecom wavelengths [149].

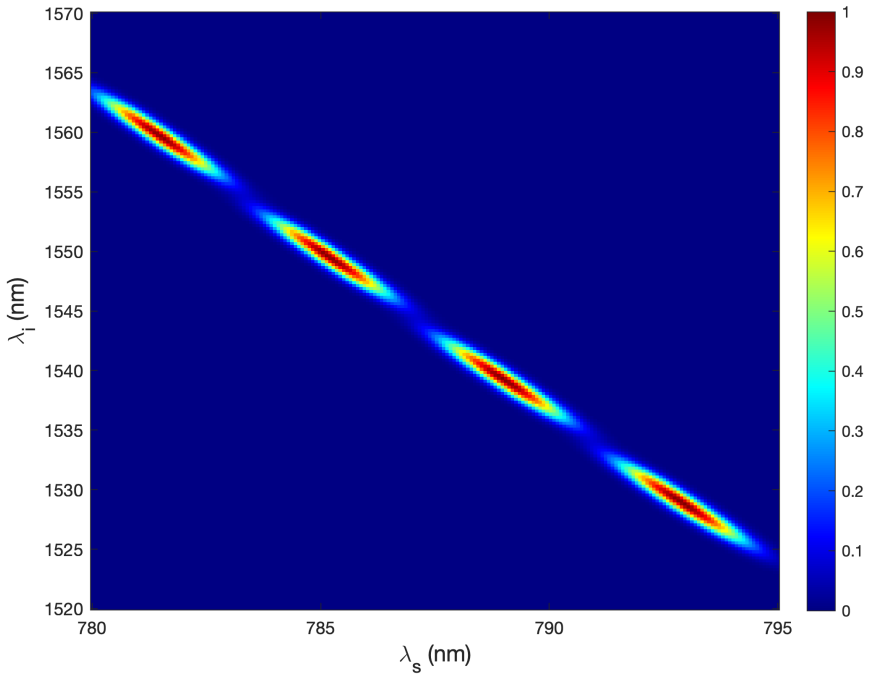


Figure 3.9: Simulated joint spectrum intensity (JSI) for the entangled photon source depicted in Fig. 3.8. Each JSI represents the spectral correlations between signal and idler photons for a specific frequency-time channel.

Chapter 4

Frequency-encoded quantum communication

This chapter is based on reference [3] and overlaps with its text.

4.1 Motivation

Initially proposed by Mérolla *et al.* in 1999 [175, 176], frequency-bin quantum information processing has garnered significant interest in the last decade due to its ease of implementation, compatibility with integrated photonic devices [177, 178, 179, 180], and its high dimensionality which allows for large alphabets [181, 182, 183, 184]. This is particularly beneficial for quantum communication as it increases the capacity of the quantum channel and enhances noise tolerance [185, 186, 187]. Frequency-bin states can be generated from compact sources, are easily manipulated using standard optical components, and the stability in their relative phase provides inherent resistance against mode mixing and phase noise in long-distance propagation. Furthermore, frequency-bin encoding has shown promise in overcoming challenges associated with solid state emitters, such as phonon dephasing and spectral diffusion, thus allowing for the generation of photonic cluster states [188, 189] and facilitating scalable quantum information processing [190, 191, 192, 193]. In particular, frequency-bins are compatible with spectrally heterogeneous matter qubits [180, 194] and support dense spectral multiplexing making them prime candidates for quantum networking. Demonstrations of narrowband frequency-bin EPSs designed to interface with atomic memories have already been reported [195, 196]. Moreover, combined with

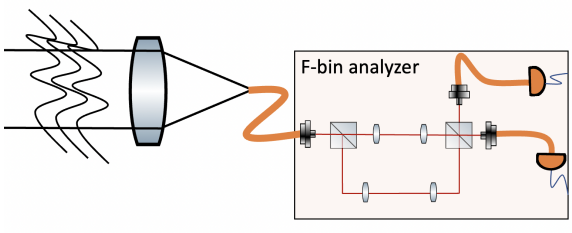


Figure 4.1: Multi-mode frequency-bin analyzer. The MM fibre input provides increased coupling efficiency and enhanced robustness to pointing errors and distorted point spread functions.

their low size, weight, and power (SWaP) footprint and vibration tolerance, frequency-bin quantum sources form an attractive option for satellite-based quantum communication.

However, frequency-bin states are typically decoded via spectral filtering [178, 197, 198], electro-optic modulation [175, 177, 199], or pulse shaping [179, 182, 200]. These techniques are lossy and require coupling into single-mode fibre hindering their applicability with free-space channels unless adaptive optics are utilized. These limitations are directly resolved by using a multi-mode (MM) analyzer as shown in Fig. 4.1. Due to their higher numerical aperture and core size, MM fibres provide an enlarged field of view and drastically increased coupling efficiency [201]. For example, with a 1-meter telescope with significant turbulence ($r_0 = 1$cm) [202], single-mode fibre coupling is limited to an efficiency of 0.04% whereas for the step-index multi-mode fibre considered here a 96.7% efficiency is achievable with tip-tilt-only corrections. Moreover, they are significantly more robust to pointing errors [203, 204] and turbulence-induced wavefront distortions [205, 206, 207, 208]. In this chapter, we propose a simple interferometric decoding method utilizing a field-widened Mach-Zehnder interferometer (MZI) which requires no modal filtering or active elements, thus providing a robust solution for spatially multi-mode channels and free-space quantum communication [209]. This passive interferometric approach offers important advantages over the established techniques for manipulating frequency-bin encoded quantum states and can be readily applied to long-distance satellite links.

4.2 Theory

4.2.1 Frequency-bin encoding

Frequency-bins are encoded in distinct spectral modes ω_n such that a dual-rail qubit can be defined from the two modes ω_0 and ω_1 as shown in Fig. 4.2 according to

$$|\psi\rangle = \alpha\,|0\rangle_L + \beta\,|1\rangle_L\,, \tag{4.1}$$

where the two modes are identical in all degrees of freedom except frequency. As the Hilbert space contains an infinite set of modes with frequency ω_n, Eq. 4.1 can naturally be extended to qudits. Practically, high-dimensional quantum states can be efficiently encoded using broadband frequency combs, with each spectral line serving as an information carrier [180]. Arbitrary quantum states can also be created from the coherent superposition of frequency-bins or from chip-scale micro-resonators, making them highly compatible with integrated photonic platforms [181, 184, 198].

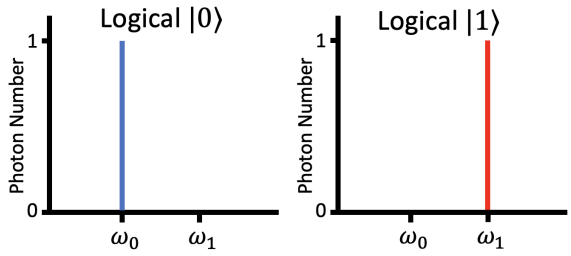


Figure 4.2: Dual-rail logical qubit encoding: a single photon corresponds to $|0\rangle$ or $|1\rangle$ depending on which frequency mode it occupies.

Yet, the ability to perform flexible and efficient operations on these states remains limited. Traditional techniques rely on active nonlinear optics to modify photon frequencies, e.g. through sum- and difference-frequency generation in $\chi^{(2)}$ media, which requires stringent phase-matching conditions and high pump powers that restrict both flexibility and scalability [210]. More recently, coherent control over frequency modes has been demonstrated using electro-optic modulators in combination with phase-shaping techniques [180, 192]. However, scaling these methods to manipulate multiple frequency modes requires intricate setups involving cascaded modulators and pulse shapers, whose configurations must be extensively optimized [200]. The disparity between the relative ease of state generation and the complexity of manipulation underscores the need for alternative strategies in frequency-domain quantum information processing.

Frequency-bin detection

Detecting frequency-bins in the computational (σ_Z) basis is straightforwardly realized either by frequency demultiplexing or frequency-to-time mapping. However, these methods provide no phase information and thus cannot resolve states in the superposition (σ_X) basis. Discriminating between superposition states is thus typically achieved via nonlinear or electro-optic mixing. This approach introduces significant losses due to the populating of higher-order sidebands outside the desired frequency range [211]. The finite bandwidth of modulators further exacerbates this issue, often introducing additional inefficiencies. Moreover, this method relies on single-spatial-mode operation, which limits its applicability in free-space channels unless adaptive optics are employed. Expanding frequency-bin compatibility to ground and satellite-based free-space channels is crucial for enabling truly global quantum networks, where atmospheric turbulence and pointing instability necessitate robust multi-mode operation to maintain high-fidelity quantum communication. Consequently in the following chapters 4-5, we will focus on a novel scheme based on passive photonic components and time-resolved detectors. Rather than relying on nonlinear or electro-optic mixing, we directly resolve the interference fringes of any given superposition state. By mapping frequency-bin modes to distinct spatial channels via linear interferometry, one can create arbitrary unitary gates on the frequency basis [211], where projective measurements are then realized by time-resolved detection of each spatial output using single-photon detectors with high temporal resolution.

For a superposition $|\Psi\rangle$ of two frequency-bins, $(A_0\hat{a}_0^\dagger + A_1\hat{a}_1^\dagger)\,|0\rangle$, the intensity measurement $\langle\hat{N}(t)\rangle$, where $\hat{N}(t) = \hat{a}_t^\dagger\hat{a}_t$, results in a beat note [212]

$$\langle\hat{N}(t)\rangle = \frac{1}{(|A_0| + |A_1|)^2}\Big(|A_0|^2 + |A_1|^2 + 2|A_0||A_1|\cos(\Delta\omega t)\Big).$$

If frequency spacing $\Delta\omega$ is sufficiently small compared to the detector's timing resolution δt_j, orthogonal superposition states can be directly distinguished from the resulting interference fringes in the photon wavepacket. The corresponding beat visibility is $v_X = \frac{2|A_0A_1|}{|A_0|^2+|A_1|^2} \cdot v_X^\epsilon$, where v_X^ϵ corresponds to the visibility due to mode-mismatch and experimental imperfections for the σ_X-basis measurement.

For the rectilinear (σ_Z) basis, an unbalanced Mach-Zehnder interferometer, with a path length difference ΔL can act as a frequency demultiplexer (DEMUX) that directs specific frequencies to designated output ports based on their relative phases. The phase shift introduced by the unbalanced MZI is given by the product of the spatial frequency (ω_i/c) and the path length difference $\phi_i = \omega_i\Delta L/c$ leading to a phase difference at the output

equal to $\Delta\phi = \phi_1 - \phi_0 = \frac{\Delta\omega\Delta L}{c} = \pi$. Consequently, an unbalanced MZI with path length different ΔL separates frequencies ω_n and ω_m according to Eq. 4.2:

$$\Delta\omega = \frac{\pi c}{\Delta L}, \tag{4.2}$$

where $\Delta\omega = |\omega_m - \omega_n|$ is the DEMUX frequency separation. A more detailed derivation of Eq. 4.2 is provided in Appendix C.1. This method extends naturally to qudits by concatenating a series of optical interleavers [213, 214] or using cascaded interferometers [215, 216].

Non-monochromatic frequency-bins

In practice, each frequency mode $|\omega_i\rangle$ is not perfectly monochromatic but has a finite bandwidth σ_i. Assuming Gaussian wave packets, each mode can be described as

$$|\omega_i\rangle = \left(\frac{1}{2\pi\sigma_i^2}\right)^{1/4} \int d\mu \exp\left(-\frac{(\mu-\omega_i)^2}{4\sigma_i^2}\right) \hat{a}_\mu^\dagger |0\rangle \tag{4.3}$$

with the creation operator $\hat{a}_\mu^\dagger$ for a monochromatic frequency mode μ as shown in Fig. 4.3. Consequently, a realistic frequency-bin superposition state can be described as

$$|\Psi\rangle = \int d\mu \left[A_0\left(\frac{1}{2\pi\sigma_0^2}\right)^{1/4} \exp\left(-\frac{(\mu-\omega_0)^2}{4\sigma_0^2}\right) + A_1\left(\frac{1}{2\pi\sigma_1^2}\right)^{1/4} \exp\left(-\frac{(\mu-\omega_1)^2}{4\sigma_1^2}\right)\right] \hat{a}_\mu^\dagger |0\rangle \tag{4.4}$$

$$= A_0 |\omega_0\rangle + A_1 |\omega_1\rangle \approx A_0 |0\rangle_L + A_1 |1\rangle_L ,$$

where $|A_0|^2 + |A_1|^2 = 1$ and the approximation $|\Psi\rangle \approx A_0 |0\rangle_L + A_1 |1\rangle_L$ holds when $\langle\omega_0|\omega_1\rangle \simeq 0$. The inner product

$$\langle\omega_0|\omega_1\rangle = \sqrt{\frac{2\sigma_0\sigma_1}{\sigma_0^2+\sigma_1^2}} \exp\left(-\frac{\Delta\omega^2}{4(\sigma_0^2+\sigma_1^2)}\right)$$

has minimal overlap when the frequency separation $\Delta\omega = \omega_1 - \omega_0$ is much larger than the frequency-bin bandwidth (i.e. $\Delta\omega \gg 2\sqrt{\sigma_0^2+\sigma_1^2}$). We now consider an intensity measurement $\hat{N}(t) = \hat{a}_t^\dagger \hat{a}_t$ with $\hat{a}_t = \int d\mu \hat{a}_\mu e^{i\mu t}$ on the state in Eq. 4.4 and obtain a time-dependent beating signal

$$F(t) \propto \langle\Psi| \hat{N} |\Psi\rangle := \frac{1}{2}(1 + v'_X \cos(\Delta\omega t)), \tag{4.5}$$

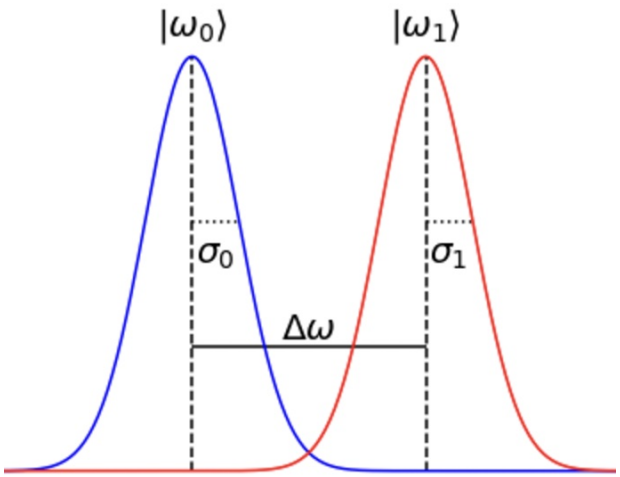


Figure 4.3: Frequency-bin encoding. Photons are encoded in spectral bands $|\omega_0\rangle$ ($|\omega_1\rangle$) with bandwidth σ_0 (σ_1) separated by $\Delta\omega$. For $\langle\omega_0|\omega_1\rangle = 0$, $|\omega_0\rangle$ ($|\omega_1\rangle$) correspond to logical bits $|0\rangle_L$ ($|1\rangle_L$).

where $v'_X = v_X \cdot \frac{2|A_0A_1|}{|A_0|^2+|A_1|^2}\left(\frac{\sqrt{2\sigma_0\sigma_1}e^{-t^2(\sigma_0^2+\sigma_1^2)}}{\sigma_0 e^{-2t^2\sigma_0^2}+\sigma_1 e^{-2t^2\sigma_1^2}}\right)$ and v_X corresponds to the visibility due to mode-mismatch and experimental imperfections.

In the σ_Z-basis, the phase shift introduced by the path length difference in the MZI depends on the bandwidth of the frequency-bin according to $\delta\phi_i = 2\pi\sigma_i\Delta L/c$ [217]. Assuming the phase shift in each frequency-bin follows a Gaussian distribution, the total phase shift variation across the two frequency-bins is then equal to $\delta\phi_T = \sqrt{\delta\phi_0^2 + \delta\phi_1^2}$ and its impact on the MZI visibility corresponds to

$$v'_Z = v_Z \exp\left(\frac{-2\pi^4(\sigma_0^2+\sigma_1^2)}{\Delta\omega^2}\right),$$

where v_Z is the visibility due to the experimental imperfections for the σ_Z-basis measurement. For practical implementations, $\sigma_0 \approx \sigma_1$ and the source's linewidth $\sigma_i \ll \Delta\omega$ is several orders of magnitude smaller than the frequency-bin separation. These bandwidth contributions to both the σ_X- (v'_X) and σ_Z-basis (v'_Z) are thus negligible.

Consider frequency-bin-encoded photonic qubits, defined as: $|\omega_0\rangle$, $|\omega_1\rangle \coloneqq |\omega_0 + \Delta\omega\rangle$, and the superposition $\frac{1}{\sqrt{2}}[|\omega_0\rangle + e^{i\Delta\omega t}|\omega_1\rangle]$, corresponding to logical bits $|0\rangle, |1\rangle, |+\rangle$ for $e^{i\Delta\omega t} = 1$. For the superposition (σ_X) basis, different frequency-bins accumulate phases at a

different rate leading to a time dependent relative phase. Consequently, in the Schrödinger picture the time evolution leads to an oscillating beat note $|\Psi(t)\rangle = \frac{1}{\sqrt{2}}[|\omega_0\rangle + e^{i\Delta\omega t}\,|\omega_1\rangle]$ around the equator of the Poincaré sphere as depicted in Fig 4.4 [211]. In spite of the phase

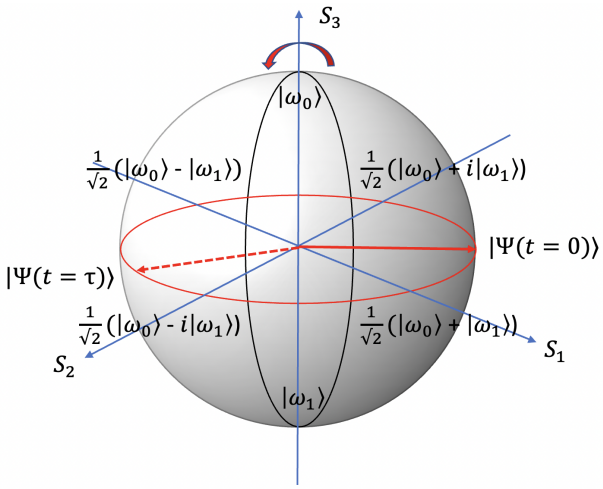


Figure 4.4: (a) Poincaré sphere. The time dependence, described in Schrödinger picture, $|\Psi(t)\rangle = \frac{1}{\sqrt{2}}(|\omega_0\rangle + e^{i\Delta\omega t}\,|\omega_1\rangle)$ leads to an oscillation around the equator at angular velocity $\Delta\omega = \omega_1 - \omega_0$ as depicted at times $t = 0$ and $t = \tau$.

oscillation of the quantum state, Pennacchietti *et al.* have shown that when the temporal resolution of the detection system is significantly smaller than the oscillation period, all photons can be used in a quantum key distribution protocol for key generation [189].

4.2.2 Timing jitter

The phase oscillation of the superposition state shown in Fig. 4.4 constrains the resolvable frequency spacing $\Delta\omega$ due to detector timing jitter. Fig. 4.5a shows the maximal visibility for a timing resolution of 100 ps as a function of $\Delta\omega$ assuming $v_X = 0.95$. Alternatively for a given frequency spacing, this constraint reduces the beat note visibility as a function of timing jitter as shown in Fig. 4.5b. To model timing jitter, the measurement outcome $F(t)$ can be described as a convolution of the beating signal $f(t) = \frac{1}{2}(1 + v_X \cos(\Delta\omega t))$ with weight function $g(t)$, where v_X is the initial visibility of the state. Assuming Gaussian $g(t)$ with timing jitter standard deviation of δt_j and adding sources of jitter in quadrature

$(\delta T = \sqrt{\sum_j \delta t_j^2})$ the measurement outcome $F(t)$ is

$$F(t) = \int g(\tau) f(t-\tau) d\tau = \int f(t-\tau) \frac{1}{2\sqrt{2\pi}} \exp[-\frac{\tau^2}{2\delta T^2}] d\tau = \frac{1}{2}[1+v_X e^{-(\Delta\omega\delta T)^2/2} \cos(\Delta\omega t)]. \tag{4.6}$$

The visibility of the beating signal is degraded as $v_X^{\text{jitter}} = v_X \exp[-(\Delta\omega\delta T)^2/2]$. We experimentally confirm this result by measuring a $\Delta f = 260$ MHz beat note using the experimental setup in Fig. 4.10 with four single photon detectors each with a different timing resolution given in Table 4.1. As the photon count rate is significantly smaller than the number of beat cycles N_b, we observe the beat note via statistical accumulation by post-processing the time-tags, referencing each detection event (t_i) to the latest synchronization marker pulse (t_m) according to

$$\Delta t_i = t_i - \max_m \{t_m | t_m \leq t_i\}, \tag{4.7}$$

where the synchronization channel provides a marker pulse with frequency $1/T_M$. Each time difference Δt_i is mapped into the beat period $T_b = T_M/N_b = 2\pi/\Delta\omega$ via

$$\tau_i = \Delta t_i \mod T_b, \tag{4.8}$$

effectively assigning a time relative to the beat period to each photon detection event. Partitioning the beat period into $K = T_b/\delta t_{\text{bin}}$ time intervals, we calculate the number of events falling within the k-th interval according to

$$N_k(T) = \sum_i \mathbf{1}_A(\tau_i), \tag{4.9}$$

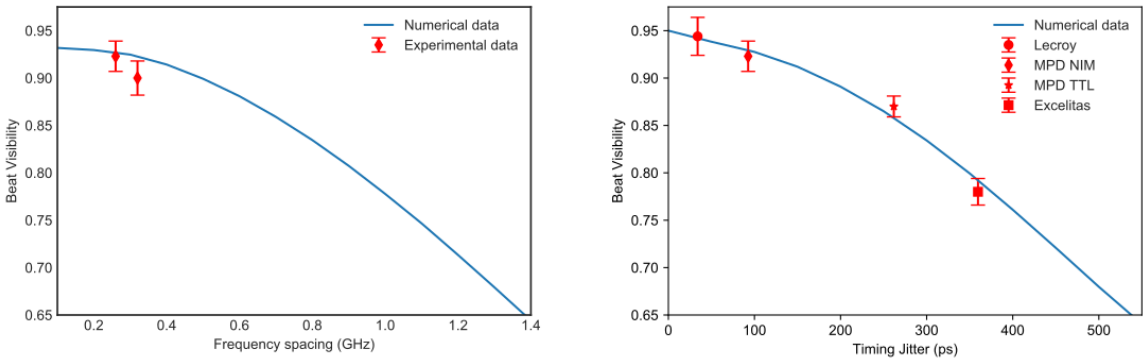
where $\mathbf{1}_A$ is the indicator function and $A = [k\delta t_{\text{bin}}, (k+1)\delta t_{\text{bin}}]$ represents the k-th bin. Summing over all intervals δt_{bin}, we create a histogram of the total events per beat period

$$N(T) = \sum_{k=0}^{K-1} N_k(T) \tag{4.10}$$

where the bin size δt_{bin} is the resolution of the time-tagger. The analysis code is provided in Appendix D.

4.2.3 Moving platforms

In non-static links, frequency-bin encoded quantum states can experience rapid phase shifts, necessitating a fast compensation system. We describe the time-dependent change



(a) Frequency spacing limitation

(b) Timing resolution limitation

Figure 4.5: Limitations on the beat note visibility due to (a) the beat note's frequency spacing for a fixed timing resolution of 100 ps, (b) the detector's time jitter for a fixed frequency spacing of 260 MHz. We assume a laser linewidth of 300 kHz [6], and a visibility of 95% at $\Delta t = 0$.

in the Heisenberg picture, where an operator $\hat{P}$ is time-dependent. Moreover, for fast moving platforms such as satellites, the position-dependent phase shift and the Doppler shift must be incorporated. For a distance $R(t)$ between the source and receiver, the operator $\hat{P}(t)$ will be given as

$$\hat{P}(t) = |P(t)\rangle\langle P(t)| \qquad |P(t)\rangle = \sum_i p_i e^{i\omega_i' \frac{R(t)}{c}} |\omega_i'\rangle \approx \sum_i p_i e^{i\omega_i (1+\frac{1}{c}\frac{\mathrm{d}R(t)}{\mathrm{d}t})\frac{R(t)}{c}} |\omega_i\rangle . \quad (4.11)$$

The Doppler effect $\omega_i' = \omega_i \left(\frac{c+v}{c-v}\right)^{1/2} \approx \omega_i(1+\frac{v}{c}) = \omega_i(1+\frac{dR(t)}{cdt})$ is negligible in satellite systems. For a LEO satellite, $\frac{dR(t)}{cdt} \approx 2.6\times10^{-5}$. For the frequency separation $\Delta\omega = 1.634\times 10^9$ rad/s used in our experiment, the Doppler shift modifies the frequency separation by 4.2×10^4 rad/s – a negligible change compared with the frequency-bin bandwidth.

Moreover, on a nonstatic platform, take as an example a projector onto a two-dimensional space spanned by $\{|\omega_0\rangle, |\omega_1\rangle\}$. The explicit time dependence of the qubit measurement is $|P(t)\rangle = \frac{1}{2}(|\omega_0\rangle + e^{i\Delta\omega(1+\frac{dR(t)}{cdt})\frac{R(t)}{c}} |\omega_1\rangle)$, where the projector evolves due to the transmitter's motion with a phase change $\Delta\omega(1+\frac{dR(t)}{cdt})\frac{R(t)}{c}$, and a phase change rate given by: $\delta f \approx \frac{1}{2\pi}\frac{d}{dt}\left(\Delta\omega(1+\frac{dR(t)}{cdt})\frac{R(t)}{c}\right)$. For a LEO satellite at perigee, approximating its distance to first order as $R(t) = vt$, where the average velocity $v \approx 6$km/s [39], a frequency-bin state of $\Delta\omega = 1.634\times10^9$ rad/s will experience a average phase change rate $\delta f \approx \frac{1}{2\pi}\Delta\omega\frac{v}{c} \approx 5$kHz.

Table 4.1: Detector models used in Fig. 4.5b and their corresponding nominal full width at half maximum (FWHM) timing resolution (δt^{FWHM}). The MPD and Excelitas detectors were used in pair with a UQD Logic16 time-tagger with a resolution of 78.125 ps [7]. A conservative upper bound for the timing resolution of the LeCroy waveRunner 640Zi used in combination with a LeCroy OE425 [8] is provided. The total resolution of the detection system (δT^{FWHM}) is estimated from the summation in quadrature of each component.

Detector Model	δt^{FWHM} (ps)	δT^{FWHM} (ps)	Measured visibility
LeCroy waveRunner 640Zi [218]	25	34	$94.4 \pm 2.2\%$
MPD PDM Series NIM output [219]	50	93	$92.7 \pm 2.7\%$
MPD PDM Series TTL output	250	262	$87.0 \pm 2.0\%$
Excelitas SPCM [220]	350	359	$77.0 \pm 2.4\%$

Table 4.2: Comparing satellite-based quantum protocols using different degrees of freedom (DOF), sensitivity quantifies how fast the compensation scheme should be.

DOF	Sensitivity	Compensation
Time-bin[228]	< 1 Hz	Phase Modulation
Frequency-bin	~ 5 kHz	GPS+ Fast Phase Modulation

A comparison with the time-bin degree of freedom is provided in Table 4.2. Without a precise time reference and phase compensation system, the measurement $\tilde{P}(t)$ is a convolution between $\hat{P}(t)$ with a rectangular function $g(t) = 1/(2T_r)$ for $t \in [-T_r, T_r]$, depending on the resolution of t quantified by T_r,

$$\tilde{P}(t) = \int \hat{P}(t-\tau)g(t)d\tau = \frac{1}{2T_r}\int_{-T_r}^{T_r} \hat{P}(t)dt \xrightarrow{T_r \gg \infty} \Delta(P(t)) \tag{4.12}$$

where $\Delta(P(t)) = \sum_i |p_i|^2 |\omega_i\rangle\langle\omega_i|$ is the completely dephasing map. Consider, for instance, the Uhlmann fidelity between the projectors $P(t)$ and $\tilde{P(t)}$: $F(t) = \left(\text{Tr}\sqrt{\sqrt{P(t)}\tilde{P(t)}\sqrt{P(t)}}\right)^2$, for $\Delta\omega = 1.634 \times 10^9$ rad/s . To maintain fidelity $F(t_i)$ above 99.9%, in the worst case scenario for the LEO orbit $R(t)$, $T_r \approx 50\mu$s is required, and thus a fast phase compensation $\frac{1}{T_r} \approx 20$ kHz is needed. Such a rapid phase shift can, however, be compensated using well-established techniques such as Global Positioning System (GPS) tracking [221, 222, 223], Satellite Laser Range (SLR) [224, 225], and more advanced laser phase tracing using frequency combs with well-defined spectral lines [226, 227].

4.3 Field-widened interferometers

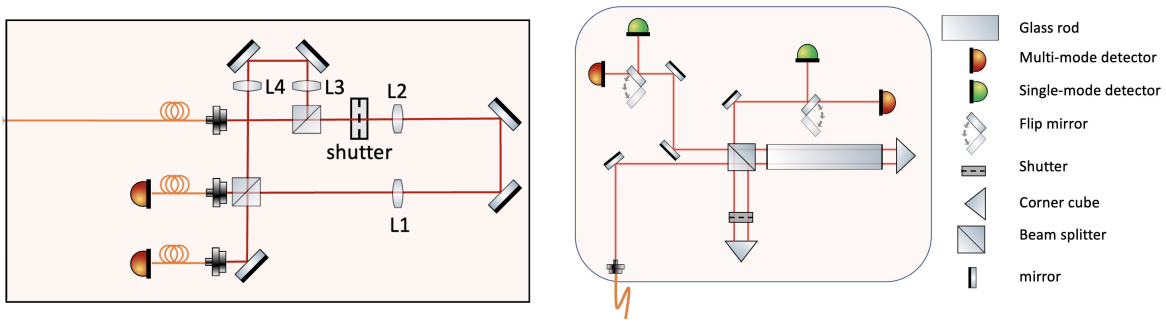
While we have shown in section 4.2.1 that unbalanced interferometers can be used as frequency analyzers for the computational basis, such analyzers are typically considered impractical for free-space channels. Indeed, mode distortions from transmission through a multi-mode optical channel [229] introduce path distinguishability in the unbalanced interferometer. This is exacerbated for mobile links, as telescope pointing errors and turbulence-induced angular fluctuations further degrade the interference quality. Moreover, spatial filters cannot address these issues without introducing significant throughput losses. FWIs have been demonstrated to function as multi-mode time-bin quantum receivers by exploiting imaging optics, or carefully selected refractive indices, to correct induced phase shifts and visibility reductions due to angular fluctuations [106, 209, 230, 231, 232, 228], which we realize can be extended to the analysis of frequency-bin receivers. We will exploit both of these techniques in sections 4.4 and 5.3.2 respectively and present both interferometric designs in Fig. 4.6.

For the relay-optics enhanced interferometer shown in Fig. 4.6a, the differences in the evolution of the spatial modes over the path length difference ΔL can be matched using a $4f$ imaging system in both arms of the unbalanced Mach-Zehnder interferometer, thus producing identical wavefronts when the paths recombine and ensuring indistinguishability at the interferometer output regardless of the spatial mode or the AOI of the input beam.

Alternatively, the combination of the glass rod and the retroreflector, in the long arm of the interferometer in Fig. 4.6b, creates a virtual mirror that appears closer to the interferometer's beam splitter. Thus by carefully selecting the glass' refractive index and length, we can match the distance from the beam splitter to this virtual mirror with the actual distance to the real mirror in the short arm, effectively balancing the interferometer [228, 233]. More specifically, consider a MZI with an input beam incident at an angle α. We can approximate the OPL difference using Snell's law and Taylor's expansion for small α, in which case [209, 234]:

$$\Delta L \approx \sum_i \left[n_{il} L_{il} - n_{is} L_{is} - \frac{n_0^2 \sin^2 \alpha}{2} \left(\frac{L_{il}}{n_{il}} - \frac{L_{is}}{n_{is}} \right) \right], \tag{4.13}$$

where l, s respectively denote the long and short arms of the interferometer and $n_{is(l)}$ the different refractive indices. To cancel out ΔL's angular dependence, we require that $\sum_i \frac{L_{il}}{n_{il}} = \sum_i \frac{L_{is}}{n_{is}}$. Solving this condition simultaneously with Eq. 4.2, one can construct a multi-mode frequency qubit analyzer. While the use of refractive index compensation can introduce some chromatic dispersion, these interferometers are significantly easier to align than relay-enhanced designs.



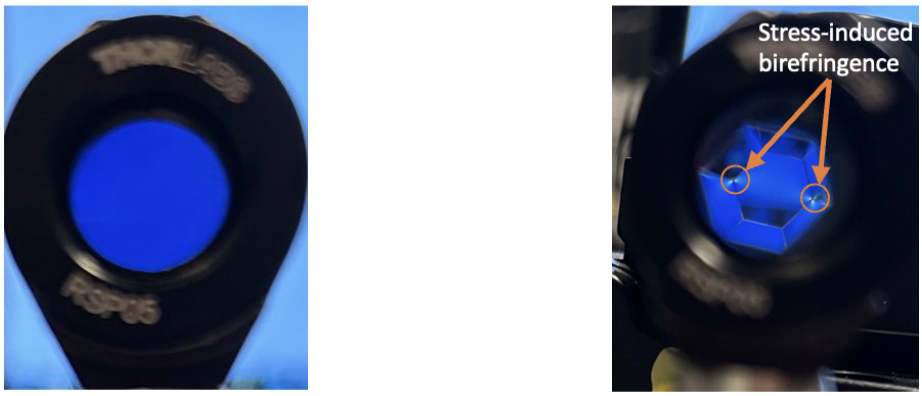
(a) (b)

Figure 4.6: (a) Relay-optics enhanced and (b) field-widened interferometer designs. For the former a $4f$ imaging system in each arm reproduces the field mode at the same position in each arm thus removing the path distinguishability. For the latter, a 10 cm BK7 glass rod is used to compensate for spatial distortions of the optical mode of the frequency-bin qubit. In both cases, the interferometer performs the σ_Z-basis projection by demultiplexing frequencies ω_0 and ω_1. The basis choice is implemented via an optical shutter in the short arm of the interferometer.

For the implementation in chapter 5, we designed two symmetric interferometers based off the design shown in Fig. 4.6b. The signal and idler f-bin analyzers in Fig. 5.3 differ only in the input fibre: single-mode for the idler and multi-mode for the signal. Solving Eqs. 4.2 and 4.13 for our optical design we obtain the following condition for the required length of glass $L_g = \frac{\pi c}{2\Delta\omega}(n_g - 1/n_g)^{-1}$, where n_g is the refractive index of the glass rod. More specifically, for the demonstration presented in Sec. 5.2, we utilized a 10 cm BK7 glass rod (*Edmund Optics TECHSPEC N-BK7 Light Pipe Homogenizing Rod*) with a 1.5007 refractive index at 1550 nm. In the long arm of the interferometer, the beam propagated in a double pass configuration through 1cm of air from the beam splitter to the glass rod, then through the 10 cm rod, followed by another 1 cm air gap between the rod and the corner cube retro-reflector for an optical path length of 34 cm. The short arm, in comparison, had a physical length of 7.85 cm resulting in an OPL difference of $\Delta L \sim 18.3$ cm corresponding to a 609.8 ps time delay or equivalently a $\Delta\omega = 2\pi \cdot 820$ MHz frequency splitting. The alignment procedure used to synchronize the optical path length differences of both interferometers is described in Sec. 5.2.1.

To characterize the polarization effects introduced by the BK7 glass rod, we performed a polarization extinction measurement as depicted in Fig. 4.8. Setting two linear polarizers (LPs) orthogonal to each other, we first measured the polarization leakage on a power meter

(*Thorlabs S122C*) and obtained a baseline of −43 dB. When the BK7 glass rod was inserted into the optical path, the leakage increased to −20 dB, suggesting that the rod perturbs the polarization state of the transmitted light. This perturbation is likely due to stress-induced anisotropy within the glass. This is directly observed by looking at a polarized light source, e.g. a computer screen in Fig. 4.7, where the screen appears uniformly blue when viewed through a polarizer in Fig. 4.7a, whereas distinct white stress patterns emerge at the mounting points of the glass rod in Fig. 4.7b. Further supporting this hypothesis, loosening the glass rod in its mount improved the extinction ratio to −29dB.



(a) (b)

Figure 4.7: Stress-induced birefringence in the glass rod. (a) Image of polarized light from a computer screen (b) same image but observed through the glass rod, revealing stress-induced birefringence along the mounting screws.

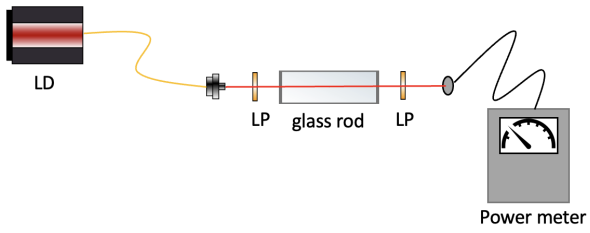
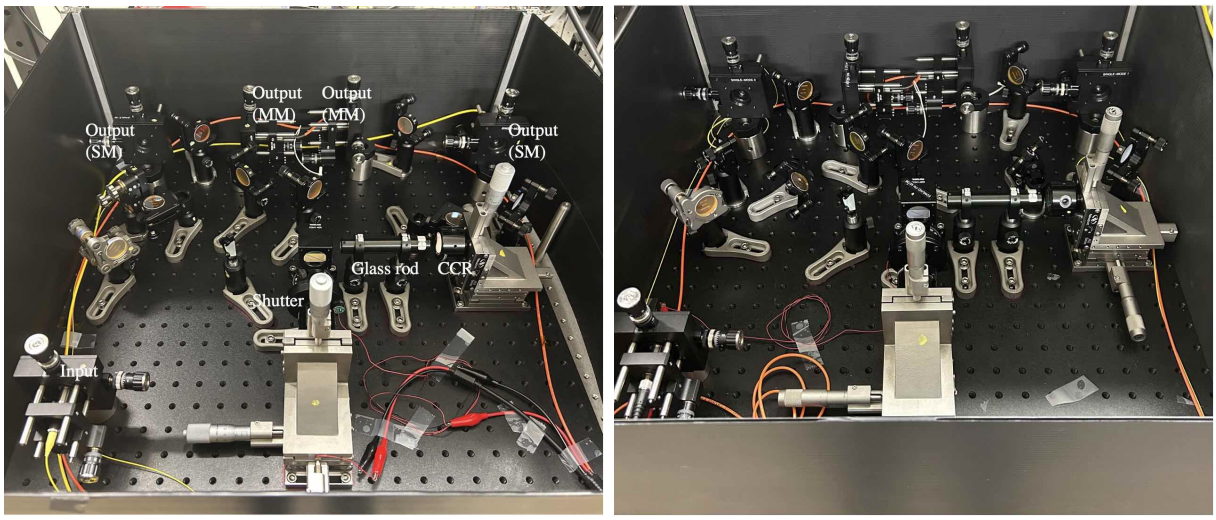


Figure 4.8: Polarization extinction measurement for the glass rod. (LD: laser diode, LP: linear polarizer)



(a) (b)

Figure 4.9: Photographs of the (a) idler photon's frequency-bin analyzer: the FWI has a single-mode fibre input, (b) the signal photon's frequency-bin analyzer: the FWI has a multi-mode fibre input (CCR: corner cube retro-reflector).

4.4 Proof-of-concept demonstration

We implemented a proof-of-principle demonstration of frequency-bin quantum communication using the setup depicted in Fig. 4.10. A continuous-wave laser (*Toptica DL-Pro*) produces a 780 nm signal, where a portion is detuned by $\Delta\omega$ to a second frequency by an acoustic-optical-modulator (*G&H AOMO 3200-124*) driven by an RF signal at a frequency of 260 MHz. Two mechanical shutters encode the frequency-bins. To generate a balanced superposition state ($A_0 \simeq A_1$), we recombine both frequency-bins at a fibre beam-splitter with appropriately adjusted coupling efficiencies at each fibre port. The encoded signal is attenuated to single photon level and sent over a two meter free-space channel to a multi-mode frequency-bin analyzer [209]. The frequency-bin generation setup is shown in greater detail in Fig. 4.11. Contrary to typical frequency-bin analyzers, our analyzer necessitates no mode filtering nor adaptive optics thus significantly improving the collection efficiency for free-space quantum channels. In the rectilinear basis, the Mach-Zehnder inteferometer operates as a frequency demultiplexer where the channel spacing is determined by the path length difference according to Eq. 4.2. The outputs are coupled into multi-mode fibres and detected with Si-APDs. For the superposition basis, a shutter blocks the interferometer's long arm and a beat note is measured at each photon detector. To track the oscillation

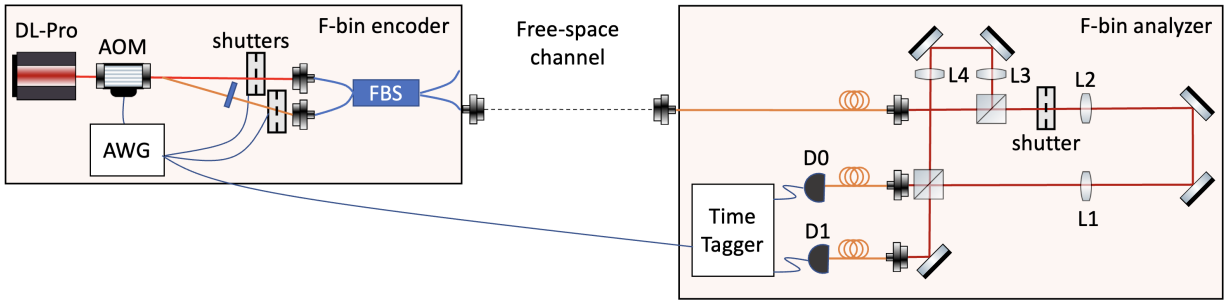


Figure 4.10: Simplified experimental setup: The DL-Pro generates 780 nm light which is modulated into two frequency-bins via an AOM driven by an arbitrary waveform generator at 260 MHz. Two mechanical shutters are used to encode the frequency-bins which are spatially combined at a polarization-maintaining fibre beam-splitter and sent across a 2 meter free-space bridge to the receiver. The frequency-bin analyzer consists of a field-widened multi-mode interferometer which is used to demultiplex the frequency-bins. The basis choice at the receiver is performed via a mechanical shutter in the long arm of the interferometer. The outputs from the frequency-bin analyzer are coupled into multi-mode fibres connected to Si-APDs. A 500 kHz marker pulse from the AWG provides a time reference to the time-tagging unit.

of the beat note, a 500kHz marker pulse is sent from the encoder's arbitrary waveform generator (AWG) (*Tabor Model WX1284C*) to the receiver's time-tagger.

We demonstrate the feasibility of our scheme by encoding a repeated sequence of $\{0, +, 1, \text{vac}\}$, depicted in Fig. 4.12a, via two mechanical shutters driven at 1 Hz by square waves $\pi/2$ out of phase. The MZI demultiplexes $|\omega_0\rangle$ and $|\omega_1\rangle$ onto detector channels 0 and 1 respectively as can be seen in Fig. 4.12b-c. Despite strong spatial distortions (see Fig. E.1a) and no active phase stabilization, we measured a visibility of 85.5% in the σ_Z basis. From the V parameter of the Thorlabs M43L01 fibre, we can estimate the number of modes $M \approx \frac{1}{2}V^2$ to approximately 4300 modes [235]. A more detailed characterization of the beam's multi-mode properties is provided in Appendix E. While perfect visibility is theoretically possible, the performance is limited due to imperfect overlap between the interfering beams in the MZI which leads to crosstalk between the inteferometer's output ports. This leakage is visible in Fig. 4.12 in the slight difference with the vacuum floor for detectors 0 (1) when only $|\omega_1\rangle$ ($|\omega_0\rangle$) is transmitted and was used to calculate the visibility according to $V_{\omega_i} = (N_{peak} - N_{leak})/(N_{peak} + N_{leak})$. The visibility could be further enhanced through more precise interferometric alignment and improved thermal stability [209]. For the superposition basis, the beat note shown in Fig. 4.13a was measured on a MPD PDM

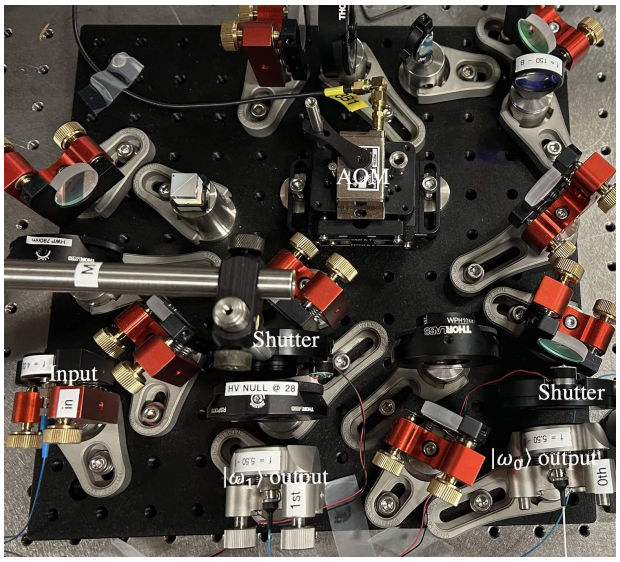


Figure 4.11: Photograph of the frequency-bin generation setup. A double-pass configuration through the AOM was used to achieve a total frequency shift of 260 MHz while driving the AOM at 130 MHz.

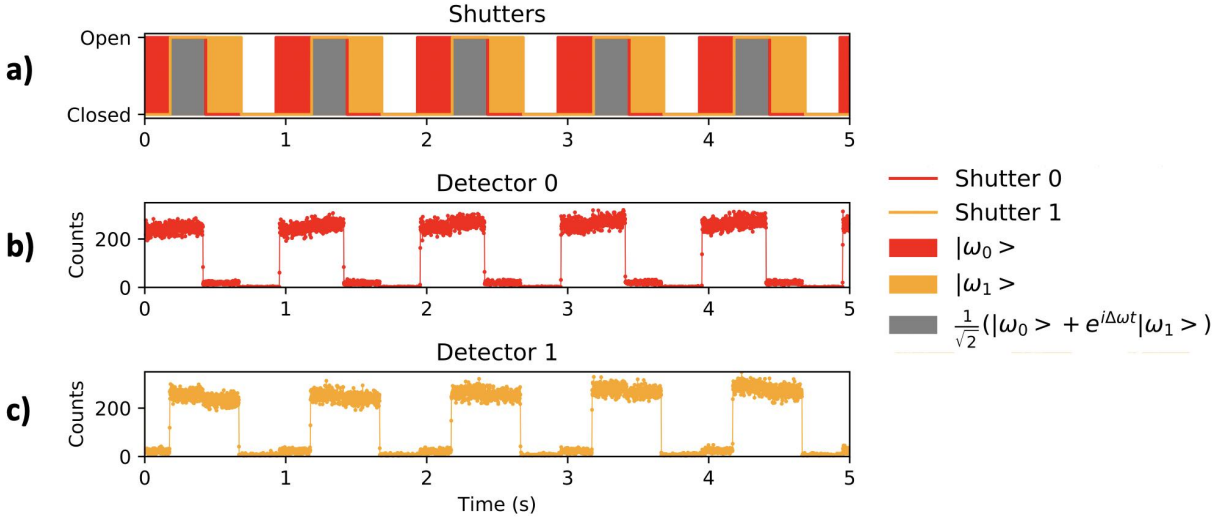
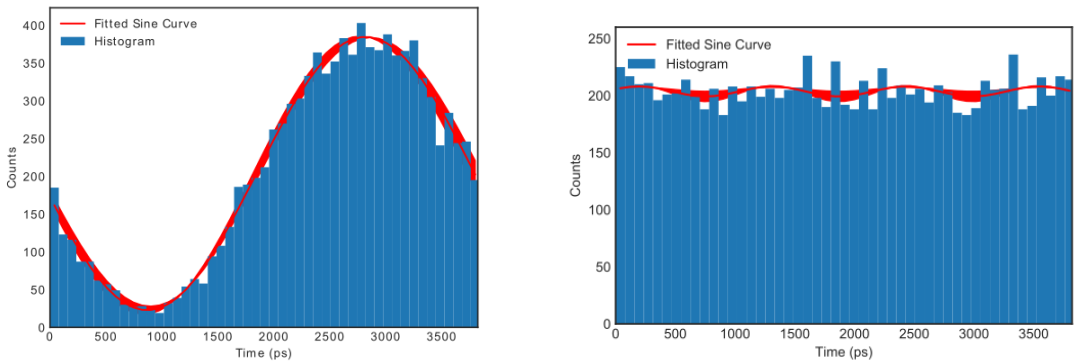


Figure 4.12: (a) Frequency-bin encoding scheme. A repeated sequence $\{|\omega_0\rangle, \frac{1}{\sqrt{2}}[|\omega_0\rangle + e^{i\Delta\omega t}|\omega_1\rangle], |\omega_1\rangle, |vac\rangle\}$ is encoded via two mechanical shutters driven by squares waves $\pi/2$ out of phase. Frequency-bin decoding scheme for the rectilinear basis: $|\omega_0\rangle$ and $|\omega_1\rangle$ are measured on detectors 0 and 1 in (b) and (c) respectively.

series single photon Avalanche Photodetector (APD) paired with a UQD Logic16 time-tagger. If the sender and receiver bases are mismatched, no beat note is observed as is the case in Fig. 4.13b. The $\sim$ 93 ps timing resolution of the detection system limited the σ_X-basis visibility, in Fig. 4.12, to $92.4 \pm 2.7\%$. The experimental parameters for our proof-of-concept demonstration are summarized in Table 4.3.

Atmospheric turbulence introduces phase noise through refractive index fluctuations that affect the optical wavefront both spatially and temporally [236]. These effects can be categorized into transverse distortions, which alter the AOI and the spatial mode profile of the beam, and longitudinal fluctuations, which result in variations of the optical path length. As demonstrated in Ref. [209], the field-widened interferometer can passively compensate for AOI variations and spatial distortions. In contrast, longitudinal turbulence causes fluctuations in the arrival time of the photons, contributing to the overall timing jitter δT. In practice, atmospheric phase noise leads to negligible timing jitter, with typical range errors of around 0.5 mm RMS (1.7 ps RMS) for ground-to-satellite measurements at elevations above 30° [237]. Furthermore, although atmospheric turbulence evolves dynamically, its characteristic timescale is set by the Greenwood frequency f_G [238, 239]. f_G is typically on the order of $0.2 - 2$ kHz for LEO satellite-to-ground quantum channels [240], which is several orders of magnitude slower than the quantum beat frequency $\Delta\omega$. Consequently, atmospheric phase fluctuations appear to be effectively static during any given detection window and do not notably degrade the observed interference visibility. Moreover, as the phase noise evolves slowly compared to the quantum signal, it will, in principle, also be tracked and corrected in real time as the clocks are synchronized - similarly to the phase shift induced by the motion of the satellite discussed in Sec. 4.2.3 - for instance by transmitting a classical reference tone and adjusting the time delay between the synchronized clocks at the sender and receiver [226, 227]. In addition to phase fluctuations, atmospheric turbulence causes temporal variations in the intensity of the received signal [241], while the background count rate remains relatively constant. These perturbations in the signal-to-noise ratio can compromise the quantum bit error rate [242, 243]. To quantify this effect, we calculate the scintillation index $\sigma_I^2 = \frac{\langle I^2\rangle - \langle I\rangle^2}{\langle I\rangle^2}$ from a 5-second segment of our data by dividing it into 100 ms intervals. We obtained a scintillation index of $\sigma_I^2 = 0.012 \pm 0.003$ consistent with weak irradiance fluctuations in a laboratory setting. Although scintillation is much stronger for satellite-to-ground links ($\sigma_I^2 \sim 0.1-1$), it mainly affects intensity and not phase coherence. As such, it does not degrade the visibility of the single-photon interference of frequency demultiplexing.

The encoding rate could be easily improved up to 50 GHz using off the shelf electro-optic intensity modulators or all-optical switches [244, 245]. While the method outlined in this chapter leveraged a prepare-and-measure scheme, it is also compatible with entanglement



(a) σ_X-basis encoding (b) σ_Z-basis encoding

Figure 4.13: Frequency-bin decoding scheme for the superposition basis. To evaluate the integrity of the quantum channel, the receiver blocks the long arm of the interferometer and measures a beat note at the photon detector. (a) If the sender prepared a state in the σ_X basis, a beat note corresponding to $\frac{1}{\sqrt{2}}[|\omega_0\rangle + e^{i\Delta\omega t}|\omega_1\rangle]$ can be observed. (b) Whenever the sender encoded in the rectilinear basis only one frequency is received and no beat note is observed. The histogram bin size corresponds to the time-tagger resolution.

distribution [198]. In fact, the resource requirement for the latter is reduced as spectrally resolved coincidence counting removes the requirement for the synchronization channel. Significant advancements have been achieved in generating two-photon frequency-bin entanglement. Techniques such as operating an optical parametric oscillator below threshold [246], filtering broadband parametric down-conversion [247], and more recently, the on-chip generation of quantum frequency combs using microring resonators [181, 184, 248, 249] have been explored. Yet these methods have typically been implemented with bin spacing of tens of gigahertz and beyond due to the resolution of dense wavelength division multiplexing filters and wavelength-selective switches [192]. Using our approach, the resolvable frequency spacing is constrained solely by the timing resolution of the detection system, enabling dense spectral multiplexing for scalable quantum networks [1, 194].

Δf	260 MHz
$\Delta\omega$	1.634×10^9 rad/s
Timing pulse repetition rate	500 kHz
Shutter repetition rate	1 Hz
ω_0 visibility	$88.9 \pm 2.8\%$
ω_1 visibility	$82.1 \pm 3.4\%$
σ_Z-basis visibility	$85.5 \pm 2.2\%$
σ_X-basis visibility	$92.4 \pm 2.7\%$

Table 4.3: Experimental parameters for the prepare-and-measure demonstration.

4.5 Conclusion

Using a purely passive frequency-bin analyzer, we demonstrate the transmission and measurement of frequency-bin encoded photons over a multi-modal free-space channel, observing quantum beats without the need for coupling into single-mode fibre. Our approach is passive, requiring no spatial filtering or adaptive optics, while maintaining a high optical throughout. The simple receiver design is well-suited for quantum communication over fluctuating channels to moving platforms, including space-based quantum communication. The compatibility of the frequency-bin encoding with solid state devices, combined with their scalability to higher dimensional states, also supports long-distance quantum information processing. Furthermore, time-resolved detection followed by active feed-forward has enabled the entanglement swapping of different colored photons [250, 251], allowing connectivity between heterogeneous network nodes. Alternatively, entanglement swapping has also been demonstrated by interfering two photons at a beam splitter followed by spectrally resolved detection [252]. In this configuration, orthogonal frequency-bin Bell states can be heralded from the quantum beating observed in the two-photon interference. Our work complements these efforts by advancing the compatibility of frequency-bin photonic qubits with realistic, multimode channels and lays the groundwork for global-scale frequency-bin quantum networking with satellites.

Chapter 5

Entanglement-based frequency-bin quantum communication

This chapter is based on reference [4] and overlaps with its text.

In the preceding chapter, we demonstrated the feasibility of frequency-bin quantum communication leveraging a prepare and measure scheme. This encoding warrants further investigation. As discussed in section 4.1, one of the motivations for frequency-bin encoding stems from the development of on-chip scalable quantum light sources offering low SWaP entangled photons easily deployable in satellite-based applications. In the following chapter, we explore the entanglement distribution of frequency-bin-entangled photon pairs generated from a silicon nitride integrated photonic circuit.

5.1 Time-resolved detection scheme

Recent advances in time-resolved measurements have enabled the characterization of frequency-mode entanglement in narrowband biphoton sources [195]. As discussed in chapter 4, one can directly measure the interference fringes in the single-photon wavepacket if the frequency spacing $\Delta\omega$ is sufficiently small relative to the jitter of the detection system ($\delta T \ll \frac{2\pi}{\Delta\omega}$). In this chapter we extend this approach to the two-photon wavepacket. The JTI captures the temporal correlations between the signal and idler photons and encodes their frequency-bin superposition state. By post-selecting on various relative time delays, one can implement arbitrary projective measurements in the equatorial plane of the Poincaré sphere. Beyond the equatorial basis, any projective measurement can be

implemented using high temporal resolution detectors in combination with linear interferometry, a notable development in this direction is presented in [211], where frequency modes are effectively mapped to spatial modes, enabling arbitrary unitary transformations. As a special case, projections onto the computational σ_Z-basis can be performed using standard demultiplexing techniques with an unbalanced MZI [3]. This approach is purely passive, requires minimal resources, and naturally extends to higher dimensions. Although, the measurement fidelity is ultimately limited by the timing jitter of the detection system, single-photon detector technologies have achieved timing resolutions as low as 3 ps full width at half maximum (FWHM) in state-of-the-art demonstrations [253] and 20-30 ps jitter in commercially available detectors [254, 255], significantly mitigating this constraint.

We here focus on implementing two simple qubit measurements using passive linear optics and time-resolved detection. Specifically, we first discuss the realization of arbitrary projective measurements in the equatorial basis via direct measurement of the joint temporal intensity of the biphoton state. The implementation of projective measurements in the σ_Z (frequency eigen-) basis using an unbalanced Mach-Zehnder interferometer is also briefly reviewed.

5.1.1 Preliminary: joint temporal intensity measurement

We pump two spectrally well-separated, high-Q microrings, labelled as R0 and R1 in Fig. 5.3a, at ω_{p_1} and ω_{p_2}, with mode spacing $\Delta\omega = |\omega_{p_2} - \omega_{p_1}|$. After coarse-graining, each ring contributes a single frequency mode, $\hat{B}_n$, obtained from the continuous frequency mode creation operators $\hat{a}_s^\dagger(\omega)$ and $\hat{a}_i^\dagger(\omega)$:

$$\hat{B}_n = \iint d\omega_s d\omega_i \phi_n(\omega_s)\psi_n(\omega_i)\delta(\omega_s + \omega_i - 2\omega_{p_n})\hat{a}_s^\dagger(\omega_s)\hat{a}_i^\dagger(\omega_i), \tag{5.1}$$

where the envelope functions $\phi_n(\omega) = \sqrt{\frac{\gamma}{2\pi}}\frac{1}{\omega-\omega_{s_n}+i\gamma/2}$ and $\psi_n(\omega) = \sqrt{\frac{\gamma}{2\pi}}\frac{1}{\omega-\omega_{i_n}+i\gamma/2}$ corresponding to Lorentzian cavity modes of linewidth γ, centered at ω_{s_n} and ω_{i_n}, respectively. Under the approximation $\Delta\omega \gg \gamma$, each envelope function defines an orthogonal mode:

$$\hat{a}_{s,n}^\dagger = \int d\omega_s \phi_n(\omega_s)\hat{a}_s^\dagger(\omega), \qquad \hat{a}_{i,m}^\dagger = \int d\omega_i \psi_m(\omega_i)\hat{a}_i^\dagger(\omega),$$

such that $[\hat{a}_{\nu,n}, \hat{a}_{\mu,m}^\dagger] = \delta_{\nu\mu}\delta_{nm}$. This condition is verified by the use of Si_3N_4 ring resonators with loaded Q-factors of $\sim 1.2 \times 10^6$ and $\sim 1.3 \times 10^6$ for the signal and idler resonances,

respectively, corresponding to an intrinsic Q-factor of $\sim 3 \times 10^6$, in addition to timing resolutions ≤ 60 ps for the detection system.

In the Heisenberg picture, all dynamics sit in the field operators and the two-photon state remains time-independent:

$$|\Phi^\theta\rangle \simeq \frac{\hat{B}_0 + e^{i\theta}\hat{B}_1}{\sqrt{2}}|vac\rangle \simeq \frac{|0_s 0_i\rangle + e^{i\theta}|1_s 1_i\rangle}{\sqrt{2}}, \tag{5.2}$$

where $|vac\rangle$ is the vacuum state and the phase θ is given by (twice) the relative phase between the pump fields driving R0 and R1. A coincident click of two time-resolved detectors on the signal arm at time t_s and on the idler arm at time t_i defines a projector:

$$\begin{aligned} |P_{s,i}(t_s,t_i)\rangle \propto & \left[\left(\hat{a}^\dagger_{s,0}e^{i\omega_{s_0}t_s} + \hat{a}^\dagger_{s,1}e^{i\omega_{s_1}t_s}\right)|vac\rangle\right] \otimes \left[\left(\hat{a}^\dagger_{i,0}e^{i\omega_{i_0}t_i} + \hat{a}^\dagger_{i,1}e^{i\omega_{i_1}t_i}\right)|vac\rangle\right] \\ \propto & \left(|0_s\rangle + e^{i\Delta\omega t_s}|1_s\rangle\right) \otimes \left(|0_i\rangle + e^{i\Delta\omega t_i}|1_i\rangle\right), \end{aligned} \tag{5.3}$$

where $\omega_{s_1} - \omega_{s_0} = \omega_{i_1} - \omega_{i_0} = \Delta\omega$. In other words, a measurement performed at time t_s (t_i) corresponds to a projective measurement upon a signal (idler) qubit state located at the equator of the Poincaré sphere with azimuthal phase $\Delta\omega\, t_s$ ($\Delta\omega\, t_i$).

Applying the projector (5.3) gives the joint temporal intensity

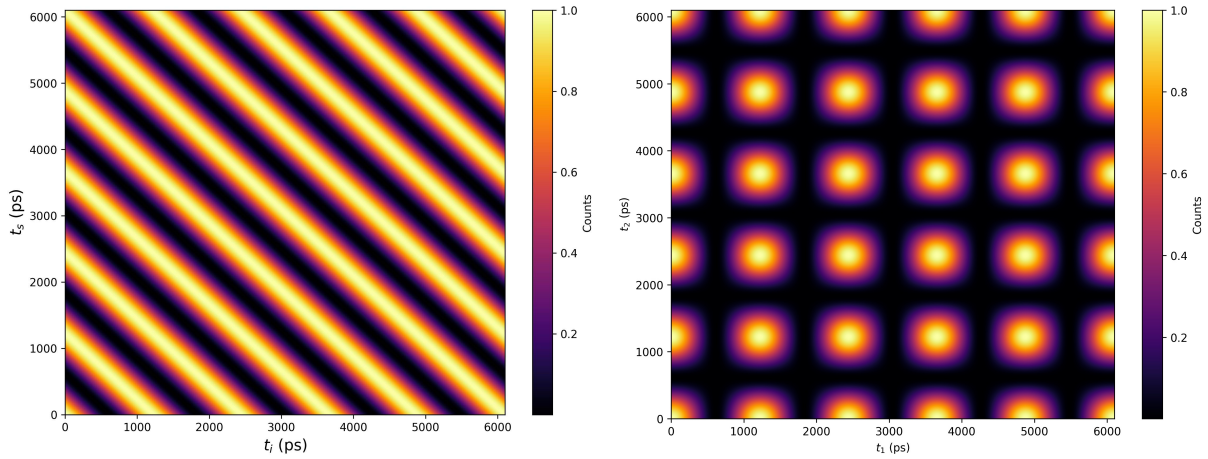
$$J(t_s,t_i) = |\langle P_{s,i}(t_s,t_i)|\Phi^\theta\rangle|^2 \propto e^{-\gamma|t_s - t_i|}\left[1 + \cos\big(\Delta\omega(t_s+t_i) + \theta\big)\right], \tag{5.4}$$

where the oscillatory term $\cos\big(\Delta\omega(t_s+t_i)+\theta\big)$ generates fast fringes along the $t_s = t_i$ diagonal. This oscillation can be interpreted as a quantum interference analogous to that observed in a Bell nonlocality experiment [256] or in Franson's scheme [257]. A visual representation of projectors $|P_{s,i}(t_s,t_i)\rangle$ is given in Fig. F.1. The JTI also exhibits a decay term related to the relative time delay $|t_s - t_i|$, which is associated with the resonator ringdown time $1/\gamma$. This decay results in an effective measurement described by a lossy projector with time-dependent efficiency $\eta(t_s,t_i) = e^{-\gamma|t_s-t_i|}$.

We show the joint temporal intensity for the limit where $\gamma \ll \Delta\omega$, in Fig. 5.1a and contrast it to the JTI obtained from the classical bichromatic pump in Fig. 5.1b. For the latter, $J(t_s,t_i) \propto \cos^2(\Delta\omega t_s)\cos^2(\Delta\omega t_i)$ results in a checkered pattern. The diagonal oscillatory behaviour of the JTI in Fig. 5.1a paired with the $\langle\sigma_Z\sigma_Z\rangle$ correlations can serve as an entanglement witness (for the classical pump $\langle\sigma_Z\sigma_Z\rangle = 0$).

5.1.2 Preliminary: interferometric σ_Z-basis measurement

As detailed in section 4.2.1, by carefully tuning the path delay of the unbalanced Mach–Zehnder interferometer, we can effectively realize projections onto $\{|0_{s(i)}\rangle, |1_{s(i)}\rangle\}$. By combining



(a) (b)

Figure 5.1: Joint temporal intensity for (a) frequency-bin entangled photons in the ideal limit where $\gamma \ll \Delta\omega$, (b) joint temporal intensity for the classical bichromatic pump.

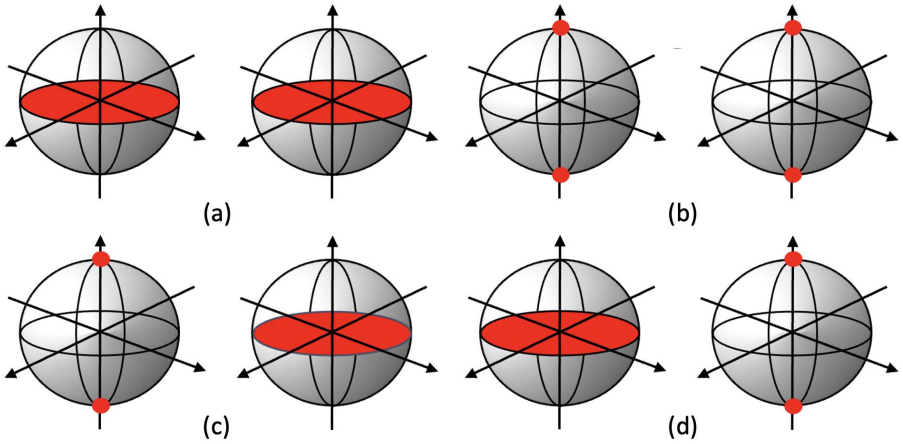


Figure 5.2: Pictorial representation of the projections for (a) the equatorial basis measurement presented in Sec 5.3.1, (b) the $\sigma_Z\sigma_Z$-basis in Sec 5.3.2 and (c)-(d) the cross-basis measurements presented in Sec 5.3.3.

measurements in the equatorial- and σ_Z-bases, as shown in Fig. 5.2, we are able to perform full quantum state tomography and demonstrate violations of both Bell and steering inequalities.

5.2 Experimental setup

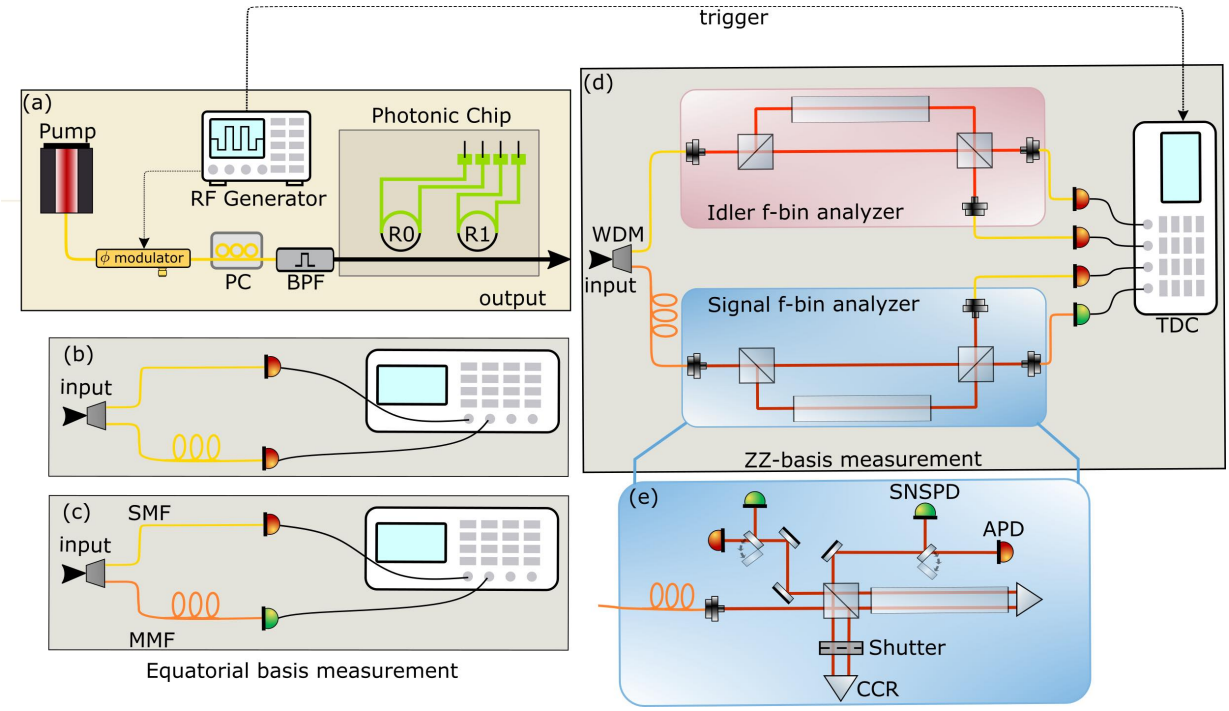


Figure 5.3: The experimental setup is broken down into five different stages: (a) the entangled photon pair generation, (b)-(d) representing three different detection scenarios, and (e) a detailed schematic of the field-widened interferometer. (b) and (c) represent a direct detection scheme for the equatorial basis measurement where the signal is detected over single- and multi-mode fibre respectively. (d) $\sigma_Z\sigma_Z$-basis measurement: the field-widened interferometers demultiplex $|0_{s(i)}\rangle$ and $|1_{s(i)}\rangle$.

A conceptual schematic of the experimental setup is shown in Fig. 5.3. The light from a tunable and continuous wave (CW) pump laser (*Santec TSL-570*) at 1550.06 nm is sent through an electro-optic modulator (EOM) (*Exail MPZ-LN-10*) driven by a sinusoidal RF

signal (*AnaPico APMS20G*) at a frequency $\Delta\omega/2\pi = 820\,\mathrm{MHz}$. The resulting bichromatic field at the modulator's output (neglecting the sidebands not used in the experiment) is then coupled to a silicon nitride (Si_3N_4) photonic chip (insertion loss: 3 dB/facet). Here, each frequency component excites a respective high-Q microring resonance previously, set at ω_{p_1} and ω_{p_2} by thermo-optic tuning, provided by integrated resistive heaters placed above each ring, with mode spacing adjusted to match $\Delta\omega = |\omega_{p_2} - \omega_{p_1}|$. Photon pair generation from spontaneous four-wave mixing occurs in both rings in a coherent superposition where each ring, respectively, generates photon pairs in the state $|0\rangle_{s(i)}$ and $|1\rangle_{s(i)}$. The integrated source design is based on a multiple-resonator approach [258, 181, 259, 198, 260], originally developed to simultaneously provide high brightness and a moderate frequency-bin spacing, accessible by commercial modulators. It consists of a sequence of two nominally identical Si_3N_4 microring resonators, each associated with a state of the computational basis, coupled to a single bus waveguide, with a cross-section $1.4 \times 0.4\ \mu m^2$. The structure is embedded in a silica cladding and light is coupled in and out from the chip with Ultra High Numerical Aperture (UNHA4) fibre array. The microrings spectral brightness is estimated to be between $5 \times 10^5\,\mathrm{cps/mW^2/GHz}$ and $5.5 \times 10^5\,\mathrm{cps/mW^2/GHz}$. The CAR$\sim 4$ is limited by spontaneous Raman scattering in the silicon nitride and in the UNHA4 fibre.

A marker pulse at $\Delta\omega/40\pi = 41\,\mathrm{MHz}$ provides a time reference to the time-tagging unit (*Swabian instruments Time Tagger X*). While this implementation relies on a shared timing signal, the experimental configuration could be simplified by presharing a reference clock. This could be achieved via GPS-based synchronization, by using high-precision local optical clocks or via the bichromatic pump itself which could be used as a stable optical reference for clock synchronization. In addition to simplifying the setup, such approaches could reduce the overhead of the protocol, in particular, for long distance links. The modulation index is adjusted to obtain sidebands that equalize the probabilities of generating a photon pair in each ring. Assuming the pump power is sufficiently low to suppress multi-pair emissions, the generated frequency-bin state can then be approximated by the Bell state given in Eq. 5.2. A dense wavelength-division demultiplexer (WDM) separates the idler at 1548.5 nm (ITU channel 36) and the signal at 1551.7 nm (ITU channel 32) photons which are then routed to three different detection scenarios.

Measurements for the equatorial basis, in Figs. 5.3b-c, were performed by time-resolved detection of the interference fringes as described in Sec. 5.1.1. In Fig. 5.3b, the signal photons are coupled into single- (*Thorlabs SMF-28*) mode fibre and detected directly using a SNSPD whereas for Fig. 5.3c, the signal photons are coupled into multi- (*Thorlabs GIF625*) mode fibre and detected on a multi-mode indium gallium arsenide (InGaAs) APD (*MPD PDM-IR*). In both scenarios, idler photons are coupled into single-(*Thorlabs SMF-28*) mode fibre and detected on a SNSPD (*PhotonSpot*) channel. The third measurement,

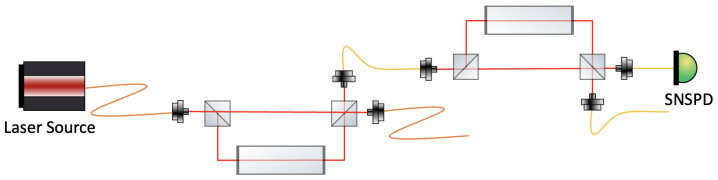


Figure 5.4: Experimental setup for the time-of-flight interferometric calibration.

in Fig. 5.3d, corresponds to the σ_Z-basis and is performed using a Mach-Zehnder interferometer (shown in Fig. 4.6) to demultiplex $|0\rangle_{s(i)}$ and $|1\rangle_{s(i)}$. In addition, cross-basis measurements were performed, in which one qubit was measured in the σ_Z basis and the other in the equatorial basis, although this configuration is not explicitly shown in Fig. 5.3. To reduce the dark count rate, the InGaAs APD was operated in an externally gated mode, triggered by the idler SNSPD.

5.2.1 Interferometric alignment

To calibrate the optical path length difference ΔL in both MZIs, we first performed a time of flight (TOF) measurement in Waterloo. Pulses generated from a ID300 laser (*ID Quantique*) were sent through a cascaded configuration of signal and idler interferometers. By selectively blocking the short and long arm of each interferometer, we were able to isolate the four possible path combinations: early-early (EE), early-late (EL), late-early (LE), and late-late (LL). Each combination correspond to a different optical path and produces a distinct arrival time at the SNSPD. The resulting time-of-flight distribution is shown in Fig. 5.5. By post-processing the time-tags and calculating the delay between the EL and LE pulses, we can estimate the ΔL mismatch between the interferometers. In this case, we find a 2.68 ps delay between the centroid of Gaussian functions fitted to the EL and LE pulses corresponding to a OPL difference of 0.8 mm.

The interferometers were then packaged and shipped for testing at the Università di Pavia. We adopted a slightly different approach to recalibrate them in Italy. More specifically, we operated the Santec TSL-570 laser in continuous linear scan mode to carefully match the optical path length difference in both interferometers. Similarly to Fig. 5.4, the laser output was injected through both MZIs sequentially. The interference signal at the output was monitored on a fast mixed-domain oscilloscope (*Tektronix MDO3034*). As the laser frequency was swept at a rate of 10 nm/s, each interferometer produced a periodic transmission pattern corresponding to its individual free spectral range (FSR),

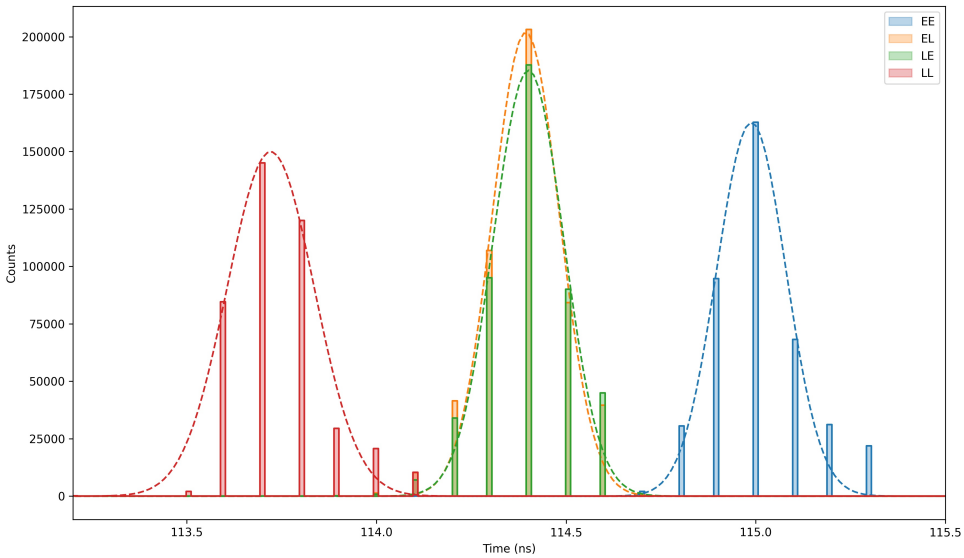


Figure 5.5: Time-of-flight measurement for the two MZIs. Gaussian functions were fitted to the early-early (EE), early-late (EL), late-early (LE) and late-late (LL) pulses.

determined by its path length difference ΔL. Consequently, by suppressing the resulting beat note from mismatched FSRs, we were able to carefully match the optical delays in both interferometers.

5.3 Source characterization

5.3.1 Equatorial basis measurement

We measured, to the best of our knowledge, the first joint temporal intensity for frequency-bin entangled photons in Fig. 5.6b. The measured joint temporal intensity shows excellent agreement with the theoretical expectation shown in Fig. 5.6a. The oscillatory term $\cos\big(\Delta\omega(t_s+t_i)+\theta\big)$ along the diagonal of the JTI, shown in Fig.5.6c, has a beating visibility of 91.9(9)%, calculated by integrating along the anti-diagonals with a range $|t_s - t_i| \leq 800$ ps. Importantly, the temporal oscillation appears only in the coincidence counts, and should therefore be regarded as a property of the two-photon state, while the single counts, related to the marginal states, remain flat, thus highlighting the two-photon, non-classical nature of the interference. The anti-diagonal profile of the JTI is shown in Fig. 5.6d and

follows the exponential envelope $e^{-\gamma|t_s-t_i|}$, with ringdown time $1/\gamma = 583.3(9)$ ps. The analysis code is provided in Appendix F.

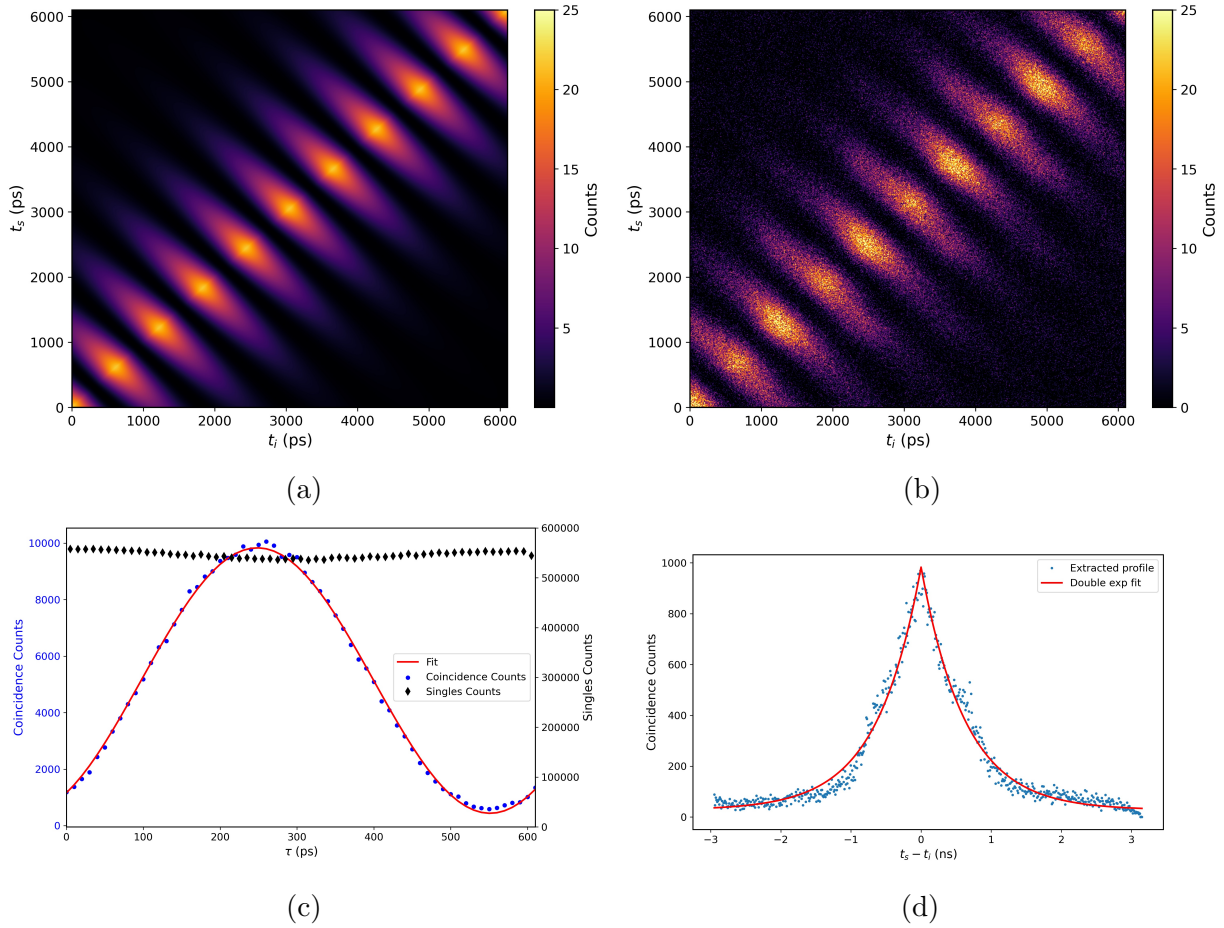


Figure 5.6: Joint temporal intensity. (a) Theoretical JTI for $1/\gamma = 581.4$ ps, the counts were scaled to match the experimental data, (b) Measured JTI over single-mode fibre, with a fitted ringdown time $1/\gamma_{fit} = 581.3(9)$ ps^{-1}, (c) diagonal profile of the measured JTI, a biphoton temporal beating can be observed in the coincidences whereas the singles exhibit no oscillation highlighting the non-local nature of the correlations, (d) antidiagonal profile of measured JTI, the cavity lifetime leads to a double exponential decay proportional to γ.

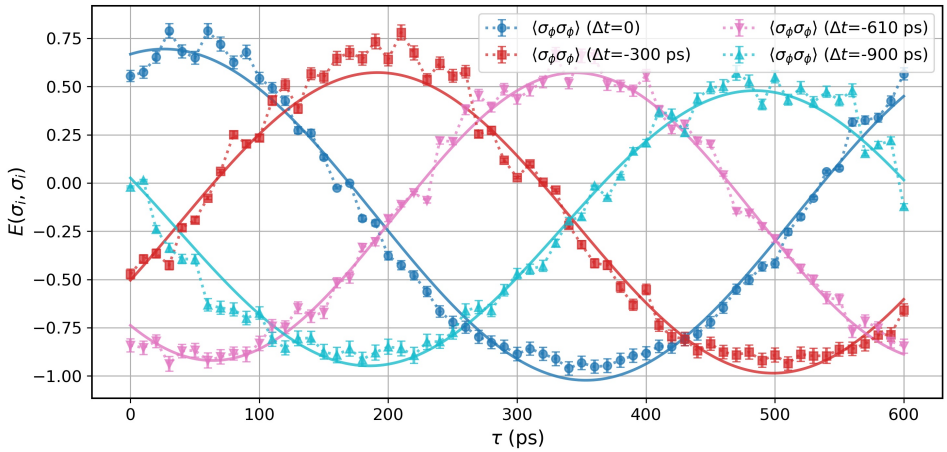


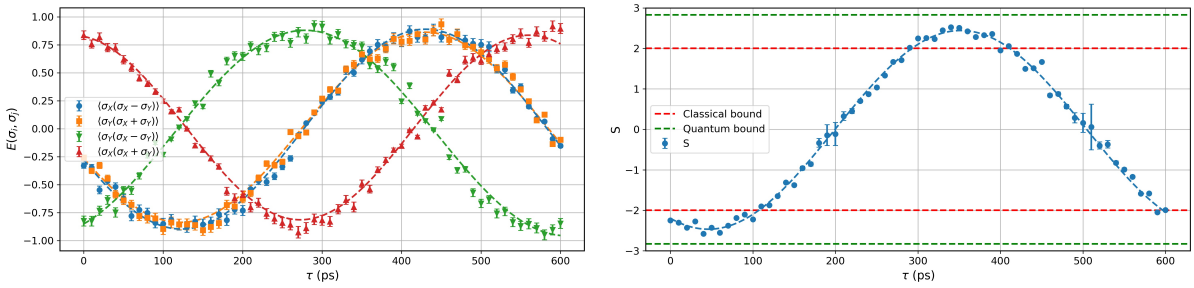
Figure 5.7: Correlation function $\langle \sigma_\phi \sigma_\phi \rangle$ as a function of the absolute time τ for different relative time delays $\Delta t = t_s - t_i$. Here ϕ denotes the azimuthal angle on the equator of the Poincaré sphere. Due to the cavity lifetime, the amplitude of the oscillation decays proportional to $|t_s - t_i|$ suggesting under-corrections in our time-dependent detector modeling. The time axis spans 0 to 610 ps, corresponding to one beat period $T_b = \pi/\Delta\omega$.

Correlation fringes

For a fixed relative time delay $\Delta t = t_s - t_i$, the two-photon correlation (as shown in Fig. 5.8a for $t_s - t_i = 0$) is analogous to that obtained in polarization entanglement where the joint detection time, $\tau \mod T_b$, $T_b = \frac{\pi}{\Delta\omega}$, defines the relative phase of the Bell-basis projection. Alternatively, the phase setting can also be adjusted by tuning the relative arrival time of the signal and idler photons with respect to the phase modulation signal. Using this latter approach, the correlation fringes for different Δt are plotted in Fig. 5.7. There is a drop in fringe visibility with increasing Δt due to an undercorrection of the decay induced by the finite cavity lifetime.

We can then use these correlations between the detection times to test for quantum nonlocality [195]. In particular, we consider the CHSH inequality [102] defined in Eq. 1.1. Fig. 5.8 shows the CHSH parameter S and the Bell correlations $\langle A_i B_j \rangle$, $(i, j \in \{0, 1\})$ as a function of detection time τ. Note that, we choose the measurement operators $A_0 = \sigma_X, A_1 = \sigma_Y, B_0 = \frac{1}{\sqrt{2}}(\sigma_X - \sigma_Y), B_1 = \frac{1}{\sqrt{2}}(\sigma_X + \sigma_Y)$, i.e. all our measurements are in the equatorial plane of the Poincaré sphere. To optimize the timing resolution of the detection scheme, we first consider projections only onto SNSPD channels, and obtain $S = 2.53 \pm 0.03$, at $\tau = 340$ ps, which violates the classical limit by $\sim 18\sigma$. Note that due

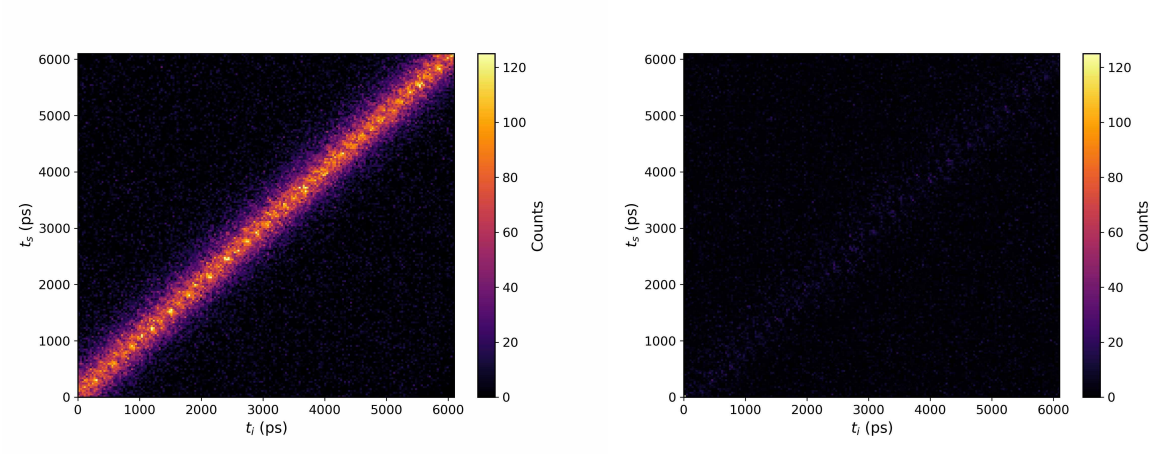
to the low CAR ~ 4, we applied a background subtraction to the raw coincidence counts to compensate for uncorrelated events and accurately estimate the CHSH parameter. We also observe a $\sim 6\sigma$ violation over multimode fibre, with $S = 2.32 \pm 0.05$. The primary difference in this case is the reduced statistics, due to the low detection efficiency of the InGaAs APD.



(a) (b)

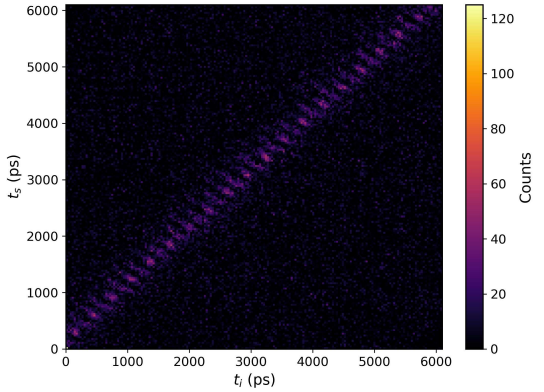
Figure 5.8: CHSH Bell inequality for frequency-bin entangled photons. (a) Expectation values $\langle A_i B_j \rangle$, $i, j \in \{0, 1\}$ for $\Delta t = 0$, and (b) Bell parameter S as a function of detection time τ. The time axis spans 0 to 610 ps, corresponding to one beat period $T_b = \pi/\Delta\omega$.

5.3.2 $\sigma_Z\sigma_Z$-basis

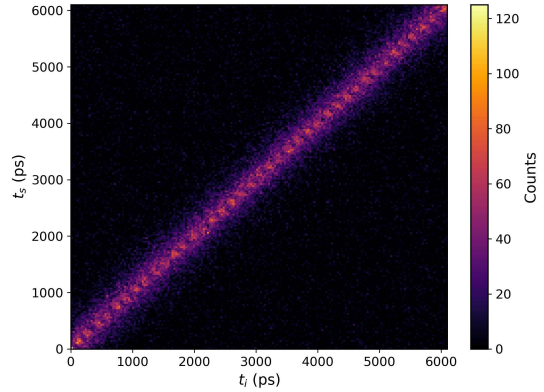


(a) C_{00}

(b) C_{01}



(c) C_{10}



(d) C_{11}

Figure 5.9: $\sigma_Z\sigma_Z$-basis measurement. Counts C_{ij}, for $i, j \in \{0, 1\}$, in (a) through (d) correspond to the projections $|00\rangle\langle 00|$, $|01\rangle\langle 01|$, $|10\rangle\langle 10|$, $|11\rangle\langle 11|$ respectively. Note that detections C_{i1} were taken with the InGaAs APD.

Fig. 5.9 shows the joint temporal intensitys for $\sigma_Z\sigma_Z$-basis measurement, where the four detection outcomes C_{ij}, $i, j \in \{0, 1\}$ correspond to the $|ij\rangle$ projections. The corresponding counts for each projection are given in Table 5.1. Despite significant spatial distortions (see Fig. E.2a), the demultiplexing visibilities of the single- and multi-mode interferometers

Projections	$\|00\rangle\langle 00\|$	$\|10\rangle\langle 10\|$	$\|01\rangle\langle 01\|$	$\|11\rangle\langle 11\|$
C_{ij}	264897	11011	25411	270383

Table 5.1: $\sigma_Z\sigma_Z$ measurement statistics. The counts were normalized by the channel efficiency and the integration time was 60 seconds. A detailed breakdown of the channel losses is given in Table 5.2.

were, respectively, 92% and 83%. The optical throughput of the interferometers were limited by optical surface losses to ~ 5 dB (see Table 5.2). Although the optical shutter in the short arm of each interferometer can implement an active basis choice between the two measurements, the interferometers were circumvented for the equatorial basis, as shown in Fig. 5.3b-c, to minimize the insertion loss and optimize the coincidence-to-accidentals ratio (CAR). The throughput and visibility of the interferometers could be improved through more careful optical design, including optimized spatial mode overlap, symmetric mode-matching optics, and enhanced thermal stability. In our implementation,

Channel	Interferometer loss (dB)	Detector efficiency (%)	η_T
SM MZI Output 1	5.1	0.85	0.2635
SM MZI Output 2	5.3	0.85	0.2499
MM MZI Output 1	10.7	0.85	0.07225
MM MZI Output 2	5.4	0.15	0.0429

Table 5.2: Channel efficiencies for the σ_Z-basis measurements.

both interferometers operated without active phase stabilization, which constrained the measurement integration time. Indeed, the phase in each interferometer drifts randomly according to environmental fluctuations. If both phase shifts follow a random walk, the variance of the interferometers' relative phase $\Delta\phi(t)$ grows linearly over time which leads to an exponential decay of $\langle\sigma_Z\sigma_Z\rangle$ as observed in Fig. 5.10. Specifically, $\langle\sigma_Z\sigma_Z\rangle(t)$ decays proportionally to $\langle\sigma_Z\sigma_Z\rangle(t=0)\times e^{-2Dt}$, where D is the diffusion constant reflecting the phase noise introduced by the environment.

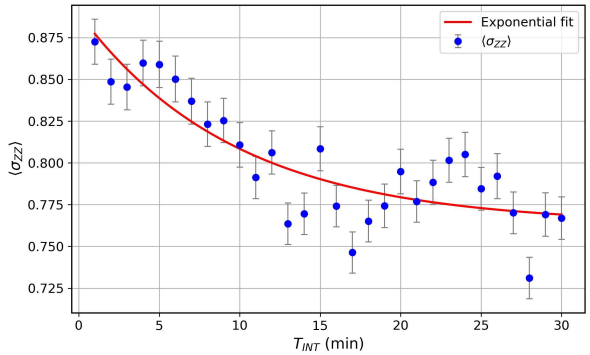


Figure 5.10: $\langle\sigma_Z\sigma_Z\rangle(t)$: phase fluctuations in both interferometers lead to an exponential decay of $\langle\sigma_Z\sigma_Z\rangle$.

Evidently, active phase stabilization would enable extended integration times sufficient to compensate for the interferometers' insertion loss without compromising the CAR.

5.3.3 Cross-basis (Equatorial-σ_Z-basis)

To be tomographically complete, we must also consider the cross-basis measurements between the equator and the poles of the Poincaré sphere (Fig. 5.2c-d). In this scenario, the four projectors corresponding to measurements where only the idler or the signal photon are demultiplexed can be defined as:

$$|\psi_{0_i}(t_s)\rangle\langle\psi_{0_i}(t_s)| \quad \text{for} \quad |\psi_{0_i}(t_s)\rangle = \left(|0_s\rangle + e^{i\Delta\omega t_s}|1_s\rangle\right)\otimes|0_i\rangle \tag{5.5}$$

$$|\psi_{1_i}(t_s)\rangle\langle\psi_{1_i}(t_s)| \quad \text{for} \quad |\psi_{1_i}(t_s)\rangle = \left(|0_s\rangle + e^{i\Delta\omega t_s}|1_s\rangle\right)\otimes|1_i\rangle \tag{5.6}$$

$$|\psi_{0_s}(t_s)\rangle\langle\psi_{0_s}(t_s)| \quad \text{for} \quad |\psi_{0_s}(t_i)\rangle = |0_s\rangle\otimes\left(|0_i\rangle + e^{i\Delta\omega t_i}|1_i\rangle\right) \tag{5.7}$$

$$|\psi_{1_s}(t_s)\rangle\langle\psi_{1_s}(t_s)| \quad \text{for} \quad |\psi_{1_s}(t_i)\rangle = |1_s\rangle\otimes\left(|0_i\rangle + e^{i\Delta\omega t_i}|1_i\rangle\right). \tag{5.8}$$

Similarly to Sec 5.3.2, the JTI in this case is $\propto e^{-\gamma|t_s-t_i|}$, with no oscillation along the diagonal. This can be readily seen from applying the projectors in Eqs. 5.5-5.8 to the state defined in Eq. 5.2. We present the JTIs associated to these measurements in Figs. 5.11a-5.11d. By post-selecting on detection times t_i and t_s we can implement projections in the $\sigma_Z\sigma_X, \sigma_Z\sigma_Y, \sigma_X\sigma_Z, \sigma_Y\sigma_Z$ bases as required for quantum state tomography.

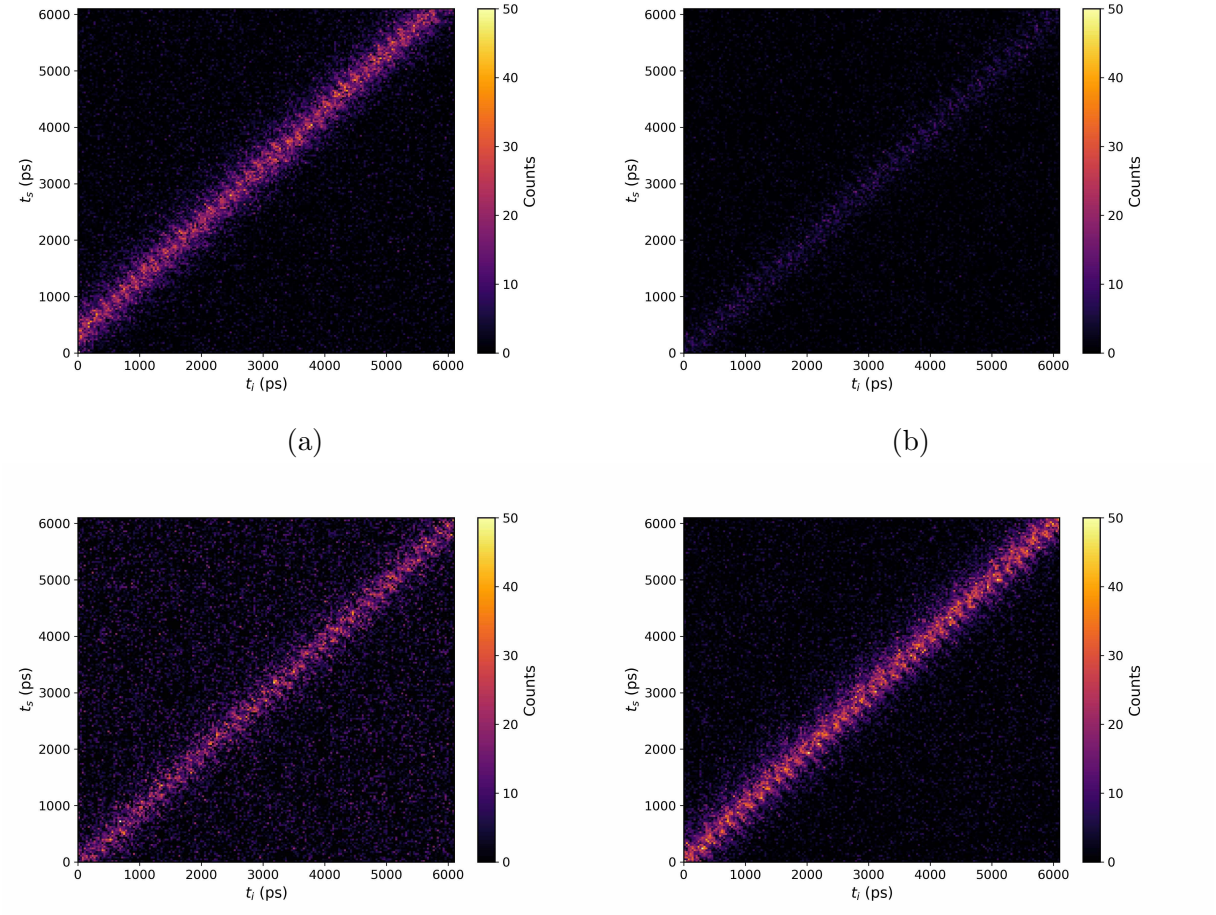


Figure 5.11: In (a) and (b) the equatorial-basis measurement was done with the MPD and the Z-basis measurement was done with the SM-MZI for $|0_i\rangle$ and $|1_i\rangle$ respectively. In (c) and (d) the MM-MZI implemented the Z-basis measurement (for $|0_s\rangle$ and $|1_s\rangle$ respectively) and the equatorial-basis measurement was done with an SNSPD detector.

5.4 Results

5.4.1 Quantum State Tomography

To assess the performance of our time-resolved detection scheme, we performed quantum state tomography. The temporal resolution of our detection scheme enables us to extract the full set of time correlations required for complete state reconstruction using only four physical measurement settings. Using a standard maximum likelihood estimation, we reconstruct a density matrix, shown in Fig. 5.12, with an Uhlmann fidelity up to 91(1)% to the Bell state $|\Phi^+\rangle$ and a purity of 84(2)% over the single-mode channel. Over multi-mode fibre, the reconstructed density matrix had a fidelity of 85(2)% with respect to $|\Phi^+\rangle$ with a purity of 78(3)%. A summary of the quantum state tomography fidelities and the CHSH values for the single- and multi-mode scenarios is presented in Table 5.3.

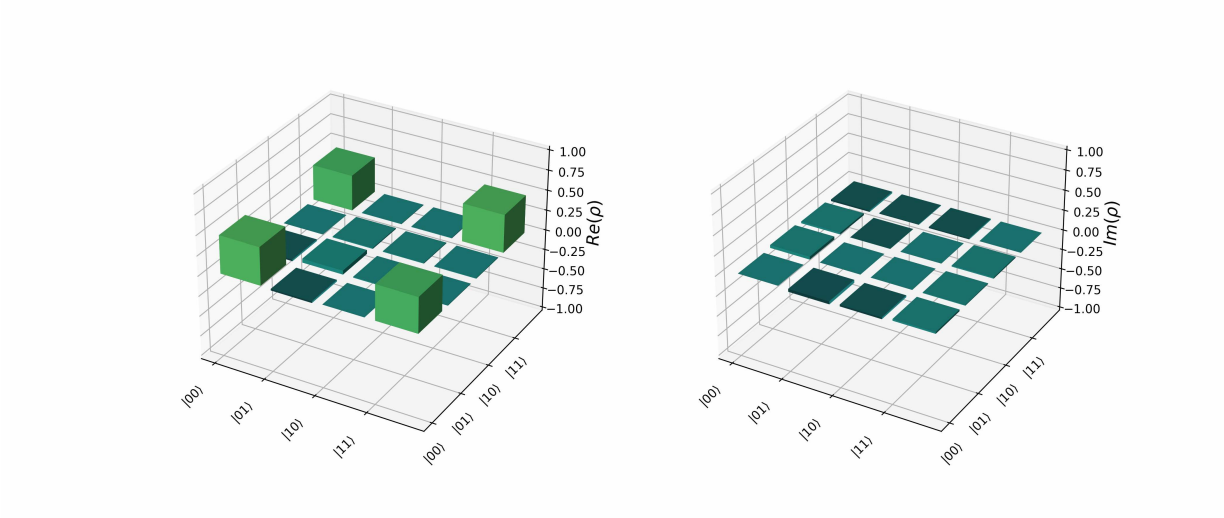


Figure 5.12: Quantum state tomography. A 91(1)% fidelity to the $|\Phi^+\rangle$ state was obtained.

Idler detector	Signal Detector	S	$\mathcal{F}(\rho, \lvert\Phi^+\rangle\langle\Phi^+\rvert)$	$\mathrm{Tr}(\rho^2)$
SNSPD	SNSPD	2.53 ± 0.03	$91 \pm 1\%$	$84 \pm 2\%$
SNSPD	InGaAs APD	2.32 ± 0.05	$85 \pm 2\%$	$78 \pm 3\%$

Table 5.3: Quantum state tomography fidelities, purities and CHSH S-parameters obtained using equatorial basis measurements performed over single-mode or multi-mode fibre. All remaining basis measurements were performed over multi-mode fibre in both configurations as depicted in Fig. 5.3d.

5.4.2 Steering inequality and entropic uncertainty relation

In the previous section, we showed that the joint-temporal intensity of our two-photon state already certifies non-classicality through the violation of the CHSH inequality. In this section, we combine the σ_Z measurement into the non-classicality certification.

The task that we consider in this section relies on all three Pauli correlations $\sigma_X \otimes \sigma_X$, $\sigma_Y \otimes \sigma_Y$ and $\sigma_Z \otimes \sigma_Z$. The test can be formulated in terms of linear steering inequalities, defined in Eqs. 5.9-5.10, and originally implemented in [261] for polarization-entangled photons.

$$\frac{1}{2}\Big(|\langle\sigma_X\sigma_X\rangle| + |\langle\sigma_Z\sigma_Z\rangle|\Big) \leq \frac{\sqrt{2}}{2}, \tag{5.9}$$

$$\frac{1}{3}\Big(|\langle\sigma_X\sigma_X\rangle| + |\langle\sigma_Y\sigma_Y\rangle| + |\langle\sigma_Z\sigma_Z\rangle|\Big) \leq \frac{\sqrt{3}}{3}. \tag{5.10}$$

This inequality allows us to verify entanglement in the presence of asymmetric trust scenarios by violating local hidden-state bounds. Steering inequalities are applicable in one-sided device-independent settings. More specifically, suppose Bob has a trusted and well-characterized measurement device. Alice's device, on the other hand, is untrusted. If the measurement correlations violate a steering inequality, it implies that Alice's reported outcomes cannot be explained by a classical model in which Bob's system is merely responding to a pre-existing local hidden state. Instead, Alice's measurements must have non-locally influenced, or *steered*, Bob's system, thereby certifying entanglement under minimal trust assumptions. The expectation values for the three bases considered in Eq. 5.9 are reported in Table 5.4. In particular, we violate the classical bound in Eq. 5.10 (Eq. 5.9) by more than 27σ (19σ) over single-mode fibre, and by more than 7σ (5σ) over multi-mode fibre. Note that there is a slight discrepancy between the expectation values $\langle\sigma_X\sigma_X\rangle$ and $\langle\sigma_Y\sigma_Y\rangle$

for the equatorial basis. This asymmetry is also apparent as a parity dependent modulation in Fig. 5.6b and we attribute it to contributions from uncorrelated pump photons which introduce a sub-harmonic oscillation at $\Delta\omega(t_s + t_i)/2$. More interestingly, the same

Idler detector	Signal Detector	$\langle\sigma_X\sigma_X\rangle$	$\langle\sigma_Y\sigma_Y\rangle$	$\langle\sigma_Z\sigma_Z\rangle$	$\frac{1}{3}\sum_{i=1}^{3}\langle\sigma_i\sigma_i\rangle$
SNSPD	SNSPD	-0.912	0.839	0.873	0.875 ± 0.011
SNSPD	InGaAs APD	-0.880	0.831	0.873	0.861 ± 0.039

Table 5.4: Steering inequality violation for the single-mode and multi-mode channels. Note that the $\langle\sigma_Z\sigma_Z\rangle$ was measured in both scenarios using the InGaAs APD detector.

quantities can be evaluated through the uncertainty relation studied in [262, 263], which allows us to reveal the non-classical nature of our biphoton state through its violation of the discrete entropic uncertainty relations. Consider the discrete observables $\sigma_X \otimes \sigma_X$, $\sigma_Y \otimes \sigma_Y$ and $\sigma_Z \otimes \sigma_Z$ measured in our experiment, the entropic uncertainty relation are of the form

$$H(\sigma_X^s \mid \sigma_X^i) + H(\sigma_Z^s \mid \sigma_Z^i) \geq 1, \tag{5.11}$$

$$H(\sigma_X^s \mid \sigma_X^i) + H(\sigma_Y^s \mid \sigma_Y^i) + H(\sigma_Z^s \mid \sigma_Z^i) \geq 2, \tag{5.12}$$

where $H(\sigma_Z^s \mid \sigma_Z^i)$ is the conditional Shannon entropy of the signal outcome given the idler outcome, which quantifies the correlation in the $\sigma_Z^s \otimes \sigma_Z^i$ measurements. More specifically, we denote the experimentally determined joint probabilities as $\{p(a_s b_i)\}_{a_s,b_i=0}^{1}$, the conditional Shannon entropy is then given as

$$H(\sigma_Z^s \mid \sigma_Z^i) = -\sum_{b_i \in \{0,1\}} p(b_i) \sum_{a_s \in \{0,1\}} p(a_s|b_i) \log_2 p(a_s|b_i) \tag{5.13}$$

where $p(b_i) = \sum_{a_s} p(a_s, b_i)$, $p(a_s|b_i) = \frac{p(a_s,b_i)}{p(b_i)}$ and $p(a_s, b_i)$ is the probability of getting outcome a_s, b_i in the correlated Pauli measurement. In our setup, the σ_Z basis corresponds to **energy** (i.e. frequency-bin) measurements, whereas the equatorial Pauli bases σ_X and σ_Y are realized via joint temporal measurements. Equations (5.11)–(5.12) are therefore a *discrete version of the time–energy uncertainty relation*: an entangled state can simultaneously render the conditional energy entropy *and* the conditional time entropy almost zero, thus violating the classical bound imposed on any local hidden state model [263, 264, 265]. Here we summarize the experimental violation of the entropic uncertainty relation in Table 5.5 where we find a violation of the classical bound in Eq. 5.12 by more than 12σ over single-mode fibre, and by more than 3σ over multi-mode fibre.

Idler detector	Signal Detector	$H(\sigma_X^s \mid \sigma_X^i)$	$H(\sigma_Y^s \mid \sigma_Y^i)$	$H(\sigma_Z^s \mid \sigma_Z^i)$	$\sum_{j=1}^{3} H(\sigma_j^s \mid \sigma_j^i)$
SNSPD	SNSPD	0.369	0.280	0.307	0.956 ± 0.082
SNSPD	InGaAs APD	0.534	0.338	0.307	1.179 ± 0.247

Table 5.5: Entropic uncertainty relation for the single-mode and multi-mode channels. Note that the $H(\sigma_Z^s \mid \sigma_Z^i)$ was measured in both scenarios using the InGaAs APD detector.

5.4.3 Quantum Key Distribution

Due to their low SWaP requirements [192], and qudit scalability, frequency-bin encoding is especially well suited for quantum communication systems in resource-constrained environments, such as satellite payloads. There is a natural extension of this time-resolved frequency-bin detection scheme to QKD, in particular in the context of RFI protocols. While the equatorial basis can be used as an entanglement witness to estimate Eve's information, the σ_Z-basis is fixed and can be used for the key-map. To demonstrate feasibility, we consider the 6-state 4-state protocol defined in [266], where the channel quality is evaluated using the following C-parameter:

$$C = \sqrt{\langle \sigma_X \sigma_X \rangle^2 + \langle \sigma_Y \sigma_X \rangle^2}, \tag{5.14}$$

where $C = 1$ indicates a maximally entangled state or perfect channel. The QBER, meanwhile, is given by

$$\mathrm{QBER}_{\mathrm{ZZ}} = \frac{1 - \langle \sigma_Z \sigma_Z \rangle}{2}. \tag{5.15}$$

Using the values calculated in Table 5.4, we have $\mathrm{QBER}_{\mathrm{ZZ}} = 6.35\%$. We can then calculate an asymptotic key rate, K according to

$$K \geq qR[1 - fH_2(\mathrm{QBER}_{ZZ}) - H_2(\mathrm{QBER}_{\mathrm{Equatorial}})], \tag{5.16}$$

where $\mathrm{QBER}_{\mathrm{Equatorial}} = \frac{1-\mathrm{C}}{2}$, q is the basis reconciliation factor, R is the coincidence detection rate, f the bidirection error correction efficiency, and $H_2(x)$ is the binary entropy function. The main figure of merit, the $C-$parameter and the secure key rate are presented in Fig. 5.13. We observe that the $C-$ parameter, which quantifies the channel integrity, exceeds the threshold required for a positive secret key rate. The number of secret bits per coincidence detection at the asymptotic limit is estimated to be 0.058(3) bits/coincidence. We emphasize that these QKD results are intended solely as a proof of concept to demonstrate feasibility; they are not representative of the achievable performance, as the data

have undergone post-processing including background subtraction as discussed in Sec. 5.3. Nevertheless, these results indicate compatibility with practical quantum communication protocols, which may not be constrained by the extrinsic limitations of this demonstration, particularly the low CAR.

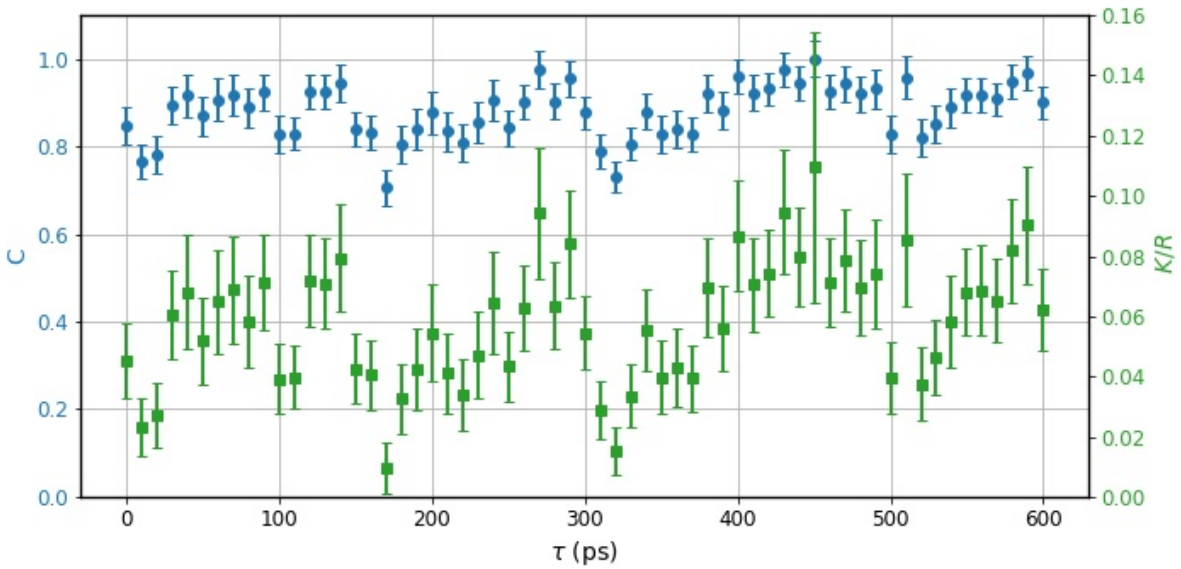


Figure 5.13: C-parameter and secure key rate calculated according to Eq. 5.14-5.16.

5.5 Summary and outlook

We conclude this chapter with a few remarks on our novel approach to measure frequency-bin encoded photons with passive linear interferometry and time-resolved detection.

1. While we have discussed in Sec. 5.4.3, a RFI protocol that leverages both the σ_Z and the equatorial bases, it is worth noting that an alternative protocol could be developed using solely the equatorial measurements as mutually unbiased bases can be defined, and a violation of the CHSH inequality can be achieved solely through post-selection based on photon arrival times. This approach eliminates the need for interferometric stability. The simplicity of this method, illustrated in Fig. 5.3c, enables a remarkably compact and robust experimental implementation, making it especially well-suited

for scenarios with constrained resources or limited infrastructure—such as satellite-based or field-deployed quantum communication.

2. The scheme can be extended to higher dimensions via additional linear interferometry [211, 267] and incorporating additional microresonator arrays [260]. By mapping the frequency bins to spatial modes and recombining them on a single-photon detector arbitrary qudit projectors can be implemented. For example, in Fig. 5.14 we present a simulation of the JTI for a qutrit projection corresponding to

$$|P_{s,i}(t_s, t_i)\rangle \propto \left(|0_s\rangle + e^{i\Delta\omega t_s}|1_s\rangle + e^{i2\Delta\omega t_s}|2_s\rangle\right) \otimes \left(|0_i\rangle + e^{i\Delta\omega t_i}|1_i\rangle + e^{i2\Delta\omega t_i}|2_i\rangle\right). \quad (5.17)$$

   Optical interleavers offer a practical and scalable approach to demultiplexing and recombining frequency bins with high extinction and low loss, enabling parallel processing of multiple frequency modes.

3. In both our time-resolved detection scheme and the standard EOM-based approach, where spectral interference between bins is induced using a fast modulator, accurate measurement of frequency-bin phase information relies on ultra-fast devices. As shown in Sec. 4.2.2, increasing timing jitter leads to dephasing in frequency-bin measurements. However, ancillary-assisted strategies could mitigate this dephasing and relax the requirement for ultra-fast devices.

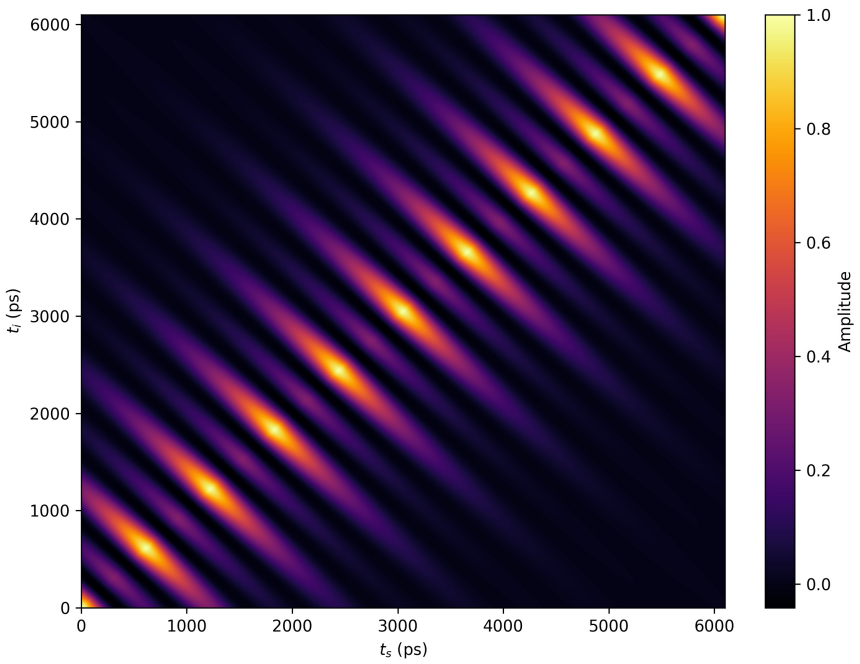


Figure 5.14: Simulated JTI for the qutrit projection defined in Eq. 5.17.

Chapter 6

Conclusions

We conclude with a summary of the thesis's results and an outlook for future research directions.

6.1 Summary of results and research outlook

This thesis demonstrates multiple advances that support the development of satellite-assisted quantum networks.

A reconfigurable architecture for satellite-assisted quantum network

In chapter 2, we outlined a vision towards a global quantum network relying on heterogeneous networks and satellite links to connect distant QMANs. Central to this vision is our reconfigurable network architecture, which efficiently integrates satellite nodes into terrestrial quantum networks while supporting continuous, around-the-clock operation. A key advantage of this architecture is its resource efficiency enabled by a combination of WDM and TDM. Not only does the architecture use the same entangled photon source for both the ground and satellite configurations, it also requires only minimal hardware at each node, including the satellite, thus reducing deployment costs and enhancing the scalability of the system. Importantly, satellites extend the quantum communication range beyond QMANs. Moreover, quantum frequency conversion could significantly extend the range of the ground configuration [268, 269]. In fact, quantum frequency conversion from 780 nm to the telecom band has already been demonstrated with a 57% conversion efficiency [270]

paving the way for entanglement distribution in optical fibre over distances of hundreds of kilometres [271].

After first demonstrating the network reconfiguration capabilities in a tabletop experiment with up to 5 nodes, in chapter 3, we proposed an integrated version of the EPS capable of supporting 72 users to further enhance the practicality of our network. Paired with reconfigurable add-drop demultiplexers and adaptive bandwidth management, the integrated source design offers dynamic and efficient photon routing beyond the two topologies outline in Fig. 3.1c-d, to subgraphs tailored to the network's real-time demands. Our architecture functions as an entanglement distribution server: it distributes entangled photon pairs between the users without requiring trust in the service provider. Network clients can independently verify the security of their communication links through correlation measurements as exemplified in Secs. 1.3.2 and 5.3.1. Although its demonstration was designed for the QEYSSat mission, the network architecture is extendable to other wavelengths. A particularly interesting case would be the use of a degenerate telecom EPS. Not only would this scenario benefit from favorable loss scaling in optical fibres, it would also maximize compatibility with the ITU grid, thereby enabling the use of cost-effective, off-the-shelf telecom components. Although telecom wavelengths also exhibit good transmission through the atmosphere [51], a key limitation for ground-to-space links remains the lack of high-efficiency, space-qualified single-photon detectors in this band. Despite recent progress [272, 273, 274], integrating SNSPDs onboard satellites remains extremely challenging due to their important power requirements, most notably from the cryogenic cooling systems.

Frequency-bin encoding

Although our proposed integrated source employs time-bin encoding, the network design is flexible and compatible with different encoding schemes, such as polarization or frequency-bin encoding. The latter is particularly promising for optical interfacing between heterogeneous network nodes [192], as bichromatic photons can interface quantum systems operating at different wavelengths [195, 210]. Furthermore, *spectral linear optical quantum computation (LOQC)* [180] offers favorable linear scaling of optical resources by decomposing any matrix transformation into a sequence of EOMs and pulse shaping operations. A key advantage of this approach is massive parallelization, as the EOM and pulse shaper can act coherently across many frequency modes, thus allowing for a $\mathcal{O}(N)$ component scaling, in contrast to the $\mathcal{O}(N^2)$ scaling for typical spatial- or polarization-encoded LOQC. Unfortunately, these methods are limited to single-spatial mode operation, thus restricting the deployment of frequency-bin quantum communication over long distances. In chapter 4,

we proposed an alternative method to process frequency-bin encoded quantum information compatible with multi-mode channels. To correct for spatial distortions and pointing errors arising from turbulent free-space links, we developed multi-mode frequency-bin analyzers based on FWIs. Leveraging linear interferometry and time-resolved detection, we demonstrated high-fidelity prepare-and-measure quantum communication and entanglement distribution. Time-resolved detection serves as a powerful technique for controlling quantum processes, enabling operations such as entanglement swapping and teleportation through heralding [252] and post-selection [29, 250]. Moreover, our approach is fully passive, easily implementable, and scalable to higher dimensions. Whilst our numerical analysis suggests frequency-bins are compatible with moving platforms including aircraft and satellites, their performance must still be validated outside of the laboratory, in more rigorous turbulent environments. To assess robustness under realistic deployment conditions, work is currently underway to test frequency-bin encoding over outdoor free-space links.

Our FWIs can be further optimized in the near future. The throughput could be significantly improved by employing optics with anti-reflection (AR) coatings and using glass rods with higher surface quality, as the current rods contributed noticeably to the optical loss. Furthermore, interferometer visibility can be improved through more precise alignment. Visibilities approaching unity were achieved in Waterloo before shipment to Pavia. The improved throughput would significantly reduce the measurement acquisition time, thus alleviating the phase stability requirements for the interferometers. Additionally, improvements to the EPS, particularly in mitigating Raman scattering in the SiN ring resonators, could boost the CAR, removing the need for background subtraction and enabling higher-fidelity measurements.

Applications in quantum computing

Both quantum frequency comb sources and our FWIs are also compatible with time-bin encoding, making them suitable platforms for exploring time-frequency entanglement and hybrid encoding schemes. Recent proposals have suggested that single-photon frequency combs, known as time-frequency Gottesman-Kitaev-Preskill (TFGKP) states, could enable universal LOQC without the use of any active devices [213]. More specifically, the proposal leverages the same passive building blocks we demonstrated in chapter 5: optical interleavers and time-resolved detectors. Furthermore, discretization in both time and frequency degrees of freedom leads to inherent error robustness against both temporal and spectral errors for the TFGKP states. Another interesting research direction for measurement-based quantum computation, is the generation of large linear cluster states.

Novel approaches have demonstrated how frequency-encoded linear cluster states can be generated with limited sensitivity to decoherence while exploiting the compatibility of frequency modes with multiplexed architectures [188].

Scaling to qudits

To exploit the wide range of benefits of frequency encoding, our time-resolved detection scheme must be extended to higher dimensions. This can be achieved through additional interferometric stages. However, careful attention to the phase stability of the photonic circuit is required as small drifts will degrade the interference visibility, leading to reduced measurement fidelity in higher-dimensional Hilbert spaces [211]. Another key consideration, especially in the context of satellite-based communication, is the form factor of the analyzer. Although the frequency-bin source has low SWaP requirements, the free-space analyzer becomes rapidly bulky for qudits. A possible solution lies in the use of Herriott cells [275] or nested interferometers [276], which allow the implementation of unbalanced interferometers with significantly reduced physical footprint, suitable for compact space-based photonic systems.

Quantum interconnects

The narrow bandwidth of frequency-bin photons could enable efficient storage and retrieval in quantum memories. Such memories are essential components of quantum networks. They significantly improve the efficiency of key network tasks such as entanglement swapping and quantum teleportation by allowing the synchronization of probabilistic processes. By temporarily storing successful quantum states, memories ensure that independently generated or received photons can be coordinated in time, supporting high-fidelity operations even when individual events occur asynchronously or with low probability. In addition, memories can alleviate network congestion by providing temporary buffering of quantum information. While several platforms have been proposed for the storage and retrieval of frequency-bin qubits [190, 192, 277, 278, 279, 280, 281], significant work remains to be done toward a first experimental demonstration. Key challenges include achieving spectral compatibility between the memory bandwidth and the frequency-bin qubit, maintaining coherence during storage, and integrating the memory with low-loss photonic interfaces.

Despite these open problems, we hope that the ideas, protocols, and applications presented in this thesis contribute a meaningful step toward the development of a global quantum network.

References

[1] Stéphane Vinet, Ramy Tannous, and Thomas Jennewein. A reconfigurable entanglement distribution network suitable for connecting multiple ground nodes with a satellite. *EPJ Quantum Technology*, 12(1):8, January 2025.

[2] Stéphane Vinet, Duncan England, Chang qing Xu, and Thomas Jennewein. Demonstration of a reconfigurable ground to space quantum networking scheme, 2025.

[3] Stéphane Vinet, Wilson Wu, Yujie Zhang, and Thomas Jennewein. Feasibility study of frequency-encoded photonic qubits over a free-space channel. *Opt. Express*, 33(19):40437–40449, Sep 2025.

[4] Stéphane Vinet, Marco Clementi, Marcello Bacchi, Yujie Zhang, Massimo Giacomin, Luke Neal, Paolo Villoresi, Matteo Galli, Daniele Bajoni, and Thomas Jennewein. Time-resolved certification of frequency-bin entanglement over multi-mode channels, 2025.

[5] O. Gayer, Z. Sacks, E. Galun, and A. Arie. Temperature and wavelength dependent refractive index equations for MgO-doped congruent and stoichiometric LiNbO3. *Applied Physics B*, 91(2):343–348, May 2008.

[6] Toptica Photonics AG. Toptica dl pro, 2024. Accessed: 2024-10-30.

[7] UQ Devices. *Logic16: Logic Analyzer Specifications Datasheet*, 2019. Accessed: Sep. 30, 2024.

[8] Teledyne LeCroy. *Operator's Manual Insert for Teledyne LeCroy Instruments*, n.d. Accessed: 2024-11-27.

[9] H. J. Kimble. The quantum internet. *Nature*, 453(7198):1023–1030, June 2008.

[10] Stephanie Wehner, David Elkouss, and Ronald Hanson. Quantum internet: A vision for the road ahead. *Science*, 362(6412):eaam9288, 2018.

[11] Ch H Bennett and G Brassard. Proceedings of the ieee international conference on computers, systems and signal processing, 1984.

[12] Artur K. Ekert. Quantum cryptography based on bell's theorem. *Phys. Rev. Lett.*, 67:661–663, Aug 1991.

[13] Anne Broadbent, Joseph Fitzsimons, and Elham Kashefi. Universal blind quantum computation. In *2009 50th Annual IEEE Symposium on Foundations of Computer Science*, pages 517–526, 2009.

[14] Naomi H. Nickerson, Joseph F. Fitzsimons, and Simon C. Benjamin. Freely scalable quantum technologies using cells of 5-to-50 qubits with very lossy and noisy photonic links. *Phys. Rev. X*, 4:041041, Dec 2014.

[15] Daniel Gottesman, Thomas Jennewein, and Sarah Croke. Longer-baseline telescopes using quantum repeaters. *Phys. Rev. Lett.*, 109:070503, Aug 2012.

[16] P. Kómár, E. M. Kessler, M. Bishof, L. Jiang, A. S. Sørensen, J. Ye, and M. D. Lukin. A quantum network of clocks. *Nature Physics*, 10(8):582–587, August 2014.

[17] Stephen Wiesner. Conjugate coding. *SIGACT News*, 15(1):78–88, January 1983.

[18] Scott Aaronson and Paul Christiano. Quantum money from hidden subspaces, 2012.

[19] Charles H. Bennett and Gilles Brassard. Quantum cryptography: Public key distribution and coin tossing. *Theoretical Computer Science*, 560:7–11, 2014. Theoretical Aspects of Quantum Cryptography : celebrating 30 years of BB84.

[20] Dik Bouwmeester, Jian-Wei Pan, Klaus Mattle, Manfred Eibl, Harald Weinfurter, and Anton Zeilinger. Experimental quantum teleportation. *Nature*, 390(6660):575–579, December 1997.

[21] I. Marcikic, H. de Riedmatten, W. Tittel, H. Zbinden, and N. Gisin. Long-distance teleportation of qubits at telecommunication wavelengths. *Nature*, 421(6922):509–513, January 2003.

[22] Thomas Jennewein, Gregor Weihs, Jian-Wei Pan, and Anton Zeilinger. Experimental nonlocality proof of quantum teleportation and entanglement swapping. *Phys. Rev. Lett.*, 88:017903, Dec 2001.

[23] Yu-Ao Chen, Shuai Chen, Zhen-Sheng Yuan, Bo Zhao, Chih-Sung Chuu, Jörg Schmiedmayer, and Jian-Wei Pan. Memory-built-in quantum teleportation with photonic and atomic qubits. *Nature Physics*, 4(2):103–107, February 2008.

[24] Thomas Jennewein, Christoph Simon, Gregor Weihs, Harald Weinfurter, and Anton Zeilinger. Quantum cryptography with entangled photons. *Phys. Rev. Lett.*, 84:4729–4732, May 2000.

[25] Xiao-Song Ma, Thomas Herbst, Thomas Scheidl, Daqing Wang, Sebastian Kropatschek, William Naylor, Bernhard Wittmann, Alexandra Mech, Johannes Kofler, Elena Anisimova, Vadim Makarov, Thomas Jennewein, Rupert Ursin, and Anton Zeilinger. Quantum teleportation over 143 kilometres using active feed-forward. *Nature*, 489(7415):269–273, September 2012.

[26] Charles H. Bennett, François Bessette, Gilles Brassard, Louis Salvail, and John Smolin. Experimental quantum cryptography. *Journal of Cryptology*, 5(1):3–28, January 1992.

[27] A. Muller, T. Herzog, B. Huttner, W. Tittel, H. Zbinden, and N. Gisin. Plug and play systems for quantum cryptography. *Applied Physics Letters*, 70(7):793–795, February 1997. _eprint: https://pubs.aip.org/aip/apl/article-pdf/70/7/793/18525022/793_1_online.pdf.

[28] Jian-Wei Pan, Dik Bouwmeester, Harald Weinfurter, and Anton Zeilinger. Experimental entanglement swapping: Entangling photons that never interacted. *Phys. Rev. Lett.*, 80:3891–3894, May 1998.

[29] Matthäus Halder, Alexios Beveratos, Nicolas Gisin, Valerio Scarani, Christoph Simon, and Hugo Zbinden. Entangling independent photons by time measurement. *Nature Physics*, 3(10):692–695, October 2007.

[30] D. Stucki, M. Legré, F. Buntschu, B. Clausen, N. Felber, N. Gisin, L. Henzen, P. Junod, G. Litzistorf, P. Monbaron, L. Monat, J.-B. Page, D. Perroud, G. Ribordy, A. Rochas, S. Robyr, J. Tavares, R. Thew, P. Trinkler, S. Ventura, R. Voirol, N. Walenta, and H. Zbinden. Long-term performance of the swissquantum quantum key distribution network in a field environment. *New Journal of Physics*, 13:123001, 2011.

[31] Chip Elliott, Alexander Colvin, David Pearson, Oleksiy Pikalo, John Schlafer, and Henry Yeh. Current status of the DARPA quantum network. In Eric J. Donkor,

Andrew R. Pirich, and Howard E. Brandt, editors, *Quantum Information and Computation III*, volume 5815, pages 138 – 149. International Society for Optics and Photonics, SPIE, 2005.

[32] V. Martin, J. P. Brito, L. Ortíz, R. B. Méndez, J. S. Buruaga, R. J. Vicente, A. Sebastián-Lombraña, D. Rincón, F. Pérez, C. Sánchez, M. Peev, H. H. Brunner, F. Fung, A. Poppe, F. Fröwis, A. J. Shields, R. I. Woodward, H. Griesser, S. Roehrich, F. de la Iglesia, C. Abellán, M. Hentschel, J. M. Rivas-Moscoso, A. Pastor-Perales, J. Folgueira, and D. López. MadQCI: a heterogeneous and scalable SDN-QKD network deployed in production facilities. *npj Quantum Information*, 10(1):80, September 2024.

[33] Yong-Hua Yang, Pei-Yuan Li, Shi-Zhao Ma, Xiao-Cong Qian, Kai-Yi Zhang, Liu-Jun Wang, Wan-Li Zhang, Fei Zhou, Shi-Biao Tang, Jia-Yong Wang, Yu Yu, Qiang Zhang, and Jian-Wei Pan. All optical metropolitan quantum key distribution network with post-quantum cryptography authentication. *Opt. Express*, 29(16):25859–25867, Aug 2021.

[34] M. Sasaki, M. Fujiwara, H. Ishizuka, W. Klaus, K. Wakui, M. Takeoka, S. Miki, T. Yamashita, Z. Wang, A. Tanaka, K. Yoshino, Y. Nambu, S. Takahashi, A. Tajima, A. Tomita, T. Domeki, T. Hasegawa, Y. Sakai, H. Kobayashi, T. Asai, K. Shimizu, T. Tokura, T. Tsurumaru, M. Matsui, T. Honjo, K. Tamaki, H. Takesue, Y. Tokura, J. F. Dynes, A. R. Dixon, A. W. Sharpe, Z. L. Yuan, A. J. Shields, S. Uchikoga, M. Legré, S. Robyr, P. Trinkler, L. Monat, J. B. Page, G. Ribordy, A. Poppe, A. Allacher, O. Maurhart, T. Länger, M. Peev, and A. Zeilinger. Field test of quantum key distribution in the Tokyo QKD Network. *Optics Express*, 19(11):10387, May 2011.

[35] Markus Aspelmeyer, Hannes R. Böhm, Tsewang Gyatso, Thomas Jennewein, Rainer Kaltenbaek, Michael Lindenthal, Gabriel Molina-Terriza, Andreas Poppe, Kevin Resch, Michael Taraba, Rupert Ursin, Philip Walther, and Anton Zeilinger. Long-distance free-space distribution of quantum entanglement. *Science*, 301(5633):621–623, 2003.

[36] Xian-Min Jin, Ji-Gang Ren, Bin Yang, Zhen-Huan Yi, Fei Zhou, Xiao-Fan Xu, Shao-Kai Wang, Dong Yang, Yuan-Feng Hu, Shuo Jiang, Tao Yang, Hao Yin, Kai Chen, Cheng-Zhi Peng, and Jian-Wei Pan. Experimental free-space quantum teleportation. *Nature Photonics*, 4(6):376–381, June 2010.

[37] Cheng-Zhi Peng, Tao Yang, Xiao-Hui Bao, Jun Zhang, Xian-Min Jin, Fa-Yong Feng, Bin Yang, Jian Yang, Juan Yin, Qiang Zhang, Nan Li, Bao-Li Tian, and Jian-Wei Pan. Experimental free-space distribution of entangled photon pairs over 13 km: Towards satellite-based global quantum communication. *Phys. Rev. Lett.*, 94:150501, Apr 2005.

[38] R. Ursin, F. Tiefenbacher, T. Schmitt-Manderbach, H. Weier, T. Scheidl, M. Lindenthal, B. Blauensteiner, T. Jennewein, J. Perdigues, P. Trojek, B. Ömer, M. Fürst, M. Meyenburg, J. Rarity, Z. Sodnik, C. Barbieri, H. Weinfurter, and A. Zeilinger. Entanglement-based quantum communication over 144 km. *Nature Physics*, 3(7):481–486, July 2007.

[39] Sheng-Kai et al Liao. Satellite-to-ground quantum key distribution. *Nature*, 549(7670):43–47, Sep 2017.

[40] Sheng-Kai Liao, Wen-Qi Cai, Johannes Handsteiner, Bo Liu, Juan Yin, Liang Zhang, Dominik Rauch, Matthias Fink, Ji-Gang Ren, Wei-Yue Liu, Yang Li, Qi Shen, Yuan Cao, Feng-Zhi Li, Jian-Feng Wang, Yong-Mei Huang, Lei Deng, Tao Xi, Lu Ma, Tai Hu, Li Li, Nai-Le Liu, Franz Koidl, Peiyuan Wang, Yu-Ao Chen, Xiang-Bin Wang, Michael Steindorfer, Georg Kirchner, Chao-Yang Lu, Rong Shu, Rupert Ursin, Thomas Scheidl, Cheng-Zhi Peng, Jian-Yu Wang, Anton Zeilinger, and Jian-Wei Pan. Satellite-relayed intercontinental quantum network. *Phys. Rev. Lett.*, 120:030501, Jan 2018.

[41] Yu-Ao Chen, Qiang Zhang, Teng-Yun Chen, Wen-Qi Cai, Sheng-Kai Liao, Jun Zhang, Kai Chen, Juan Yin, Ji-Gang Ren, Zhu Chen, Sheng-Long Han, Qing Yu, Ken Liang, Fei Zhou, Xiao Yuan, Mei-Sheng Zhao, Tian-Yin Wang, Xiao Jiang, Liang Zhang, Wei-Yue Liu, Yang Li, Qi Shen, Yuan Cao, Chao-Yang Lu, Rong Shu, Jian-Yu Wang, Li Li, Nai-Le Liu, Feihu Xu, Xiang-Bin Wang, Cheng-Zhi Peng, and Jian-Wei Pan. An integrated space-to-ground quantum communication network over 4,600 kilometres. *Nature*, 589(7841):214–219, January 2021.

[42] Juan Yin, Yuan Cao, Yu-Huai Li, Sheng-Kai Liao, Liang Zhang, Ji-Gang Ren, Wen-Qi Cai, Wei-Yue Liu, Bo Li, Hui Dai, Guang-Bing Li, Qi-Ming Lu, Yun-Hong Gong, Yu Xu, Shuang-Lin Li, Feng-Zhi Li, Ya-Yun Yin, Zi-Qing Jiang, Ming Li, Jian-Jun Jia, Ge Ren, Dong He, Yi-Lin Zhou, Xiao-Xiang Zhang, Na Wang, Xiang Chang, Zhen-Cai Zhu, Nai-Le Liu, Yu-Ao Chen, Chao-Yang Lu, Rong Shu, Cheng-Zhi Peng, Jian-Yu Wang, and Jian-Wei Pan. Satellite-based entanglement distribution over 1200 kilometers. *Science*, 356(6343):1140–1144, 2017.

[43] Ji-Gang Ren, Ping Xu, Hai-Lin Yong, Liang Zhang, Sheng-Kai Liao, Juan Yin, Wei-Yue Liu, Wen-Qi Cai, Meng Yang, Li Li, Kui-Xing Yang, Xuan Han, Yong-Qiang Yao, Ji Li, Hai-Yan Wu, Song Wan, Lei Liu, Ding-Quan Liu, Yao-Wu Kuang, Zhi-Ping He, Peng Shang, Cheng Guo, Ru-Hua Zheng, Kai Tian, Zhen-Cai Zhu, Nai-Le Liu, Chao-Yang Lu, Rong Shu, Yu-Ao Chen, Cheng-Zhi Peng, Jian-Yu Wang, and Jian-Wei Pan. Ground-to-satellite quantum teleportation. *Nature*, 549(7670):70–73, September 2017.

[44] Eleni Diamanti, Hoi-Kwong Lo, Bing Qi, and Zhiliang Yuan. Practical challenges in quantum key distribution. *npj Quantum Information*, 2(1):16025, November 2016.

[45] Peter P. Rohde, Zixin Huang, Yingkai Ouyang, He-Liang Huang, Zu-En Su, Simon Devitt, Rohit Ramakrishnan, Atul Mantri, Si-Hui Tan, Nana Liu, Scott Harrison, Chandrashekar Radhakrishnan, Gavin K. Brennen, Ben Q. Baragiola, Jonathan P. Dowling, Tim Byrnes, and William J. Munro. The quantum internet (technical version), 2025.

[46] W. K. Wootters and W. H. Zurek. A single quantum cannot be cloned. *Nature*, 299(5886):802–803, October 1982.

[47] Corning® smf-28® ultra optical fiber. Technical Report PI-1424-AEN, Corning Incorporated, February 2024. Product Information Sheet.

[48] Siddarth Koduru Joshi, Djeylan Aktas, Sören Wengerowsky, Martin Lončarić, Sebastian Philipp Neumann, Bo Liu, Thomas Scheidl, Guillermo Currás Lorenzo, Željko Samec, Laurent Kling, Alex Qiu, Mohsen Razavi, Mario Stipčević, John G. Rarity, and Rupert Ursin. A trusted node-free eight-user metropolitan quantum communication network. *Science Advances*, 6(36):eaba0959, 2020.

[49] Sören Wengerowsky, Siddarth Koduru Joshi, Fabian Steinlechner, Hannes Hübel, and Rupert Ursin. An entanglement-based wavelength-multiplexed quantum communication network. *Nature*, 564(7735):225–228, December 2018.

[50] M. Peev, C. Pacher, R. Alléaume, C. Barreiro, J. Bouda, W. Boxleitner, T. Debuisschert, E. Diamanti, M. Dianati, J. F. Dynes, S. Fasel, S. Fossier, M. Fürst, J. D. Gautier, O. Gay, N. Gisin, P. Grangier, A. Happe, Y. Hasani, M. Hentschel, H. Hübel, G. Humer, T. Länger, M. Legré, R. Lieger, J. Lodewyck, T. Lorünser, N. Lütkenhaus, A. Marhold, T. Matyus, O. Maurhart, L. Monat, S. Nauerth, J. B. Page, A. Poppe, E. Querasser, G. Ribordy, S. Robyr, L. Salvail, A. W. Sharpe, A. J. Shields, D. Stucki, M. Suda, C. Tamas, T. Themel, R. T. Thew, Y. Thoma,

A. Treiber, P. Trinkler, R. Tualle-Brouri, F. Vannel, N. Walenta, H. Weier, H. Weinfurter, I. Wimberger, Z. L. Yuan, H. Zbinden, and A. Zeilinger. The SECOQC quantum key distribution network in Vienna. *New Journal of Physics*, 11(7):075001, July 2009.

[51] J-P Bourgoin, E Meyer-Scott, B L Higgins, B Helou, C Erven, H HÃŒbel, B Kumar, D Hudson, I D'Souza, R Girard, R Laflamme, and T Jennewein. A comprehensive design and performance analysis of low earth orbit satellite quantum communication. *New Journal of Physics*, 15(2):023006, feb 2013.

[52] Riccardo Bassoli, Holger Boche, Christian Deppe, Roberto Ferrara, Frank H. P. Fitzek, Gisbert Janssen, and Sajad Saeedinaeeni. Introduction. In *Quantum Communication Networks*, pages 1–11. Springer International Publishing, Cham, 2021.

[53] Yang Li, Wen-Qi Cai, Ji-Gang Ren, Chao-Ze Wang, Meng Yang, Liang Zhang, Hui-Ying Wu, Liang Chang, Jin-Cai Wu, Biao Jin, Hua-Jian Xue, Xue-Jiao Li, Hui Liu, Guang-Wen Yu, Xue-Ying Tao, Ting Chen, Chong-Fei Liu, Wen-Bin Luo, Jie Zhou, Hai-Lin Yong, Yu-Huai Li, Feng-Zhi Li, Cong Jiang, Hao-Ze Chen, Chao Wu, Xin-Hai Tong, Si-Jiang Xie, Fei Zhou, Wei-Yue Liu, Yaseera Ismail, Francesco Petruccione, Nai-Le Liu, Li Li, Feihu Xu, Yuan Cao, Juan Yin, Rong Shu, Xiang-Bin Wang, Qiang Zhang, Jian-Yu Wang, Sheng-Kai Liao, Cheng-Zhi Peng, and Jian-Wei Pan. Microsatellite-based real-time quantum key distribution. *Nature*, 640(8057):47–54, April 2025.

[54] Hideki Takenaka, Alberto Carrasco-Casado, Mikio Fujiwara, Mitsuo Kitamura, Masahide Sasaki, and Morio Toyoshima. Satellite-to-ground quantum-limited communication using a 50-kg-class microsatellite. *Nature Photonics*, 11(8):502–508, August 2017.

[55] Zhongkan Tang, Rakhitha Chandrasekara, Yue Chuan Tan, Cliff Cheng, Luo Sha, Goh Cher Hiang, Daniel K. L. Oi, and Alexander Ling. Generation and analysis of correlated pairs of photons aboard a nanosatellite. *Phys. Rev. Appl.*, 5:054022, May 2016.

[56] T. Jennewein, J. P. Bourgoin, B. Higgins, C. Holloway, E. Meyer-Scott, C. Erven, B. Heim, Z. Yan, H. Hübel, G. Weihs, E. Choi, I. D'Souza, D. Hudson, and R. Laflamme. QEYSSAT: a mission proposal for a quantum receiver in space. In Zameer U. Hasan, Philip R. Hemmer, Hwang Lee, and Charles M. Santori, editors, *Advances in Photonics of Quantum Computing, Memory, and Communication VII*,

volume 8997, page 89970A, Bellingham, WA, 2014. International Society for Optics and Photonics, SPIE.

[57] Roland Haber, Daniel Garbe, Klaus Schilling, and Wenjamin Rosenfeld. Qube-a cubesat for quantum key distribution experiments. 2018.

[58] Sebastian Philipp Neumann, Siddarth Koduru Joshi, Matthias Fink, Thomas Scheidl, Roland Blach, Carsten Scharlemann, Sameh Abouagaga, Daanish Bambery, Erik Kerstel, Mathieu Barthelemy, et al. Q3sat: quantum communications uplink to a 3u cubesat—feasibility & design. *EPJ Quantum Technology*, 5(1):1–24, 2018.

[59] Erik Kerstel, Arnaud Gardelein, Mathieu Barthelemy, Matthias Fink, Siddarth Koduru Joshi, and Rupert Ursin. Nanobob: a cubesat mission concept for quantum communication experiments in an uplink configuration. *EPJ Quantum Technology*, 5(1):6, 2018.

[60] Sumeet Khatri, Anthony J. Brady, RenÃ©e A. Desporte, Manon P. Bart, and Jonathan P. Dowling. Spooky action at a global distance: analysis of space-based entanglement distribution for the quantum internet. *npj Quantum Information*, 7(1):4, January 2021.

[61] Luca Mazzarella, Christopher Lowe, David Lowndes, Siddarth Koduru Joshi, Steve Greenland, Doug McNeil, Cassandra Mercury, Malcolm Macdonald, John Rarity, and Daniel Kuan Li Oi. Quarc: Quantum research cubesat - constellation for quantum communication. *Cryptography*, 4(1), 2020.

[62] Sheng-Kai Liao, Hai-Lin Yong, Chang Liu, Guo-Liang Shentu, Dong-Dong Li, Jin Lin, Hui Dai, Shuang-Qiang Zhao, Bo Li, Jian-Yu Guan, Wei Chen, Yun-Hong Gong, Yang Li, Ze-Hong Lin, Ge-Sheng Pan, Jason S. Pelc, M. M. Fejer, Wen-Zhuo Zhang, Wei-Yue Liu, Juan Yin, Ji-Gang Ren, Xiang-Bin Wang, Qiang Zhang, Cheng-Zhi Peng, and Jian-Wei Pan. Long-distance free-space quantum key distribution in daylight towards inter-satellite communication. *Nature Photonics*, 11(8):509–513, August 2017.

[63] Zheng-Da Li, Rui Zhang, Xu-Fei Yin, Li-Zheng Liu, Yi Hu, Yu-Qiang Fang, Yue-Yang Fei, Xiao Jiang, Jun Zhang, Li Li, Nai-Le Liu, Feihu Xu, Yu-Ao Chen, and Jian-Wei Pan. Experimental quantum repeater without quantum memory. *Nature Photonics*, 13(9):644–648, June 2019.

[64] Yun-Fei Pu, Sheng Zhang, Yu-Kai Wu, Nan Jiang, Wei Chang, Chang Li, and Lu-Ming Duan. Experimental demonstration of memory-enhanced scaling for entanglement connection of quantum repeater segments. *Nature Photonics*, 15(5):374–378, January 2021.

[65] S. Langenfeld, P. Thomas, O. Morin, and G. Rempe. Quantum repeater node demonstrating unconditionally secure key distribution. *Phys. Rev. Lett.*, 126:230506, Jun 2021.

[66] T.-Y. Chen, X. Jiang, S.-B. Tang, L. Zhou, X. Yuan, H. Zhou, J. Wang, Y. Liu, L.-K. Chen, W.-Y. Liu, H.-F. Zhang, K. Cui, H. Liang, X.-G. Li, Y. Mao, L.-J. Wang, S.-B. Feng, Q. Chen, Q. Zhang, L. Li, N.-L. Liu, C.-Z. Peng, X. Ma, Y. Zhao, and J.-W. Pan. Implementation of a 46-node quantum metropolitan area network. *npj Quantum Information*, 7:134, 2021.

[67] Andrej Kržič, Sakshi Sharma, Christopher Spiess, Uday Chandrashekara, Sebastian Töpfer, Gregor Sauer, Luis Javier González-Martín del Campo, Teresa Kopf, Stefan Petscharnig, Thomas Grafenauer, Roland Lieger, Bernhard Ömer, Christoph Pacher, René Berlich, Thomas Peschel, Christoph Damm, Stefan Risse, Matthias Goy, Daniel Rieländer, Andreas Tünnermann, and Fabian Steinlechner. Towards metropolitan free-space quantum networks. *npj Quantum Information*, 9(1):95, September 2023.

[68] H. Podmore, I. D'Souza, J. Cain, T. Jennewein, B. L. Higgins, Y. S. Lee, A. Koujelev, D. Hudson, and A. McColgan. QKD terminal for Canada's Quantum Encryption and Science Satellite (QEYSSat). In Bruno Cugny, Zoran Sodnik, and Nikos Karafolas, editors, *International Conference on Space Optics ICSO 2020*, volume 11852, page 118520H. International Society for Optics and Photonics, SPIE, 2021.

[69] E. Brambila, R. Gómez, R. Fazili, M. Gräfe, and F. Steinlechner. Ultrabright polarization-entangled photon pair source for frequency-multiplexed quantum communication in free-space. *Opt. Express*, 31(10):16107–16117, 2023.

[70] Ramy Tannous. *Advancing the Robustness of Polarization and Time Bin Quantum Key Distribution for Free-Space Channels.* Phd thesis, University of Waterloo, 2023. https://uwspace.uwaterloo.ca/items/37a657db-da54-4c46-b376-764a8b996ca7.

[71] A. Scott, T. Jennewein, J. Cain, I. D'Souza, B. Higgins, D. Hudson, H. Podmore, and W. Soh. The QEYSSAT mission: on-orbit demonstration of secure optical communications network technologies. In Karin Stein and Szymon Gladysz, editors,

Environmental Effects on Light Propagation and Adaptive Systems III, volume 11532, page 115320H. International Society for Optics and Photonics, SPIE, 2020.

[72] J. P. Gordon and H. Kogelnik. Pmd fundamentals: Polarization mode dispersion in optical fibers. *Proceedings of the National Academy of Sciences*, 97(9):4541–4550, 2000.

[73] B.L. Heffner. Automated measurement of polarization mode dispersion using jones matrix eigenanalysis. *IEEE Photonics Technology Letters*, 4(9):1066–1069, 1992.

[74] Yang Liu, Teng-Yun Chen, Jian Wang, Wen-Qi Cai, Xu Wan, Luo-Kan Chen, Jin-Hong Wang, Shu-Bin Liu, Hao Liang, Lin Yang, Cheng-Zhi Peng, Kai Chen, Zeng-Bing Chen, and Jian-Wei Pan. Decoy-state quantum key distribution with polarized photons over 200 km. *Opt. Express*, 18(8):8587–8594, Apr 2010.

[75] R. T. Thew, S. Tanzilli, W. Tittel, H. Zbinden, and N. Gisin. Experimental investigation of the robustness of partially entangled qubits over 11 km. *Phys. Rev. A*, 66:062304, Dec 2002.

[76] J. Brendel, N. Gisin, W. Tittel, and H. Zbinden. Pulsed energy-time entangled twin-photon source for quantum communication. *Phys. Rev. Lett.*, 82:2594–2597, Mar 1999.

[77] Yuan Lee, Wenhan Dai, Don Towsley, and Dirk Englund. Quantum network utility: A framework for benchmarking quantum networks. *Proceedings of the National Academy of Sciences*, 121(17):e2314103121, 2024.

[78] P. Kómár, E. M. Kessler, M. Bishof, L. Jiang, A. S. Sørensen, J. Ye, and M. D. Lukin. A quantum network of clocks. *Nature Physics*, 10(8):582–587, August 2014.

[79] Uman Khalid, Junaid Ur Rehman, Saw Nang Paing, Haejoon Jung, Trung Q. Duong, and Hyundong Shin. Quantum network engineering in the nisq age: Principles, missions, and challenges. *IEEE Network*, 38(1):112–123, 2024.

[80] Nikolai Lauk, Neil Sinclair, Shabir Barzanjeh, Jacob P Covey, Mark Saffman, Maria Spiropulu, and Christoph Simon. Perspectives on quantum transduction. *Quantum Science and Technology*, 5(2):020501, March 2020. Publisher: IOP Publishing.

[81] Shi-Hai Wei et al. Towards Real-World Quantum Networks: A Review. *Laser Photonics Rev.*, 16(3):2100219, 2022.

[82] Renato Renner. Security of quantum key distribution, 2006.

[83] Bing Qi, Chi-Hang Fred Fung, Hoi-Kwong Lo, and Xiongfeng Ma. Time-shift attack in practical quantum cryptosystems, 2006.

[84] Chi-Hang Fred Fung, Bing Qi, Kiyoshi Tamaki, and Hoi-Kwong Lo. Phase-remapping attack in practical quantum-key-distribution systems. *Phys. Rev. A*, 75:032314, Mar 2007.

[85] Ilja Gerhardt, Qin Liu, Antía Lamas-Linares, Johannes Skaar, Christian Kurtsiefer, and Vadim Makarov. Full-field implementation of a perfect eavesdropper on a quantum cryptography system. *Nature Communications*, 2(1):349, June 2011.

[86] Lars Lydersen, Carlos Wiechers, Christoffer Wittmann, Dominique Elser, Johannes Skaar, and Vadim Makarov. Hacking commercial quantum cryptography systems by tailored bright illumination. *Nature Photonics*, 4(10):686–689, October 2010.

[87] Peter W. Shor. Polynomial-Time Algorithms for Prime Factorization and Discrete Logarithms on a Quantum Computer. *SIAM Journal on Computing*, 26(5):1484–1509, 1997. _eprint: https://doi.org/10.1137/S0097539795293172.

[88] Yingbin Liang, H. Vincent Poor, and Shlomo Shamai (Shitz). Information theoretic security. *Foundations and Trends® in Communications and Information Theory*, 5(4-5):355–580, 2009.

[89] Ramona Wolf. Introduction. In *Quantum Key Distribution: An Introduction with Exercises*, pages 1–12. Springer International Publishing, Cham, 2021.

[90] Marco Lucamarini, Andrew Shields, Romain Alléaume, Christopher Chunnilall, Ivo Pietro Degiovanni, Marco Gramegna, Atilla Hasekioglu, Bruno Huttner, Rupesh Kumar, Andrew Lord, Norbert Lütkenhaus, Vadim Makarov, Vicente Martin, Alan Mink, Momtchil Peev, Masahide Sasaki, Alastair Sinclair, Tim Spiller, Martin Ward, Catherine White, and Zhiliang Yuan. Implementation security of quantum cryptography: Introduction, challenges, solutions, July 2018. First edition.

[91] Gilles Brassard, Norbert Lütkenhaus, Tal Mor, and Barry C. Sanders. Security aspects of practical quantum cryptography. In *Advances in Cryptology — EUROCRYPT 2000*, volume 1807 of *Lecture Notes in Computer Science*, pages 75–89. Springer, 2000.

[92] Charles H. Bennett, Gilles Brassard, and N. David Mermin. Quantum cryptography without Bell's theorem. *Phys. Rev. Lett.*, 68:557–559, Feb 1992.

[93] Marcos Curty, Maciej Lewenstein, and Norbert Lütkenhaus. Entanglement as a precondition for secure quantum key distribution. *Phys. Rev. Lett.*, 92:217903, May 2004.

[94] Stephanie Wehner. Quantum cryptography: Week 5 lecture notes, 2016. TU Delft OpenCourseWare.

[95] Norbert Lütkenhaus and Mika Jahma. Quantum key distribution with realistic states: photon-number statistics in the photon-number splitting attack. *New Journal of Physics*, 4(1):44, July 2002.

[96] Nitin Jain, Elena Anisimova, Imran Khan, Vadim Makarov, Christoph Marquardt, and Gerd Leuchs. Trojan-horse attacks threaten the security of practical quantum cryptography. *New Journal of Physics*, 16(12):123030, December 2014. Publisher: IOP Publishing.

[97] Mu-Sheng Jiang, Shi-Hai Sun, Chun-Yan Li, and Lin-Mei Liang. Wavelength-selected photon-number-splitting attack against plug-and-play quantum key distribution systems with decoy states. *Phys. Rev. A*, 86:032310, Sep 2012.

[98] Sebastian Nauerth, Martin Fürst, Tobias Schmitt-Manderbach, Henning Weier, and Harald Weinfurter. Information leakage via side channels in freespace BB84 quantum cryptography. *New Journal of Physics*, 11(6):065001, June 2009.

[99] Hoi-Kwong Lo, Xiongfeng Ma, and Kai Chen. Decoy state quantum key distribution. *Phys. Rev. Lett.*, 94:230504, Jun 2005.

[100] M. Lucamarini, K. A. Patel, J. F. Dynes, B. Fröhlich, A. W. Sharpe, A. R. Dixon, Z. L. Yuan, R. V. Penty, and A. J. Shields. Efficient decoy-state quantum key distribution with quantified security. *Opt. Express*, 21(21):24550–24565, Oct 2013.

[101] Shlok Nahar, Twesh Upadhyaya, and Norbert Lütkenhaus. Imperfect phase randomization and generalized decoy-state quantum key distribution. *Phys. Rev. Appl.*, 20:064031, Dec 2023.

[102] John F. Clauser, Michael A. Horne, Abner Shimony, and Richard A. Holt. Proposed experiment to test local hidden-variable theories. *Phys. Rev. Lett.*, 23:880–884, Oct 1969.

[103] Ramona Wolf. Quantum Key Distribution Protocols. In *Quantum Key Distribution: An Introduction with Exercises*, pages 91–116. Springer International Publishing, Cham, 2021.

[104] J. S. Bell. On the einstein podolsky rosen paradox. *Physics Physique Fizika*, 1:195–200, Nov 1964.

[105] Richard Cleve. Quantum information theory. https://cleve.iqc.uwaterloo.ca/resources/QIC-710-F24/Qic710QuantumInformationTheory2024V3.pdf, November 2024. Lecture notes for QIC 710: Quantum Information Processing, University of Waterloo.

[106] Ramy Tannous, Wilson Wu, Stéphane Vinet, Chithrabhanu Perumangatt, Dogan Sinar, Alexander Ling, and Thomas Jennewein. Towards fully passive time-bin quantum key distribution over multi-mode channels, 2023.

[107] Stéphane Vinet, Wilson Wu, Yujie Zhang, and Thomas Jennewein. Feasibility study of frequency-encoded photonic qubits over a free-space channel, 2024.

[108] FangXing Xu, Wei Chen, Shuang Wang, ZhenQiang Yin, Yang Zhang, Yun Liu, Zheng Zhou, YiBo Zhao, HongWei Li, Dong Liu, ZhengFu Han, and GuangCan Guo. Field experiment on a robust hierarchical metropolitan quantum cryptography network. *Chinese Science Bulletin*, 54(17):2991–2997, September 2009.

[109] P. Toliver, R. J. Runser, T. E. Chapuran, J. L. Jackel, T. C. Banwell, M. S. Goodman, R. J. Hughes, C. G. Peterson, D. Derkacs, J. E. Nordholt, L. Mercer, S. McNown, A. Goldman, and J. Blake. Experimental investigation of quantum key distribution through transparent optical switch elements. *IEEE Photonics Technology Letters*, 15(11):1669–1671, November 2003.

[110] Xiao Tang, Lijun Ma, Alan Mink, Anastase Nakassis, Hai Xu, Barry Hershman, Joshua Bienfang, David Su, Ronald F. Boisvert, Charles Clark, and Carl Williams. Demonstration of an active quantum key distribution network. In Ronald E. Meyers, Yanhua Shih, and Keith S. Deacon, editors, *Quantum Communications and Quantum Imaging IV*, volume 6305, page 630506. International Society for Optics and Photonics, SPIE, 2006.

[111] Teng-Yun Chen, Jian Wang, Hao Liang, Wei-Yue Liu, Yang Liu, Xiao Jiang, Yuan Wang, Xu Wan, Wen-Qi Cai, Lei Ju, Luo-Kan Chen, Liu-Jun Wang, Yuan Gao, Kai Chen, Cheng-Zhi Peng, Zeng-Bing Chen, and Jian-Wei Pan. Metropolitan all-pass

and inter-city quantum communication network. *Opt. Express*, 18(26):27217–27225, Dec 2010.

[112] Yu-Ao Chen, Qiang Zhang, Teng-Yun Chen, Wen-Qi Cai, Sheng-Kai Liao, Jun Zhang, Kai Chen, Juan Yin, Ji-Gang Ren, Zhu Chen, Sheng-Long Han, Qing Yu, Ken Liang, Fei Zhou, Xiao Yuan, Mei-Sheng Zhao, Tian-Yin Wang, Xiao Jiang, Liang Zhang, Wei-Yue Liu, Yang Li, Qi Shen, Yuan Cao, Chao-Yang Lu, Rong Shu, Jian-Yu Wang, Li Li, Nai-Le Liu, Feihu Xu, Xiang-Bin Wang, Cheng-Zhi Peng, and Jian-Wei Pan. An integrated space-to-ground quantum communication network over 4,600 kilometres. *Nature*, 589(7841):214–219, January 2021.

[113] Päivi Törmä and Klaus M. Gheri. Establishing multi-party entanglement with entangled photons. In *Mysteries, puzzles, and paradoxes in Quantum Mechanics*, volume 461 of *American Institute of Physics Conference Series*, pages 220–228, March 1999.

[114] Djeylan Aktas, Bruno Fedrici, Florian Kaiser, Tommaso Lunghi, Laurent Labonté, and Sébastien Tanzilli. Entanglement distribution over 150 km in wavelength division multiplexed channels for quantum cryptography. *Laser & Photonics Reviews*, 10(3):451–457, May 2016.

[115] Han Chuen Lim, Akio Yoshizawa, Hidemi Tsuchida, and Kazuro Kikuchi. Broadband source of telecom-band polarization-entangled photon-pairs for wavelength-multiplexed entanglement distribution. *Optics Express*, 16(20):16052, September 2008.

[116] Johannes Pseiner, Lukas Achatz, Lukas Bulla, Martin Bohmann, and Rupert Ursin. Experimental wavelength-multiplexed entanglement-based quantum cryptography. *Quantum Science and Technology*, 6(3):035013, jun 2021.

[117] Sebastian Ecker, Johannes Pseiner, Jorge Piris, and Martin Bohmann. Advances in entanglement-based QKD for space applications. In Kyriaki Minoglou, Nikos Karafolas, and Bruno Cugny, editors, *International Conference on Space Optics - ICSO 2022*, volume 12777, page 1277727. International Society for Optics and Photonics, SPIE, 2023.

[118] Rodney Van Meter. *Resource Management and Multiplexing*, chapter 13, pages 253–264. John Wiley & Sons, Ltd, 2014.

[119] Zhantong Qi, Yuanhua Li, Yiwen Huang, Juan Feng, Yuanlin Zheng, and Xianfeng Chen. A 15-user quantum secure direct communication network. *Light: Science & Applications*, 10(1):183, September 2021.

[120] Xu Liu, Jingyuan Liu, Rong Xue, Heqing Wang, Hao Li, Xue Feng, Fang Liu, Kaiyu Cui, Zhen Wang, Lixing You, Yidong Huang, and Wei Zhang. 40-user fully connected entanglement-based quantum key distribution network without trusted node. *PhotoniX*, 3(1):2, January 2022.

[121] Dongning Liu, Jingyuan Liu, Xiaosong Ren, Xue Feng, Fang Liu, Kaiyu Cui, Yidong Huang, and Wei Zhang. Photonic-reconfigurable entanglement distribution network based on silicon quantum photonics. *Photon. Res.*, 11(7):1314–1325, Jul 2023.

[122] Alex O. C. Davis, Paul M. Saulnier, Michał Karpiński, and Brian J. Smith. Pulsed single-photon spectrometer by frequency-to-time mapping using chirped fiber bragg gratings. *Opt. Express*, 25(11):12804–12811, May 2017.

[123] Meng Lei, Weiwen Zou, Xing Li, and Jianping Chen. Ultrafast fbg interrogator based on time-stretch method. *IEEE Photonics Technology Letters*, 28(7):778–781, 2016.

[124] Michal Karpiński, Alex O. C. Davis, Filip Sośnicki, Valérian Thiel, and Brian J. Smith. Control and measurement of quantum light pulses for quantum information science and technology. *Advanced Quantum Technologies*, 4(9):2000150, 2021.

[125] Ye Yang, Xiao Xiang, Feiyan Hou, Runai Quan, Baihong Li, Wei Li, Ninghua Zhu, Tao Liu, Shougang Zhang, Ruifang Dong, and Ming Li. Inherent resolution limit on nonlocal wavelength-to-time mapping with entangled photon pairs. *Opt. Express*, 28(5):7488–7497, Mar 2020.

[126] A. Gulinatti, P. Maccagnani, I. Rech, M. Ghioni, and S. Cova. 35 ps time resolution at room temperature with large area single photon avalanche diodes. *Electronics Letters*, 41:272–274(2), March 2005.

[127] Marek Gersbach, Justin Richardson, Eric Mazaleyrat, Stephane Hardillier, Cristiano Niclass, Robert Henderson, Lindsay Grant, and Edoardo Charbon. A low-noise single-photon detector implemented in a 130nm cmos imaging process. *Solid-State Electronics*, 53(7):803–808, 2009. Papers Selected from the 38th European Solid-State Device Research Conference -ESSDERC'08.

[128] Lucio Pancheri and David Stoppa. Low-noise single photon avalanche diodes in 0.15 um cmos technology. In *2011 Proceedings of the European Solid-State Device Research Conference (ESSDERC)*, pages 179–182, 2011.

[129] Cristiano Niclass, Marek Gersbach, Robert Henderson, Lindsay Grant, and Edoardo Charbon. A single photon avalanche diode implemented in 130-nm cmos technology. *IEEE Journal of Selected Topics in Quantum Electronics*, 13(4):863–869, 2007.

[130] G. Shaw, S. Sridharan, S. Ranu, F. Shingala, P. Mandayam, and A. Prabhakar. Time-bin superposition methods for dps-qkd. *IEEE Photonics Journal*, 14(5):1–7, 2022.

[131] J. Azana and M.A. Muriel. Real-time optical spectrum analysis based on the time-space duality in chirped fiber gratings. *IEEE Journal of Quantum Electronics*, 36(5):517–526, 2000.

[132] F. Ouellette, J.-F. Cliche, and S. Gagnon. All-fiber devices for chromatic dispersion compensation based on chirped distributed resonant coupling. *Journal of Lightwave Technology*, 12(10):1728–1738, 1994.

[133] Xiongfeng Ma, Chi-Hang Fred Fung, and Hoi-Kwong Lo. Quantum key distribution with entangled photon sources. *Phys. Rev. A*, 76:012307, Jul 2007.

[134] Catherine Holloway, John A. Doucette, Christopher Erven, Jean-Philippe Bourgoin, and Thomas Jennewein. Optimal pair-generation rate for entanglement-based quantum key distribution. *Phys. Rev. A*, 87:022342, Feb 2013.

[135] Marco Barbieri Thomas Jennewein and Andrew G. White. Single-photon device requirements for operating linear optics quantum computing outside the post-selection basis. *Journal of Modern Optics*, 58(3-4):276–287, 2011.

[136] Norbert Lütkenhaus. Estimates for practical quantum cryptography. *Phys. Rev. A*, 59:3301–3319, May 1999.

[137] Tobias Moroder, Otfried Gühne, Normand Beaudry, Marco Piani, and Norbert Lütkenhaus. Entanglement verification with realistic measurement devices via squashing operations. *Phys. Rev. A*, 81:052342, May 2010.

[138] Jie Lin. Security proofs for quantum key distribution protocols by numerical approaches. Master's thesis, University of Waterloo, 2017.

[139] Shlok Nahar, Devashish Tupkary, and Norbert Lütkenhaus. Imperfect detectors for adversarial tasks with applications to quantum key distribution, 2025.

[140] Normand J. Beaudry, Tobias Moroder, and Norbert Lütkenhaus. Squashing models for optical measurements in quantum communication. *Phys. Rev. Lett.*, 101:093601, Aug 2008.

[141] Nicky Kai Hong Li. Application of the flag-state squashing model to numerical quantum key distribution security analysis. Master's thesis, University of Waterloo, Waterloo, Ontario, Canada, 2020. In fulfilment of the thesis requirement for the degree of Master of Science in Physics (Quantum Information).

[142] Pieter Kok and Brendon W. Lovett. *Introduction to Optical Quantum Information Processing*. Cambridge University Press, 2010.

[143] Christopher J. Pugh, Sarah Kaiser, Jean-Philippe Bourgoin, Jeongwan Jin, Nigar Sultana, Sascha Agne, Elena Anisimova, Vadim Makarov, Eric Choi, Brendon L. Higgins, and Thomas Jennewein. Airborne demonstration of a quantum key distribution receiver payload. *Quantum Science and Technology*, 2(2):024009, June 2017. Publisher: IOP Publishing.

[144] Single-photon generation and detection. In Alan Migdall, Sergey V. Polyakov, Jingyun Fan, and Joshua C. Bienfang, editors, *Single-Photon Generation and Detection*, volume 45 of *Experimental Methods in the Physical Sciences*, page iii. Academic Press, 2013.

[145] M. D. Eisaman, J. Fan, A. Migdall, and S. V. Polyakov. Invited Review Article: Single-photon sources and detectors. *Review of Scientific Instruments*, 82(7):071101, July 2011.

[146] Fabio Severini, Iris Cusini, Davide Berretta, Klaus Pasquinelli, Alfonso Incoronato, and Federica Villa. Spad pixel with sub-ns dead-time for high-count rate applications. *IEEE Journal of Selected Topics in Quantum Electronics*, 28(2: Optical Detectors):1–8, 2022.

[147] Id120 visible single-photon detector. Accessed: 2023-12-01.

[148] E. Meyer-Scott, H. Hübel, A. Fedrizzi, C. Erven, G. Weihs, and T. Jennewein. Quantum entanglement distribution with 810 nm photons through telecom fibers. *Applied Physics Letters*, 97(3):031117, 07 2010.

[149] M.G. Raymer and K. Srinivasan. Manipulating the color and shape of single photons. *Physics Today*, 65(11):32–37, 2012.

[150] A. Gulinatti, P. Maccagnani, I. Rech, M. Ghioni, and S. Cova. 35 ps time resolution at room temperature with large area single photon avalanche diodes. *Electronics Letters*, 41(5):272–274(2), March 2005. Publisher: Institution of Engineering and Technology.

[151] A. Khodadad Kashi and M. Kues. Frequency-bin-encoded entanglement-based quantum key distribution in a reconfigurable frequency-multiplexed network. *Light Sci. Appl.*, 14(1):49, 2025.

[152] P.S. Kuo, V.B. Verma, and S.W. Nam. Demonstration of a polarization-entangled photon-pair source based on phase-modulated ppln. *OSA Continuum*, 3(2):295–304, 2020.

[153] Martin A. Wolff, Fabian Beutel, Jonas Schütte, Helge Gehring, Matthias Häußler, Wolfram Pernice, and Carsten Schuck. Broadband waveguide-integrated superconducting single-photon detectors with high system detection efficiency. *Applied Physics Letters*, 118(15):154004, 04 2021.

[154] Angus Macleod. *Thin-Film Optical Filters*. CRC Press, 4th edition, 2010.

[155] Pochi Yeh. *Optical Waves in Layered Media*. Wiley, 2005.

[156] Alluxa Engineering Staff. Specifying plasma deposited hard coated optical thin film filters. https://alluxa.com/wp-content/uploads/2013/12/Specifying-Plasma-Deposited-Hard-Coated-Optical-Thin-Film-Filters.pdf, December 2012. White paper, Alluxa.

[157] H. Takesue and K. Inoue. 1.5-μm band quantum-correlated photon pair generation in dispersion-shifted fiber: suppression of noise photons by cooling fiber. *Opt. Express*, 13(20):7832–7839, 2005.

[158] A. Lohrmann, C. Perumangatt, A. Villar, and A. Ling. Broadband pumped polarization entangled photon-pair source in a linear beam displacement interferometer. *Appl. Phys. Lett.*, 116(2):021101, 2020.

[159] Hiroki Takesue and Kaoru Shimizu. Effects of multiple pairs on visibility measurements of entangled photons generated by spontaneous parametric processes. *Optics Communications*, 283(2):276–287, 2010.

[160] Sungeun Oh and Thomas Jennewein. Polarization entanglement with highly nondegenerate photon pairs enhanced by an effective walk-off-compensation method. *Phys. Rev. A*, 110:063515, Dec 2024.

[161] N.B. Lingaraju, H.-H. Lu, S. Seshadri, D.E. Leaird, A.M. Weiner, and J.M. Lukens. Adaptive bandwidth management for entanglement distribution in quantum networks. *Optica*, 8(3):329–332, 2021.

[162] S. Wang, X. Feng, S. Gao, Y. Shi, T. Dai, H. Yu, H.-K. Tsang, and D. Dai. On-chip reconfigurable optical add-drop multiplexer for hybrid wavelength/mode-division-multiplexing systems. *Optics Express*, 25(6):6712–6720, 2017.

[163] Félicien Appas, Florent Baboux, Maria I. Amanti, Aristide Lemaître, Fabien Boitier, Eleni Diamanti, and Sara Ducci. Flexible entanglement-distribution network with an AlGaAs chip for secure communications. *npj Quantum Information*, 7(1):118, July 2021.

[164] Yun Zheng, Chonghao Zhai, Dajian Liu, Jun Mao, Xiaojiong Chen, Tianxiang Dai, Jieshan Huang, Jueming Bao, Zhaorong Fu, Yeyu Tong, Xuetong Zhou, Yan Yang, Bo Tang, Zhihua Li, Yan Li, Qihuang Gong, Hon Ki Tsang, Daoxin Dai, and Jianwei Wang. Multichip multidimensional quantum networks with entanglement retrievability. *Science*, 381(6654):221–226, July 2023. Publisher: American Association for the Advancement of Science.

[165] Darius Bunandar, Anthony Lentine, Catherine Lee, Hong Cai, Christopher M. Long, Nicholas Boynton, Nicholas Martinez, Christopher DeRose, Changchen Chen, Matthew Grein, Douglas Trotter, Andrew Starbuck, Andrew Pomerene, Scott Hamilton, Franco N. C. Wong, Ryan Camacho, Paul Davids, Junji Urayama, and Dirk Englund. Metropolitan quantum key distribution with silicon photonics. *Phys. Rev. X*, 8:021009, Apr 2018.

[166] G. Singh, R. P. Yadav, and V. Janyani. Optimized digital optical switch using proton exchanged lithium niobate waveguides. *International Journal of Optics and Photonics*, 4(1):3–10, 2010. Accessed: 2025-05-24.

[167] Jian Wang, Hao Shen, Li Fan, Rui Wu, Ben Niu, Leo T. Varghese, Yi Xuan, Daniel E. Leaird, Xi Wang, Fuwan Gan, Andrew M. Weiner, and Minghao Qi. Reconfigurable radio-frequency arbitrary waveforms synthesized in a silicon photonic chip. *Nature Communications*, 6(1):5957, January 2015.

[168] Karanveer Singh, Ranjan Das, Abhinand Venugopalan, Souvaraj De, Mohamed I. Hosni, Linjie Zhou, and Thomas Schneider. Real-time reconfigurable on-chip photonic frequency decoder. *Opt. Express*, 31(19):30160–30170, Sep 2023.

[169] Xiang Guo, Chang-ling Zou, Carsten Schuck, Hojoong Jung, Risheng Cheng, and Hong X Tang. Parametric down-conversion photon-pair source on a nanophotonic chip. *Light: Science & Applications*, 6(5):e16249–e16249, May 2017.

[170] H. Jin, F. M. Liu, P. Xu, J. L. Xia, M. L. Zhong, Y. Yuan, J. W. Zhou, Y. X. Gong, W. Wang, and S. N. Zhu. On-chip generation and manipulation of entangled photons based on reconfigurable lithium-niobate waveguide circuits. *Phys. Rev. Lett.*, 113:103601, Sep 2014.

[171] Vijay S. S. Sundaram, Evan Manfreda-Schulz, Todd Hawthorne, Tony Roberts, Thomas Palone, Venkatesh Deenadayalan, Mario Ciminelli, Phil Battle, Gerald Leake, Daniel Coleman, Michael L. Fanto, Nick Vamivakas, Gregory A. Howland, and Stefan F. Preble. Heralded telecom single photons from a visible–telecom pair source on a hybrid ppktp–pic platform. *Optica Quantum*, 3(2):211–220, Apr 2025.

[172] Chenguang Li, Bo Xiong, and Tao Chu. Polarization-independent wavelength demultiplexer based on a single etched diffraction grating device. *Communications Engineering*, 2(1):4, January 2023.

[173] Alexander Y. Piggott, Jesse Lu, Konstantinos G. Lagoudakis, Jan Petykiewicz, Thomas M. Babinec, and Jelena Vučković. Inverse design and demonstration of a compact and broadband on-chip wavelength demultiplexer. *Nature Photonics*, 9(6):374–377, June 2015.

[174] Hesham Sakr, Yong Chen, Gregory T. Jasion, Thomas D. Bradley, John R. Hayes, Hans Christian H. Mulvad, Ian A. Davidson, Eric Numkam Fokoua, and Francesco Poletti. Hollow core optical fibres with comparable attenuation to silica fibres between 600 and 1100 nm. *Nature Communications*, 11(1):6030, November 2020.

[175] Jean-Marc Mérolla, Yuri Mazurenko, Jean-Pierre Goedgebuer, Henri Porte, and William T. Rhodes. Phase-modulation transmission system for quantum cryptography. *Opt. Lett.*, 24(2):104–106, Jan 1999.

[176] Jean-Marc Mérolla, Yuri Mazurenko, Jean-Pierre Goedgebuer, Laurent Duraffourg, Henri Porte, and William T. Rhodes. Quantum cryptographic device using single-photon phase modulation. *Phys. Rev. A*, 60:1899–1905, Sep 1999.

[177] Poolad Imany, Jose A. Jaramillo-Villegas, Ogaga D. Odele, Kyunghun Han, Daniel E. Leaird, Joseph M. Lukens, Pavel Lougovski, Minghao Qi, and Andrew M. Weiner. 50-ghz-spaced comb of high-dimensional frequency-bin entangled photons from an on-chip silicon nitride microresonator. *Opt. Express*, 26(2):1825–1840, Jan 2018.

[178] L. Olislager, J. Cussey, A. T. Nguyen, P. Emplit, S. Massar, J.-M. Merolla, and K. Phan Huy. Frequency-bin entangled photons. *Phys. Rev. A*, 82:013804, Jul 2010.

[179] Christof Bernhard, Bänz Bessire, Thomas Feurer, and André Stefanov. Shaping frequency-entangled qudits. *Phys. Rev. A*, 88:032322, Sep 2013.

[180] Joseph M. Lukens and Pavel Lougovski. Frequency-encoded photonic qubits for scalable quantum information processing. *Optica*, 4(1):8–16, Jan 2017.

[181] Marco Clementi, Federico Andrea Sabattoli, Massimo Borghi, Linda Gianini, Noemi Tagliavacche, Houssein El Dirani, Laurene Youssef, Nicola Bergamasco, Camille Petit-Etienne, Erwine Pargon, J. E. Sipe, Marco Liscidini, Corrado Sciancalepore, Matteo Galli, and Daniele Bajoni. Programmable frequency-bin quantum states in a nano-engineered silicon device. *Nature Communications*, 14(1):176, January 2023.

[182] Meritxell Cabrejo-Ponce, André Luiz Marques Muniz, Marcus Huber, and Fabian Steinlechner. High-dimensional entanglement for quantum communication in the frequency domain. *Laser & Photonics Reviews*, 17(9):2201010, 2023.

[183] Massimo Borghi, Noemi Tagliavacche, Federico Andrea Sabattoli, Houssein El Dirani, Laurene Youssef, Camille Petit-Etienne, Erwine Pargon, J.E. Sipe, Marco Liscidini, Corrado Sciancalepore, Matteo Galli, and Daniele Bajoni. Reconfigurable silicon photonic chip for the generation of frequency-bin-entangled qudits. *Phys. Rev. Appl.*, 19:064026, Jun 2023.

[184] Michael Kues, Christian Reimer, Piotr Roztocki, Luis Romero Cortés, Stefania Sciara, Benjamin Wetzel, Yanbing Zhang, Alfonso Cino, Sai T. Chu, Brent E. Little, David J. Moss, Lucia Caspani, José Azaña, and Roberto Morandotti. On-chip generation of high-dimensional entangled quantum states and their coherent control. *Nature*, 546(7660):622–626, June 2017.

[185] Sebastian Ecker, Frédéric Bouchard, Lukas Bulla, Florian Brandt, Oskar Kohout, Fabian Steinlechner, Robert Fickler, Mehul Malik, Yelena Guryanova, Rupert Ursin, and Marcus Huber. Overcoming noise in entanglement distribution. *Phys. Rev. X*, 9:041042, Nov 2019.

[186] P. Ben Dixon, Gregory A. Howland, James Schneeloch, and John C. Howell. Quantum mutual information capacity for high-dimensional entangled states. *Phys. Rev. Lett.*, 108:143603, Apr 2012.

[187] Daniele Cozzolino, Beatrice Da Lio, Davide Bacco, and Leif Katsuo Oxenløwe. High-dimensional quantum communication: benefits, progress, and future challenges. *Advanced Quantum Technologies*, 2(12):1900038, 2019.

[188] Dale Scerri, Ralph N. E. Malein, Brian D. Gerardot, and Erik M. Gauger. Frequency-encoded linear cluster states with coherent raman photons. *Phys. Rev. A*, 98:022318, Aug 2018.

[189] Matteo Pennacchietti, Brady Cunard, Shlok Nahar, Mohd Zeeshan, Sayan Gangopadhyay, Philip J. Poole, Dan Dalacu, Andreas Fognini, Klaus D. Jöns, Val Zwiller, Thomas Jennewein, Norbert Lütkenhaus, and Michael E. Reimer. Oscillating photonic Bell state from a semiconductor quantum dot for quantum key distribution. *Communications Physics*, 7(1):62, February 2024.

[190] Ming Lai Chan, Ziv Aqua, Alexey Tiranov, Barak Dayan, Peter Lodahl, and Anders S. Sørensen. Quantum state transfer between a frequency-encoded photonic qubit and a quantum-dot spin in a nanophotonic waveguide. *Phys. Rev. A*, 105:062445, Jun 2022.

[191] P. Laccotripes, T. Müller, R. M. Stevenson, J. Skiba-Szymanska, D. A. Ritchie, and A. J. Shields. Spin-photon entanglement with direct photon emission in the telecom C-band. *Nature Communications*, 15(1):9740, November 2024.

[192] Hsuan-Hao Lu, Marco Liscidini, Alexander L. Gaeta, Andrew M. Weiner, and Joseph M. Lukens. Frequency-bin photonic quantum information. *Optica*, 10(12):1655–1671, Dec 2023.

[193] W.B. Gao, P. Fallahi, E. Togan, A. Delteil, Y.S. Chin, J. Miguel-Sanchez, and A. Imamoğlu. Quantum teleportation from a propagating photon to a solid-state spin qubit. *Nature Communications*, 4(1):2744, November 2013.

[194] Navin B. Lingaraju, Hsuan-Hao Lu, Daniel E. Leaird, Steven Estrella, Joseph M. Lukens, and Andrew M. Weiner. Bell state analyzer for spectrally distinct photons. *Optica*, 9(3):280–283, Mar 2022.

[195] Xianxin Guo, Yefeng Mei, and Shengwang Du. Testing the bell inequality on frequency-bin entangled photon pairs using time-resolved detection. *Optica*, 4(4):388–392, Apr 2017.

[196] Fu-Yuan Wang, Bao-Sen Shi, and Guang-Can Guo. Observation of time correlation function of multimode two-photon pairs on a rubidium d2 line. *Opt. Lett.*, 33(19):2191–2193, Oct 2008.

[197] Matthieu Bloch, Steven W. McLaughlin, Jean-Marc Merolla, and Frédéric Patois. Frequency-coded quantum key distribution. *Opt. Lett.*, 32(3):301–303, Feb 2007.

[198] Noemi Tagliavacche, Massimo Borghi, Giulia Guarda, Domenico Ribezzo, Marco Liscidini, Davide Bacco, Matteo Galli, and Daniele Bajoni. Frequency-bin entanglement-based Quantum Key Distribution. *npj Quantum Information*, 11(1):60, April 2025.

[199] Laurent Olislager, Ismaël Mbodji, Erik Woodhead, Johann Cussey, Luca Furfaro, Philippe Emplit, Serge Massar, Kien Phan Huy, and Jean-Marc Merolla. Implementing two-photon interference in the frequency domain with electro-optic phase modulators. *New Journal of Physics*, 14(4):043015, apr 2012.

[200] Hsuan-Hao Lu, Karthik V. Myilswamy, Ryan S. Bennink, Suparna Seshadri, Mohammed S. Alshaykh, Junqiu Liu, Tobias J. Kippenberg, Daniel E. Leaird, Andrew M. Weiner, and Joseph M. Lukens. Bayesian tomography of high-dimensional on-chip biphoton frequency combs with randomized measurements. *Nature Communications*, 13(1):4338, July 2022.

[201] Andrej Krzic, Daniel Heinig, Matthias Goy, and Fabian Steinlechner. Dual-downlink quantum key distribution with entangled photons: prospects for daylight operation. In Kyriaki Minoglou, Nikos Karafolas, and Bruno Cugny, editors, *International Conference on Space Optics ICSO 2022*, volume 12777, page 1277726. International Society for Optics and Photonics, SPIE, 2023.

[202] L. F. Beesley, R. Griffiths, K. Hartley, O. J. D. Farley, F. Quatresooz, A. Rodríguez-Gómez, A. Comerón, M. Townson, D. Alaluf, and J. Osborn. Demonstration of 24-hour continuous optical turbulence monitoring in a city. *Opt. Express*, 33(5):10140–10149, Mar 2025.

[203] Manuel M. Freitas, Marco A. Fernandes, Pedro A. Loureiro, Paulo P. Monteiro, Fernando P. Guiomar, and Gil M. Fernandes. Robust and cost-efficient fso transmission using a multi-mode fiber-coupled receiver. *Opt. Continuum*, 3(2):227–233, Feb 2024.

[204] Ultan J. Daly, Fortune Iga, Aleksandr Boldin, Adam J. Vallance, Mitchell A. Cox, and Martin P. J. Lavery. Low-complexity turbulence resilience enabled by a multimode bi-directional transceiver. *Opt. Express*, 32(20):34314–34330, Sep 2024.

[205] Suguru Arisa, Yoshihisa Takayama, Hiroyuki Endo, Ryosuke Shimizu, Mikio Fujiwara, and Masahide Sasaki. Coupling efficiency of laser beam to multimode fiber for free space optical communication. In Zoran Sodnik, Bruno Cugny, and Nikos Karafolas, editors, *International Conference on Space Optics ICSO 2014*, volume 10563, page 105630Y. International Society for Optics and Photonics, SPIE, 2017.

[206] Donghao Zheng, Yan Li, Erhu Chen, Beibei Li, Deming Kong, Wei Li, and Jian Wu. Free-space to few-mode-fiber coupling under atmospheric turbulence. *Opt. Express*, 24(16):18739–18744, Aug 2016.

[207] Nicolas K. Fontaine, Roland Ryf, Yuanhang Zhang, Juan Carlos Alvarado-Zacarias, Sjoerd van der Heide, Mikael Mazur, Hanzi Huang, Haoshuo Chen, Rodrigo Amezcua-Correa, Guifang Li, Mark Capuzzo, Rose Kopf, Al Tate, Hugo Safar, Cristian Bolle, David T. Neilson, Ellsworth Burrows, Kwangwoong Kim, Marianne Bigot-Astruc, Frank Achten, Pierre Sillard, Adrian Amezcua-Correa, and Joel Carpenter. Digital turbulence compensation of free space optical link with multimode optical amplifier. In *45th European Conference on Optical Communication (ECOC 2019)*, pages 1–4, 2019.

[208] Yetian Huang, Hanzi Huang, Haoshuo Chen, Juan Carlos Alvarado, Nicolas K. Fontaine, Mikael Mazur, Qianwu Zhang, Roland Ryf, Rodrigo Amezcua-Correa, Yingxiong Song, Yingchun Li, and Wang Min. Free-space optics communications employing elliptical-aperture multimode diversity reception under anisotropic turbulence. *Journal of Lightwave Technology*, 40(5):1502–1508, 2022.

[209] Jeongwan Jin, Sascha Agne, Jean-Philippe Bourgoin, Yanbao Zhang, Norbert Lütkenhaus, and Thomas Jennewein. Demonstration of analyzers for multimode photonic time-bin qubits. *Phys. Rev. A*, 97:043847, Apr 2018.

[210] Stéphane Clemmen, Alessandro Farsi, Sven Ramelow, and Alexander L. Gaeta. Ramsey interference with single photons. *Phys. Rev. Lett.*, 117:223601, Nov 2016.

[211] Chaohan Cui, Kaushik P. Seshadreesan, Saikat Guha, and Linran Fan. High-dimensional frequency-encoded quantum information processing with passive photonics and time-resolving detection. *Phys. Rev. Lett.*, 124:190502, May 2020.

[212] Richard P. Feynman, Robert B. Leighton, and Matthew Sands. *The Feynman Lectures on Physics, Vol. I, Chapter 48: Beats*. California Institute of Technology, 1963. https://www.feynmanlectures.caltech.edu/I_48.html.

[213] Tomohiro Yamazaki, Tomoaki Arizono, Toshiki Kobayashi, Rikizo Ikuta, and Takashi Yamamoto. Linear optical quantum computation with frequency-comb qubits and passive devices. *Phys. Rev. Lett.*, 130:200602, May 2023.

[214] Manuel Erhard, Mario Krenn, and Anton Zeilinger. Advances in high-dimensional quantum entanglement. *Nature Reviews Physics*, 2(7):365–381, July 2020.

[215] Nurul T. Islam, Clinton Cahall, Andrés Aragoneses, A. Lezama, Jungsang Kim, and Daniel J. Gauthier. Robust and stable delay interferometers with application to d-dimensional time-frequency quantum key distribution. *Phys. Rev. Appl.*, 7:044010, Apr 2017.

[216] Thomas Brougham, Stephen M Barnett, Kevin T McCusker, Paul G Kwiat, and Daniel J Gauthier. Security of high-dimensional quantum key distribution protocols using franson interferometers. *Journal of Physics B: Atomic, Molecular and Optical Physics*, 46(10):104010, may 2013.

[217] Max Born and Emil Wolf. *Principles of Optics: 60th Anniversary Edition*. Cambridge University Press, 7 edition, 2019.

[218] Teledyne LeCroy. *WaveRunner 6Zi Oscilloscope Datasheet*, 2024. Accessed: Sep. 30, 2024.

[219] Micro Photon Devices. *PDM Series: Single Photon Counting Module Datasheet*, 2024. Accessed: Sep. 30, 2024.

[220] Excelitas Technologies. *SPCM-AQRH: Single Photon Counting Module Datasheet*, 2024. Accessed: Sep. 30, 2024.

[221] A. Jäggi, U. Hugentobler, H. Bock, and G. Beutler. Precise orbit determination for grace using undifferenced or doubly differenced gps data. *Advances in Space Research*, 39(10):1612–1619, 2007.

[222] Keke Zhang, Xingxing Li, Jiaqi Wu, Yongqiang Yuan, Xin Li, Xiaohong Zhang, and Wei Zhang. Precise orbit determination for leo satellites with ambiguity resolution: Improvement and comparison. *Journal of Geophysical Research: Solid Earth*, 126(9):e2021JB022491, 2021. e2021JB022491 2021JB022491.

[223] Zhigui Kang, Byron Tapley, Srinivas Bettadpur, John Ries, Peter Nagel, and Rick Pastor. Precise orbit determination for the GRACE mission using only GPS data. *Journal of Geodesy*, 80(6):322–331, September 2006.

[224] Daniel Arnold, Oliver Montenbruck, Stefan Hackel, and Krzysztof Sośnica. Satellite laser ranging to low Earth orbiters: orbit and network validation. *Journal of Geodesy*, 93(11):2315–2334, November 2019.

[225] John J. Degnan. *Millimeter Accuracy Satellite Laser Ranging: a Review*, pages 133–162. American Geophysical Union (AGU), 1993.

[226] Steven T. Cundiff and Jun Ye. Colloquium: Femtosecond optical frequency combs. *Rev. Mod. Phys.*, 75:325–342, Mar 2003.

[227] Matthias Lezius, Tobias Wilken, Christian Deutsch, Michele Giunta, Olaf Mandel, Andy Thaller, Vladimir Schkolnik, Max Schiemangk, Aline Dinkelaker, Anja Kohfeldt, Andreas Wicht, Markus Krutzik, Achim Peters, Ortwin Hellmig, Hannes Duncker, Klaus Sengstock, Patrick Windpassinger, Kai Lampmann, Thomas Hülsing, Theodor W. Hänsch, and Ronald Holzwarth. Space-borne frequency comb metrology. *Optica*, 3(12):1381–1387, Dec 2016.

[228] Giuseppe Vallone, Daniele Dequal, Marco Tomasin, Francesco Vedovato, Matteo Schiavon, Vincenza Luceri, Giuseppe Bianco, and Paolo Villoresi. Interference at the single photon level along satellite-ground channels. *Phys. Rev. Lett.*, 116:253601, Jun 2016.

[229] Yamaç Dikmelik and Frederic M. Davidson. Fiber-coupling efficiency for free-space optical communication through atmospheric turbulence. *Appl. Opt.*, 44(23):4946–4952, Aug 2005.

[230] Jeongwan Jin, Jean-Philippe Bourgoin, Ramy Tannous, Sascha Agne, Christopher J. Pugh, Katanya B. Kuntz, Brendon L. Higgins, and Thomas Jennewein. Genuine time-bin-encoded quantum key distribution over a turbulent depolarizing free-space channel. *Opt. Express*, 27(26):37214–37223, Dec 2019.

[231] Chris Zeitler, Trent M. Graham, Joseph Chapman, Herbert Bernstein, and Paul G. Kwiat. Super-dense teleportation for space applications. In Hamid Hemmati and Don M. Boroson, editors, *Free-Space Laser Communication and Atmospheric Propagation XXVIII*, volume 9739, page 973912. International Society for Optics and Photonics, SPIE, 2016.

[232] Trent Graham, Christopher Zeitler, Joseph Chapman, Paul Kwiat, Hamid Javadi, and Herbert Bernstein. Superdense teleportation and quantum key distribution for space applications. In *2015 IEEE International Conference on Space Optical Systems and Applications (ICSOS)*, pages 1–7, 2015.

[233] Gordon G. Shepherd, William A. Gault, D. W. Miller, Z. Pasturczyk, Sean F. Johnston, P. R. Kosteniuk, J. W. Haslett, David J. W. Kendall, and J. R. Wimperis. Wamdii: wide-angle michelson doppler imaging interferometer for spacelab. *Appl. Opt.*, 24(11):1571–1584, Jun 1985.

[234] Dong Liu, Chris Hostetler, Ian Miller, Anthony Cook, and Johnathan Hair. System analysis of a tilted field-widened michelson interferometer for high spectral resolution lidar. *Opt. Express*, 20(2):1406–1420, Jan 2012.

[235] Bahaa E. A. Saleh and Malvin Carl Teich. *Fiber Optics*, chapter 8, pages 272–309. John Wiley & Sons, Ltd, 1991.

[236] Hui-Nan Wu, Yu-Huai Li, Bo Li, Xiang You, Run-Ze Liu, Ji-Gang Ren, Juan Yin, Chao-Yang Lu, Yuan Cao, Cheng-Zhi Peng, and Jian-Wei Pan. Single-photon interference over 8.4 km urban atmosphere: Toward testing quantum effects in curved spacetime with photons. *Phys. Rev. Lett.*, 133:020201, Jul 2024.

[237] Lukas Kral, Ivan Prochazka, and Karel Hamal. Optical signal path delay fluctuations caused by atmospheric turbulence. *Opt. Lett.*, 30(14):1767–1769, Jul 2005.

[238] Darryl P. Greenwood. Bandwidth specification for adaptive optics systems∗. *J. Opt. Soc. Am.*, 67(3):390–393, Mar 1977.

[239] David L. Fried. Greenwood frequency measurements. *J. Opt. Soc. Am. A*, 7(5):946–947, May 1990.

[240] Mark T. Gruneisen, Michael B. Flanagan, and Brett A. Sickmiller. Modeling satellite-Earth quantum channel downlinks with adaptive-optics coupling to single-mode fibers. *Optical Engineering*, 56(12):126111, 2017.

[241] L. C. Andrews, R. L. Phillips, C. Y. Hopen, and M. A. Al-Habash. Theory of optical scintillation. *J. Opt. Soc. Am. A*, 16(6):1417–1429, Jun 1999.

[242] Costantino Agnesi, Luca Calderaro, Daniele Dequal, Francesco Vedovato, Matteo Schiavon, Alberto Santamato, Vincenza Luceri, Giuseppe Bianco, Giuseppe Vallone, and Paolo Villoresi. Sub-ns timing accuracy for satellite quantum communications. *J. Opt. Soc. Am. B*, 36(3):B59–B64, Mar 2019.

[243] Mark T. Gruneisen, Mark L. Eickhoff, Scott C. Newey, Kurt E. Stoltenberg, Jeffery F. Morris, Michael Bareian, Mark A. Harris, Denis W. Oesch, Michael D. Oliker, Michael B. Flanagan, Brian T. Kay, Johnathan D. Schiller, and R. Nicholas Lanning.

Adaptive-optics-enabled quantum communication: A technique for daytime space-to-earth links. *Phys. Rev. Appl.*, 16:014067, Jul 2021.

[244] iXblue. *MX-LN Series High Bandwidth Modulators*, February 2022. Accessed: 2024-09-25.

[245] Thorlabs. Electro-optic intensity modulators (eo modulators), 2024. Accessed: 2024-09-25.

[246] Y. J. Lu, R. L. Campbell, and Z. Y. Ou. Mode-locked two-photon states. *Phys. Rev. Lett.*, 91:163602, Oct 2003.

[247] Zhenda Xie, Tian Zhong, Sajan Shrestha, XinAn Xu, Junlin Liang, Yan-Xiao Gong, Joshua C. Bienfang, Alessandro Restelli, Jeffrey H. Shapiro, Franco N. C. Wong, and Chee Wei Wong. Harnessing high-dimensional hyperentanglement through a biphoton frequency comb. *Nature Photonics*, 9(8):536–542, August 2015.

[248] Christian Reimer, Michael Kues, Piotr Roztocki, Benjamin Wetzel, Fabio Grazioso, Brent E. Little, Sai T. Chu, Tudor Johnston, Yaron Bromberg, Lucia Caspani, David J. Moss, and Roberto Morandotti. Generation of multiphoton entangled quantum states by means of integrated frequency combs. *Science*, 351(6278):1176–1180, 2016.

[249] Jose A. Jaramillo-Villegas, Poolad Imany, Ogaga D. Odele, Daniel E. Leaird, Zhe-Yu Ou, Minghao Qi, and Andrew M. Weiner. Persistent energy-time entanglement covering multiple resonances of an on-chip biphoton frequency comb. *Optica*, 4(6):655–658, Jun 2017.

[250] Tian-Ming Zhao, Han Zhang, Jian Yang, Zi-Ru Sang, Xiao Jiang, Xiao-Hui Bao, and Jian-Wei Pan. Entangling different-color photons via time-resolved measurement and active feed forward. *Phys. Rev. Lett.*, 112:103602, Mar 2014.

[251] G. Vittorini, D. Hucul, I. V. Inlek, C. Crocker, and C. Monroe. Entanglement of distinguishable quantum memories. *Phys. Rev. A*, 90:040302, Oct 2014.

[252] Sofiane Merkouche, Valérian Thiel, Alex O. C. Davis, and Brian J. Smith. Heralding multiple photonic pulsed bell pairs via frequency-resolved entanglement swapping. *Phys. Rev. Lett.*, 128:063602, Feb 2022.

[253] Boris Korzh, Qing-Yuan Zhao, Jason P. Allmaras, Simone Frasca, Travis M. Autry, Eric A. Bersin, Andrew D. Beyer, Ryan M. Briggs, Bruce Bumble, Marco Colangelo,

Garrison M. Crouch, Andrew E. Dane, Thomas Gerrits, Adriana E. Lita, Francesco Marsili, Galan Moody, Cristián Peña, Edward Ramirez, Jake D. Rezac, Neil Sinclair, Martin J. Stevens, Angel E. Velasco, Varun B. Verma, Emma E. Wollman, Si Xie, Di Zhu, Paul D. Hale, Maria Spiropulu, Kevin L. Silverman, Richard P. Mirin, Sae Woo Nam, Alexander G. Kozorezov, Matthew D. Shaw, and Karl K. Berggren. Demonstration of sub-3 ps temporal resolution with a superconducting nanowire single-photon detector. *Nature Photonics*, 14(4):250–255, April 2020.

[254] ID Quantique. ID281 Superconducting Nanowire Series. https://www.idquantique.com/quantum-detection-systems/the-id281-series/, n.d. Accessed: 2025-06-05.

[255] Single Quantum. Solutions. https://www.singlequantum.com/solutions/, 2025. Accessed: 2025-06-06.

[256] Stuart J. Freedman and John F. Clauser. Experimental test of local hidden-variable theories. *Physical Review Letters*, 28(14):938–941, April 1972.

[257] J. D. Franson. Bell inequality for position and time. *Phys. Rev. Lett.*, 62:2205–2208, May 1989.

[258] Marco Liscidini and J. E. Sipe. Scalable and efficient source of entangled frequency bins. *Optics Letters*, 44(11):2625, May 2019.

[259] Massimo Borghi, Noemi Tagliavacche, Federico Andrea Sabattoli, Houssein El Dirani, Laurene Youssef, Camille Petit-Etienne, Erwine Pargon, J. E. Sipe, Marco Liscidini, Corrado Sciancalepore, Matteo Galli, and Daniele Bajoni. A reconfigurable silicon photonics chip for the generation of frequency bin entangled qudits, 2023.

[260] Yiming Pang, Joshua E. Castro, Trevor J. Steiner, Liao Duan, Noemi Tagliavacche, Massimo Borghi, Lillian Thiel, Nicholas Lewis, John E. Bowers, Marco Liscidini, and Galan Moody. Versatile chip-scale platform for high-rate entanglement generation using an AlGaAs microresonator array. *PRX Quantum*, 6:010338, Mar 2025.

[261] D. J. Saunders, S. J. Jones, H. M. Wiseman, and G. J. Pryde. Experimental EPR-steering using Bell-local states. *Nature Physics*, 6(11):845–849, November 2010.

[262] Hans Maassen and J. B. M. Uffink. Generalized entropic uncertainty relations. *Phys. Rev. Lett.*, 60:1103–1106, Mar 1988.

[263] James Schneeloch, Curtis J. Broadbent, Stephen P. Walborn, Eric G. Cavalcanti, and John C. Howell. Einstein-podolsky-rosen steering inequalities from entropic uncertainty relations. *Phys. Rev. A*, 87:062103, Jun 2013.

[264] M. D. Reid. Demonstration of the einstein-podolsky-rosen paradox using nondegenerate parametric amplification. *Phys. Rev. A*, 40:913–923, Jul 1989.

[265] E. G. Cavalcanti, S. J. Jones, H. M. Wiseman, and M. D. Reid. Experimental criteria for steering and the einstein-podolsky-rosen paradox. *Phys. Rev. A*, 80:032112, Sep 2009.

[266] Ramy Tannous, Zhangdong Ye, Jeongwan Jin, Katanya B. Kuntz, Norbert Lütkenhaus, and Thomas Jennewein. Demonstration of a 6 state-4 state reference frame independent channel for quantum key distribution. *Applied Physics Letters*, 115(21):211103, November 2019. _eprint: https://pubs.aip.org/aip/apl/article-pdf/doi/10.1063/1.5125700/13286491/211103_1_online.pdf.

[267] Liang Zhang, Chaohan Cui, Jianchang Yan, Yanan Guo, Junxi Wang, and Linran Fan. On-chip parallel processing of quantum frequency comb. *npj Quantum Information*, 9(1):57, June 2023.

[268] Rikizo Ikuta, Yoshiaki Kusaka, Tsuyoshi Kitano, Hiroshi Kato, Takashi Yamamoto, Masato Koashi, and Nobuyuki Imoto. Wide-band quantum interface for visible-to-telecommunication wavelength conversion. *Nature Communications*, 2(1):537, November 2011.

[269] Rikizo Ikuta, Toshiki Kobayashi, Tetsuo Kawakami, Shigehito Miki, Masahiro Yabuno, Taro Yamashita, Hirotaka Terai, Masato Koashi, Tetsuya Mukai, Takashi Yamamoto, and Nobuyuki Imoto. Polarization insensitive frequency conversion for an atom-photon entanglement distribution via a telecom network. *Nature Communications*, 9(1):1997, May 2018.

[270] Tim van Leent, Matthias Bock, Florian Fertig, Robert Garthoff, Sebastian Eppelt, Yiru Zhou, Pooja Malik, Matthias Seubert, Tobias Bauer, Wenjamin Rosenfeld, Wei Zhang, Christoph Becher, and Harald Weinfurter. Entangling single atoms over 33 km telecom fibre. *Nature*, 607(7917):69–73, July 2022.

[271] Sebastian Philipp Neumann, Alexander Buchner, Lukas Bulla, Martin Bohmann, and Rupert Ursin. Continuous entanglement distribution over a transnational 248 km fiber link. *Nature Communications*, 13(1):6134, October 2022.

[272] Lixing You, Jia Quan, Yong Wang, Yuexue Ma, Xiaoyan Yang, Yanjie Liu, Hao Li, Jianguo Li, Juan Wang, Jingtao Liang, Zhen Wang, and Xiaoming Xie. Superconducting nanowire single photon detection system for space applications. *Opt. Express*, 26(3):2965–2971, Feb 2018.

[273] Haizheng Dang, Tao Zhang, Rui Zha, Jun Tan, Jiaqi Li, Yongjiang Zhao, Bangjian Zhao, Han Tan, and Renjun Xue. Development of 2-k space cryocoolers for cooling the superconducting nanowire single photon detector. *IEEE Transactions on Applied Superconductivity*, 29(5):1–4, 2019.

[274] Vincent Kotsubo, R. Radebaugh, P. Hendershott, M. Bonczyski, B. Wilson, S. W. Nam, and J. N. Ullom. Compact 2.2 k cooling system for superconducting nanowire single photon detectors. *IEEE Transactions on Applied Superconductivity*, 27(4):1–5, 2017.

[275] Donald R. Herriott and Harry J. Schulte. Folded optical delay lines. *Appl. Opt.*, 4(8):883–889, Aug 1965.

[276] Brian Pepper, Roohollah Ghobadi, Evan Jeffrey, Christoph Simon, and Dirk Bouwmeester. Optomechanical superpositions via nested interferometry. *Phys. Rev. Lett.*, 109:023601, Jul 2012.

[277] Tian Zhong, Jonathan M. Kindem, John G. Bartholomew, Jake Rochman, Ioana Craiciu, Evan Miyazono, Marco Bettinelli, Enrico Cavalli, Varun Verma, Sae Woo Nam, Francesco Marsili, Matthew D. Shaw, Andrew D. Beyer, and Andrei Faraon. Nanophotonic rare-earth quantum memory with optically controlled retrieval. *Science*, 357(6358):1392–1395, 2017.

[278] M. Hosseini, G. Campbell, B. M. Sparkes, P. K. Lam, and B. C. Buchler. Unconditional room-temperature quantum memory. *Nature Physics*, 7(10):794–798, October 2011.

[279] M. Hosseini, B.M. Sparkes, G. Campbell, P.K. Lam, and B.C. Buchler. High efficiency coherent optical memory with warm rubidium vapour. *Nature Communications*, 2(1):174, February 2011.

[280] Neil Sinclair, Erhan Saglamyurek, Hassan Mallahzadeh, Joshua A. Slater, Mathew George, Raimund Ricken, Morgan P. Hedges, Daniel Oblak, Christoph Simon, Wolfgang Sohler, and Wolfgang Tittel. Spectral multiplexing for scalable quantum photonics using an atomic frequency comb quantum memory and feed-forward control. *Phys. Rev. Lett.*, 113:053603, Jul 2014.

[281] Alessandro Seri, Dario Lago-Rivera, Andreas Lenhard, Giacomo Corrielli, Roberto Osellame, Margherita Mazzera, and Hugues de Riedmatten. Quantum storage of frequency-multiplexed heralded single photons. *Phys. Rev. Lett.*, 123:080502, Aug 2019.

[282] Stephane Vinet, Ramy Tannous, and Thomas Jennewein. Quantum key distribution simulation, 2024.

[283] J.R. Johansson, P.D. Nation, and Franco Nori. Qutip: An open-source python framework for the dynamics of open quantum systems. *Computer Physics Communications*, 183(8):1760–1772, 2012.

[284] Holloway, Catherine. Towards real-world adoption of quantum key distribution using entangled photons. Master's thesis, 2012.

[285] Stéphane Vinet and Thomas Jennewein. Photon-number resolving detectors for quantum key distribution. in preparation.

[286] Ebubechukwu O. Ilo-Okeke, Louis Tessler, Jonathan P. Dowling, and Tim Byrnes. Remote quantum clock synchronization without synchronized clocks. *npj Quantum Information*, 4(1):40, August 2018.

[287] Sheng-Kai Liao, Wen-Qi Cai, Wei-Yue Liu, Liang Zhang, Yang Li, Ji-Gang Ren, Juan Yin, Qi Shen, Yuan Cao, Zheng-Ping Li, Feng-Zhi Li, Xia-Wei Chen, Li-Hua Sun, Jian-Jun Jia, Jin-Cai Wu, Xiao-Jun Jiang, Jian-Feng Wang, Yong-Mei Huang, Qiang Wang, Yi-Lin Zhou, Lei Deng, Tao Xi, Lu Ma, Tai Hu, Qiang Zhang, Yu-Ao Chen, Nai-Le Liu, Xiang-Bin Wang, Zhen-Cai Zhu, Chao-Yang Lu, Rong Shu, Cheng-Zhi Peng, Jian-Yu Wang, and Jian-Wei Pan. Satellite-to-ground quantum key distribution. *Nature*, 549(7670):43–47, September 2017.

[288] Juan Yin, Yuan Cao, Yu-Huai Li, Ji-Gang Ren, Sheng-Kai Liao, Liang Zhang, Wen-Qi Cai, Wei-Yue Liu, Bo Li, Hui Dai, Ming Li, Yong-Mei Huang, Lei Deng, Li Li, Qiang Zhang, Nai-Le Liu, Yu-Ao Chen, Chao-Yang Lu, Rong Shu, Cheng-Zhi Peng, Jian-Yu Wang, and Jian-Wei Pan. Satellite-to-ground entanglement-based quantum key distribution. *Phys. Rev. Lett.*, 119:200501, Nov 2017.

[289] B.-S. Shi, Y.-K. Jiang, and G.-C. Guo. Quantum key distribution using different-frequency photons. *Applied Physics B*, 70(3):415–417, March 2000.

[290] N. Takato, T. Kominato, A. Sugita, K. Jinguji, H. Toba, and M. Kawachi. Silica-based integrated optic mach-zehnder multi/demultiplexer family with channel spacing of 0.01-250 nm. *IEEE Journal on Selected Areas in Communications*, 8(6):1120–1127, 1990.

[291] Chi-Hang Fred Fung and Hoi-Kwong Lo. Security proof of a three-state quantum-key-distribution protocol without rotational symmetry. *Phys. Rev. A*, 74:042342, Oct 2006.

[292] Valerio Scarani, Helle Bechmann-Pasquinucci, Nicolas J. Cerf, Miloslav Dušek, Norbert Lütkenhaus, and Momtchil Peev. The security of practical quantum key distribution. *Rev. Mod. Phys.*, 81:1301–1350, Sep 2009.

[293] Boris Desiatov, Amirhassan Shams-Ansari, Mian Zhang, Cheng Wang, and Marko Lončar. Ultra-low-loss integrated visible photonics using thin-film lithium niobate. *Optica*, 6(3):380–384, Mar 2019.

[294] Tanvirul Islam, Jasminder S. Sidhu, Brendon L. Higgins, Thomas Brougham, Tom Vergoossen, Daniel K.L. Oi, Thomas Jennewein, and Alexander Ling. Finite-resource performance of small-satellite-based quantum-key-distribution missions. *PRX Quantum*, 5:030101, Jul 2024.

[295] O. Gittsovich, N. J. Beaudry, V. Narasimhachar, R. Romero Alvarez, T. Moroder, and N. Lütkenhaus. Squashing model for detectors and applications to quantum-key-distribution protocols. *Phys. Rev. A*, 89:012325, Jan 2014.

[296] Carlo Liorni, Hermann Kampermann, and Dagmar Bruß. Satellite-based links for quantum key distribution: beam effects and weather dependence. *New Journal of Physics*, 21(9):093055, sep 2019.

[297] Toshiki Kobayashi, Rikizo Ikuta, Shuto Yasui, Shigehito Miki, Taro Yamashita, Hirotaka Terai, Takashi Yamamoto, Masato Koashi, and Nobuyuki Imoto. Frequency-domain Hong-Ou-Mandel interference. *Nature Photonics*, 10(7):441–444, July 2016.

[298] Stephane Vinet, Yujie Zhang, Marco Clementi, Marcello Bacchi, Massimo Giacomin, Matteo Galli, Daniele Bajoni, and Thomas Jennewein. Frequency-bin quantum communication data analysis. https://github.com/stephanevinet-q/frequencybin, 2025. Accessed: 2025-06-24.

[299] Johannes Pseiner, Lukas Achatz, Lukas Bulla, Martin Bohmann, and Rupert Ursin. Experimental wavelength-multiplexed entanglement-based quantum cryptography. *Quantum Science and Technology*, 6(3):035013, jun 2021.

[300] Mohinder S Grewal, Lawrence R Weill, and Angus P Andrews. *Global positioning systems, inertial navigation, and integration*. John Wiley & Sons, 2007.

[301] Ebubechukwu O. Ilo-Okeke, Louis Tessler, Jonathan P. Dowling, and Tim Byrnes. Remote quantum clock synchronization without synchronized clocks. *npj Quantum Information*, 4(1):40, August 2018.

[302] Xu Liu, Jingyuan Liu, Rong Xue, Heqing Wang, Hao Li, Xue Feng, Fang Liu, Kaiyu Cui, Zhen Wang, Lixing You, Yidong Huang, and Wei Zhang. 40-user fully connected entanglement-based quantum key distribution network without trusted node. *PhotoniX*, 3(1):2, January 2022.

[303] FangXing Xu, Wei Chen, Shuang Wang, ZhenQiang Yin, Yang Zhang, Yun Liu, Zheng Zhou, YiBo Zhao, HongWei Li, Dong Liu, ZhengFu Han, and GuangCan Guo. Field experiment on a robust hierarchical metropolitan quantum cryptography network. *Chinese Science Bulletin*, 54(17):2991–2997, September 2009.

[304] Zhantong Qi, Yuanhua Li, Yiwen Huang, Juan Feng, Yuanlin Zheng, and Xianfeng Chen. A 15-user quantum secure direct communication network. *Light: Science & Applications*, 10(1):183, September 2021.

[305] Zheng-Da Li, Rui Zhang, Xu-Fei Yin, Li-Zheng Liu, Yi Hu, Yu-Qiang Fang, Yue-Yang Fei, Xiao Jiang, Jun Zhang, Li Li, Nai-Le Liu, Feihu Xu, Yu-Ao Chen, and Jian-Wei Pan. Experimental quantum repeater without quantum memory. *Nature Photonics*, 13(9):644–648, June 2019.

[306] Juan Yin, Yuan Cao, Yu-Huai Li, Ji-Gang Ren, Sheng-Kai Liao, Liang Zhang, Wen-Qi Cai, Wei-Yue Liu, Bo Li, Hui Dai, Ming Li, Yong-Mei Huang, Lei Deng, Li Li, Qiang Zhang, Nai-Le Liu, Yu-Ao Chen, Chao-Yang Lu, Rong Shu, Cheng-Zhi Peng, Jian-Yu Wang, and Jian-Wei Pan. Satellite-to-Ground Entanglement-Based Quantum Key Distribution. *Phys. Rev. Lett.*, 119(20):200501, November 2017.

[307] Juan Yin, Yu-Huai Li, Sheng-Kai Liao, Meng Yang, Yuan Cao, Liang Zhang, Ji-Gang Ren, Wen-Qi Cai, Wei-Yue Liu, Shuang-Lin Li, Rong Shu, Yong-Mei Huang, Lei Deng, Li Li, Qiang Zhang, Nai-Le Liu, Yu-Ao Chen, Chao-Yang Lu, Xiang-Bin Wang, Feihu Xu, Jian-Yu Wang, Cheng-Zhi Peng, Artur K. Ekert, and Jian-Wei Pan.

Entanglement-based secure quantum cryptography over 1,120 kilometres. *Nature*, 582(7813):501–505, June 2020.

[308] G. A. Vanasse. *Spectrometric Techniques*, volume 1. Academic Press, San Diego, 1977.

[309] Sungeun Oh. *Entangled Photon Source for a Long-Distance Quantum Key Distribution*. Phd thesis, University of Waterloo, Waterloo, Ontario, Canada, June 2024. Advisor: Thomas Jennewein.

[310] S. Langenfeld, P. Thomas, O. Morin, and G. Rempe. Quantum Repeater Node Demonstrating Unconditionally Secure Key Distribution. *Phys. Rev. Lett.*, 126(23):230506, June 2021.

[311] Peter W. Shor and John Preskill. Simple proof of security of the bb84 quantum key distribution protocol. *Phys. Rev. Lett.*, 85:441–444, Jul 2000.

APPENDICES

Appendix A

Quantum Key Distribution Simulation

The quantum key distribution simulation code was written using the QuTIP toolbox in Python [283]. It is based on a QKD code written by Catherine Holloway [134, 284]. We assume the protocol is symmetric with respect to the σ_X and σ_Z bases thus we find that $\delta_b = \delta_p$[1]. We calculate the detection probabilities for the σ_Z basis according to the squashing model below with the following parameters:

χ : squeezing parameter
loss_a: Efficiency of the ground quantum channel
loss_b: Efficiency of the satellite quantum channel
n_factor_a: Dark count rate in ground detectors
n_factor_b: Dark count rate in satellite detectors
dim: Fock space dimension
N: number of multiplexed channels
τ: Detector dead time
f_ec: error correction factor.

A.1 Squashing model

The following function calculates the measurement probabilities for an SPDC state using a squashing model that accounts for non-ideal detectors and multi-photon events [295]. In

[1]This assumption is valid in the asymptotic limit, for the finite case one must consider the impact of statistical fluctuations on δ_p [133].

this framework, the receiver's measurements are effectively performed on the Fock space restricted to the vacuum and single-photon subspace ($\{|0\rangle, |1\rangle\}$) by probabilistically assigning multi-photon events — for instance, double-click events where both H and V detectors click are randomly assigned to H or V with 50–50 probability.

Listing A.1: Squashing model

```
def measure_2folds_4modes_squashing_optimized(dim, chi, proj, proj2, tau):
    vacc = basis(dim, 0)
    det_exp = zeros((2, 2, 2, 2))

    H_sq = 1j * chi * (tensor(create(dim), create(dim)) +
                       tensor(destroy(dim), destroy(dim)))
    U_sq = H_sq.expm()
    spdc = U_sq * tensor(vacc, vacc)
    psi_i = tensor(spdc, spdc)

    out_i = reshape(
        transpose(
            reshape(psi_i.full(), (dim, dim, dim, -1)),
            (0, 3, 2, 1)
        ),
        (dim * dim * dim * dim, -1)
    )
    psi_i = Qobj(out_i, dims=[[dim, dim, dim, dim], [1, 1, 1, 1]])

    for i in range(2):
    for j in range(2):
        for k in range(2):
            for l in range(2):
                det_exp[i][j][k][l] = abs(expect(
                    tensor(proj[i], proj[j], proj2[k], proj2[l]),
                    psi_i
                ))

    HH = (det_exp[0][1][0][1] +
          0.5 * (det_exp[0][0][0][1] + det_exp[0][1][0][0]) +
          0.25 * det_exp[0][0][0][0]) / (
         1 + tau * (det_exp[0][1][0][1] +
```

```
                    0.5 * (det_exp[0][0][0][1] + det_exp[0][1][0][0]) +
                    0.25 * det_exp[0][0][0][0]))

VV = (det_exp[1][0][1][0] +
      0.5 * (det_exp[0][0][1][0] + det_exp[1][0][0][0]) +
      0.25 * det_exp[0][0][0][0]) / (
     1 + tau * (det_exp[1][0][1][0] +
                0.5 * (det_exp[0][0][1][0] + det_exp[1][0][0][0]) +
                0.25 * det_exp[0][0][0][0]))

HV = (det_exp[0][1][1][0] +
      0.5 * (det_exp[0][0][1][0] + det_exp[0][1][0][0]) +
      0.25 * det_exp[0][0][0][0]) / (
     1 + tau * (det_exp[0][1][1][0] +
                0.5 * (det_exp[0][0][1][0] + det_exp[0][1][0][0]) +
                0.25 * det_exp[0][0][0][0]))

VH = (det_exp[1][0][0][1] +
      0.5 * (det_exp[0][0][0][1] + det_exp[1][0][0][0]) +
      0.25 * det_exp[0][0][0][0]) / (
     1 + tau * (det_exp[1][0][0][1] +
                0.5 * (det_exp[0][0][0][1] + det_exp[1][0][0][0]) +
                0.25 * det_exp[0][0][0][0]))

return [HH, HV, VH, VV]
```

Note that `det_exp` effectively calculates: $\left|\langle\psi_i|\,\Pi_{ijkl}\,|\psi_i\rangle\right|$, where $\Pi_{ijkl} = \Pi_i \otimes \Pi_j \otimes \Pi'_k \otimes \Pi'_l$, $\Pi_{i(j)} =$ `proj[i(j)]`, and $\Pi'_{k(l)} =$ `proj2[k(l)]` denote the projectors acting on the corresponding Alice and Bob's subsystems. The probabilities associated to HH, VV, HV, VH are then computed according to the detector outcomes with a normalization factor given by the detector dead time (see Eq. 2.6).

A.2 Secure key rate calculation

From the detection probabilities calculated above (relabeled `probs2f_i[i]` below), we then calculate the two-fold coincidence rate and the quantum bit error rate, respectively, according to `twofolds` $= \sum_i$ `probs2f_i[i]` and qber $= \frac{\mathrm{N_{errors}}}{\mathrm{N_{total}}} = \frac{\texttt{probs2f_i[0]+probs2f_i[3]}}{\sum_i \texttt{probs2f_i[i]}}$,

where `probs2f_i[0]` and `probs2f_i[3]` correspond to detection outcome HH and VV respectively. These detection outcomes contribute to the error rate for our input state $|\Psi^-\rangle$. The secure key rate is then calculated using Eq. 2.7.

Listing A.2: Simulation of QKD with entanglement source

```
def simqkdentanglement(
chi, loss_a, loss_b, n_factor_a, n_factor_b, dim, N
):
    vacc = basis(N, 0)
    qber_list = []
    twofolds_list = []

    for i in range(N):
        a_det = BucketDetector_realistic_detector(N, loss_a, n_factor_a)
        b_det = BucketDetector_realistic_detector(N, loss_b, n_factor_b)

        probs2f_i = measure_2folds_4modes_squashing_optimized(
        N, chi, a_det, b_det, tau
        )

        twofolds_i =
        probs2f_i[0] + probs2f_i[1] + probs2f_i[2] + probs2f_i[3]
        twofolds_list.append(twofolds_i)

        qber_i = probs2f_i[0] + probs2f_i[3]
        qber_list.append(qber_i)

    twofolds = sum(twofolds_list)
    qber = sum(qber_list) / twofolds if twofolds > 0 else 0

    if qber > 0:
        H2 = -qber * log2(qber) - (1 - qber) * log2(1 - qber)
    else:
        H2 = 0

    f_e = f_ec + qber
    skr = -1.0 * real(twofolds * 0.5 * (1 - (1 + f_e) * H2))
```

```
    return [skr, qber, twofolds]
```

To maximize the secure key rate, we optimize the squeezing parameter χ for every channel loss setting using a SLSQP algorithm.

Listing A.3: Optimization of squeezing parameter to maximize secure key rate

```
def Par_funct(x):
    loss_a = 10**(-x / 10.0)
    loss_b = 10**(-x / 10.0)
    Param = [loss_a, loss_b, n_factor_a, n_factor_b, dim, tau]

    bounds = [(0.0, 1.0)]  # Bounds on squeezing parameter
    chi_init = [chi]
    options = {'disp': True, 'maxiter': 10000, 'ftol': 1e-30}
    constraints = {'type': 'ineq', 'fun': Constraint3}

    # Optimize squeezing parameter
    result = opt.minimize(
        simqkdentanglement,
        chi_init,
        method='SLSQP',
        args=Param,
        bounds=bounds,
        constraints=constraints,
        options=options
    )
    # Evaluate metrics at optimum
    [skr] = simqkdentanglement(result.x, Param)
    [qber, twofolds] =
    simqkdentanglement(result.x, Param, return_stats=True)
    skr_final = -skr / coinc_window
    qber_final = qber * 100
    [opt_chi] = result.x

    return [skr_final, qber_final, opt_chi]
```

Appendix B

Joint Spectral Intensity Simulation

The JSI simulation is based on a phase matching code for spontaneous parametric down-conversion written by Sungeun Oh [309], where the Sellmeier coefficients are calculated from [5]. The pump ranges correspond to the pump wavelength channels considered in Sec. 3.4.2. To calculate the cross-talk we calculate the overlap between each individual (corresponding to a single pump channel) JSI.

Listing B.1: Joint spectral intensity simulation code

```
close all;
PumpRanges = [ 521.5 521.75; 522 522.25; 521 521.25; 520.5 520.75];
ReferencePumps = mean(PumpRanges, 2);
lambda_s_vals = linspace(780, 795, 200);
lambda_i_vals = linspace(1520,1570, 200);
[LambdaSGrid, LambdaIGrid] = meshgrid(lambda_s_vals, lambda_i_vals);
CombinedJSI = zeros(size(LambdaSGrid));

for idx = 1:size(PumpRanges, 1)
    PumpRangeFrom = PumpRanges(idx, 1);
    PumpRangeTo   = PumpRanges(idx, 2);
    ReferencePump = ReferencePumps(idx);

    % Constants and parameters
    IncrementDecimal=2;
    PumpPlotTickSize=10^IncrementDecimal;
    ReferenceSignal=785;
```

```
WavelengthEnd=2000;
AcceptableVisibility=0.995;
PumpLinewidth=276000; % MHz
OpticAxisAngle=pi/4;
CrystalLength=15; % mm
PolingPeriod=7.1157; % um
CrystalTemperature=45; (Celsius)
ContourSignalStart=750;
ContourSignalEnd=850;
coef_factor=10^(-6);
cLight=299792458;
cLightCONV=cLight/coef_factor;

% Allocate arrays
NumPoints =
round((PumpRangeTo - PumpRangeFrom) * PumpPlotTickSize + 1);
ArraySignal = zeros(NumPoints, 1);
ArrayIdler = zeros(NumPoints, 1);
ArraySignalBW = zeros(NumPoints, 1);
ArrayIdlerBW = zeros(NumPoints, 1);

% Sellmeier coefficients
a1z=5.756; a2z=0.0983; a3z=0.2020; a4z=189.32; a5z=12.52; a6z=1.32e-2;
b1z=2.860e-6; b2z=4.700e-8; b3z=6.113e-8; b4z=1.516e-4;
ThermalExp1=1.54e-5; ThermalExp2=5.3e-9;

% Assign coefficients
Coa1=a1z; Coa2=a2z; Coa3=a3z; Coa4=a4z; Coa5=a5z; Coa6=a6z;
Cob1=b1z; Cob2=b2z; Cob3=b3z; Cob4=b4z;
Cea1=a1z; Cea2=a2z; Cea3=a3z; Cea4=a4z; Cea5=a5z; Cea6=a6z;
Ceb1=b1z; Ceb2=b2z; Ceb3=b3z; Ceb4=b4z;
CTemperature = CrystalTemperature + 273.15;
CTempEff = (CTemperature - 297.66) * (CTemperature + 570.82);

for n = 1:NumPoints
    Pump = (n + PumpRangeFrom*PumpPlotTickSize - 1) / PumpPlotTickSize;
    PumpLambda = Pump * 1e-9;
    PumpLambdaCONV = PumpLambda / coef_factor;
```

```
    % Compute refractive index
    neCPump = sqrt(Cea1 + Ceb1*CTempEff + ...
        (Cea2 + Ceb2*CTempEff)./((PumpLambdaCONV.^2)
        -(Cea3 + Ceb3*CTempEff)^2) + ...
        (Cea4 + Ceb4*CTempEff)./((PumpLambdaCONV.^2)-Cea5^2) - ...
        Cea6*PumpLambdaCONV.^2);

    % Signal and idler computations omitted here for brevity...
    % Assume FinalSignal, FinalIdler, SignalBW, IdlerBW are obtained

    % Store results
    ArraySignal(n) = FinalSignal;
    ArrayIdler(n) = FinalIdler;
    ArraySignalBW(n) = abs(SignalBW);
    ArrayIdlerBW(n) = abs(IdlerBW);
    fprintf('%d nm done\n', Pump);
end

% Plot JSI contributions
for i = 1:length(ArraySignal)
    lambda_s = ArraySignal(i);
    lambda_i = ArrayIdler(i);
    sigma_s = ArraySignalBW(i) * 1e9 / 2.3548;
    sigma_i = ArrayIdlerBW(i) * 1e9 / 2.3548;
    rho = -0.91;

    if
    isnan(lambda_s) || isnan(lambda_i) || sigma_s <= 0 || sigma_i <= 0
        continue;
    end

    X = LambdaSGrid - lambda_s;
    Y = LambdaIGrid - lambda_i;
    exponent = -1 / (2 * (1 - rho^2)) * ...
        ((X.^2 / sigma_s^2) + (Y.^2 / sigma_i^2) - ...
        (2 * rho * X .* Y) / (sigma_s * sigma_i));
```

```
            CombinedJSI = CombinedJSI + exp(exponent);
        end
    end
```

Appendix C

Interferometric demultiplexing

C.1 MZI frequency demultiplexing

An unbalanced MZI can be described by two beam-splitters and a phase shifter corresponding to the OPL difference. In this Appendix, we derive the interferometric condition for frequency demultiplexing. The unitary can thus be described as $\hat{BS}\hat{P}\hat{BS}$, where $\hat{BS}$ is the beam-splitter operator and $\hat{P}$ is the phase shifter operator. More specifically, for a 50-50 beam-splitter

$$\hat{BS} == \frac{1}{\sqrt{2}}\begin{pmatrix} 1 & i \\ i & 1 \end{pmatrix}$$

we can also represent the phase shifter as

$$\hat{P} = \begin{pmatrix} e^{ik\Delta L} & 0 \\ 0 & 1 \end{pmatrix}$$

where $k = \omega/c$ is the wave vector and ΔL is the OPL difference of the unbalanced MZI. The overall unitary associated to the MZI is thus given by

$$\hat{MZI} = \frac{1}{2}\begin{pmatrix} 1 & i \\ i & 1 \end{pmatrix}\begin{pmatrix} e^{iK\Delta L} & 0 \\ 0 & 1 \end{pmatrix}\begin{pmatrix} 1 & i \\ i & 1 \end{pmatrix} = \begin{pmatrix} e^{ik\Delta L}+i & ie^{ik\Delta L}+1 \\ ie^{ik\Delta L}+1 & -e^{ik\Delta L}+i \end{pmatrix}$$

Let us denote the input ports of the MZI as 1 and 2 and the outputs as 3 and 4 and the respective amplitude at each port as A_i. Suppose $A_1 = 1$ and $A_2 = 0$, then

$$\begin{pmatrix} A_3 \\ A_4 \end{pmatrix} = \hat{MZI}\begin{pmatrix} 1 \\ 0 \end{pmatrix} = \frac{1}{2}\begin{pmatrix} e^{ik\Delta L}+i \\ ie^{ik\Delta L}+1 \end{pmatrix}$$

From coupled-wave theory, we recall that The MZI's transmittances are then given from coupled-wave theory as [290]:

$$T_{1\to 3} = \left|\frac{e^{ik\Delta L}+i}{2}\right|^2 = \frac{1+\cos(k\Delta L)}{2} = \cos^2\left(\frac{k\Delta L}{2}\right)$$

$$T_{1\to 4} = \left|\frac{ie^{ik\Delta L}+1}{2}\right|^2 = \frac{1-\cos(k\Delta L)}{2} = \sin^2\left(\frac{k\Delta L}{2}\right).$$

For the MZI to act as a frequency demultiplexer for ω_1 and ω_2 we require

$$\cos^2(k_i\Delta L/2) = \begin{cases} = 1 & \text{for} \quad \omega_i = \omega_1 \\ = 0 & \text{for} \quad \omega_i = \omega_2 \end{cases}$$

we can rewrite this condition as

$$(\frac{\omega_1\Delta L}{2c} - \frac{\omega_2\Delta L}{2c}) = n\pi/2,$$

where n is an odd integer. Taking $n = 1$, we obtain Eq. 4.2.

Appendix D

Frequency-bin post-processing (prepare-and-measure scheme)

For the rectilinear basis, we simply create a histogram of the detection events for the detectors D0 and D1 associated to projections $|\omega_0\rangle\langle\omega_0|$ and $|\omega_1\rangle\langle\omega_1|$.

Listing D.1: Analysis code for the rectilinear frequency-bin basis

```
import matplotlib.pyplot as plt
import numpy as np

hist, bin_edges = np.histogram(df1, bins=5000)
# df1 corresponds to the dataframe for detector 0
hist2, bin_edges2 = np.histogram(df8, bins=5000)
# df8 corresponds to the dataframe for detector 1

plt.subplot(3, 1, 2)
plt.scatter(78 * bin_edges[:-1] / 1e12, hist, s=1, color='red')
# 78 ps is the resolution of our time-tagging unit
plt.plot(78 * bin_edges[:-1] / 1e12, hist, color='red', linewidth=0.5)
plt.title('Detector 0')
plt.ylabel('Counts')
plt.xlim([0, 5])
plt.ylim([0, 350])

plt.subplot(3, 1, 3)
```

```
plt.scatter(78 * bin_edges2[:-1] / 1e12, hist2, color='orange', s=1)
plt.plot(78 * bin_edges2[:-1] / 1e12, hist2, color='orange', linewidth=0.5)
plt.title('Detector 1')
plt.ylim([0, 350])
plt.xlim([0, 5])
plt.ylabel('Counts')
plt.xlabel('Time (s)')

t = np.linspace(0, 6, 1000)
shutter_offset = -0.07

shutter1 = (np.sin(2 * np.pi * (t - shutter_offset)) > 0).astype(int)
# Shutter 1 opens and closes
shutter2 = (
    np.sin(2 * np.pi * (t - shutter_offset) - np.pi / 2) > 0
).astype(int)
# Shutter 2 phase-shifted by pi/2

plt.subplot(3, 1, 1)
plt.plot(
    t, shutter1,
    label="Shutter 0",
    drawstyle='steps-post',
    color='red'
)
plt.plot(
    t, shutter2,
    label="Shutter 1",
    drawstyle='steps-post',
    color='orange'
)
plt.fill_between(
    t, 0, shutter1 & ~shutter2,
    color='red',
    step='post',
    alpha=0.5,
    label=r"$|\omega_0\rangle$"
)
```

```
plt.fill_between(
    t, 0, shutter2 & ~shutter1,
    color='orange',
    step='post',
    alpha=0.5,
    label=r"$|\omega_1\rangle$"
)
plt.fill_between(
    t, 0, shutter1 & shutter2,
    color='grey',
    step='post',
    alpha=0.5,
    label=
    r"$\frac{1}{\sqrt{2}}(|\omega_0\rangle
+e^{i\phi(t)}|\omega_1\rangle)$"
)

plt.title('Shutters')
plt.xlim([0, 5])
plt.yticks([0, 1], labels=['Closed', 'Open'])
plt.tight_layout()
plt.show()
```

For the superposition basis, we start by referencing each detection event (df1) to the last synchronization marker (df7) as outlined in Eq. 4.7. We then apply a modulo of 49.235 time-tag units (each time-tag unit is equal to 78.125 ps) corresponding to the period of the 260 MHz beat note and generate a histogram as outlined in Eqs. 4.8-4.10.

Listing D.2: Analysis code for the superposition frequency-bin basis

```
time_diffs = []
for idx, row in df1.iterrows():
# Find the maximum timestamp in df7 that is less than or equal
#to the current timestamp in df1
    max_previous_timestamp =
    df7[df7['timestamp'] <= row['timestamp']]['timestamp'].max()

    # Calculate the time difference
    if pd.notnull(max_previous_timestamp):
```

```
            time_diff = row['timestamp'] - max_previous_timestamp
            time_diffs.append(time_diff)
        else:
            time_diffs.append(None)

df1['time_since_last_click_df7'] = time_diffs

print(df1)
third_column1 = df1.iloc[:, 2]
x =  49.235
time_elements1 = [num for num in third_column1]
result1 = [num % x for num in time_elements1]

fifth_column1 = np.array([])
for element in result1:
    if element <= 49 * y:
        fifth_column1 = np.append(fifth_column1, element)

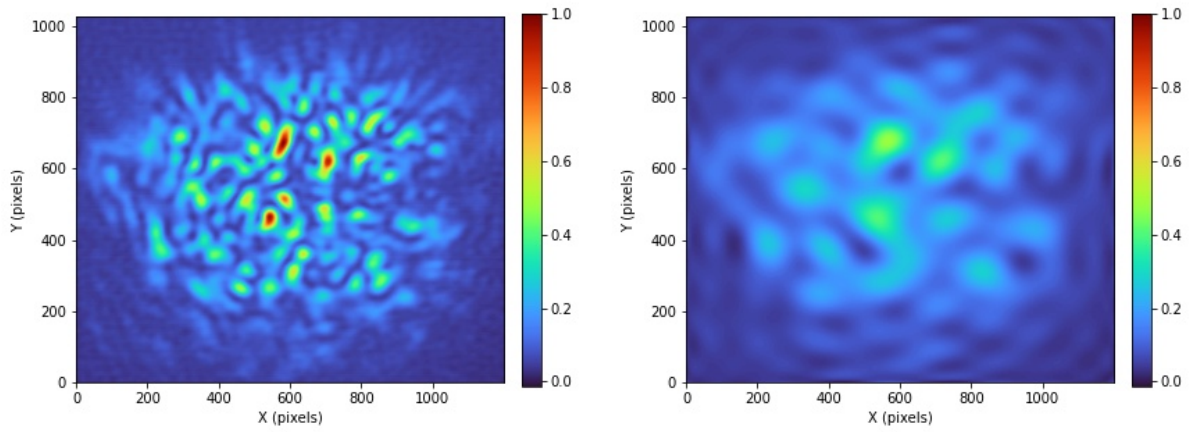
hist, bin_edges = np.histogram(fifth_column1, bins=49 * y)
modified_bin_edges = 78.125 * bin_edges

plt.bar(
    modified_bin_edges[:-1],
    hist,
    width=np.diff(modified_bin_edges),
    align='edge'
)
plt.xlim([0, 49 * y * 78.125])
plt.ylim([0, None])
plt.ylabel('Counts')
plt.xlabel('Time (ps)')
plt.show()
```

Appendix E

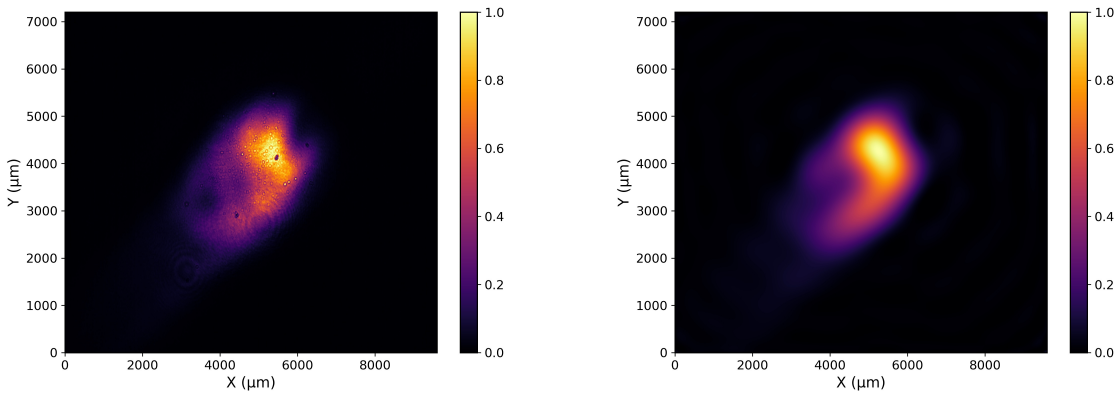
Estimation of multi-mode characteristics

To characterize the modal expansion at the receiver in both chapters 4 and 5, we first filter the point spread function (PSF) using a Fast Fourier Transform (FFT) and retaining only the dominant spatial frequency components. The PSF is then reconstructed in Fig. E.1b (Fig. E.2b) from its modal decomposition into the first 100 (30) Hermite-Gaussian modes for the beam profile in chapter 4 (5). The large number of modes required to accurately reconstruct the PSF reflects the highly multi-mode nature of the beam.



(a) Original PSF (b) Reconstructed PSF

Figure E.1: (a) Image, captured with a beam-profiling camera (WinCamD-UCD12), of the multi-mode beam in the analyzer in Fig. 4.10, after propagation through 2 meters of free space and a 1-meter long step-index multi-mode fiber (Thorlabs M43L01). (b) Reconstruction of the point spread function from modal decomposition using the first 100 Hermite-Gaussian modes. Each pixel corresponds to 5.2μm.



(a) Original PSF

(b) Reconstructed PSF

Figure E.2: (a) Point spread function, imaged with a beam-profiling camera (*New Imaging Technologies WiDy SenS 640*), of the multi-mode beam in the analyzer in Fig. 5.3, after propagation through a 5-meter long graded-index (GRIN) multi-mode fibre (*Thorlabs GIF625*). (b) Reconstruction of the point spread function from modal decomposition using the first 30 Hermite-Gaussian modes.

E.0.1 Modal decomposition analysis code

The analysis code for the modal decomposition is provided below. Note that while we chose Hermite-Gaussian modes, the analysis framework supports the decomposition of the PSF into any orthonormal spatial mode basis. Prior to this step, we filter the PSF to retain only the dominant spatial frequencies with amplitude above a given threshold relative to the maximum spatial frequency. This filtering is implemented using the `numpy.fft` package to compute the two-dimensional Fourier transform of the PSF.

Listing E.1: Hermite-Gaussian Mode Decomposition

```
import numpy as np
import matplotlib.pyplot as plt
import scipy.sparse.linalg as spla
import pandas as pd
import time
from scipy.special import eval_hermite
```

```
file_path = "WinCamExcelData2.csv" # load data file
df = pd.read_csv(file_path, skiprows=3, header=None)
psf = df.apply(pd.to_numeric, errors='coerce').values
psf = np.nan_to_num(psf, nan=0.0, posinf=0.0, neginf=0.0)
h, w = psf.shape

max_mode = 100  # number of modes considered in the modal decomposition
w0 = 1.0 # beam waist computed from a Gaussian fit of the beam profile

def hermite_gaussian(x, n, w0):
    norm = 1 / np.sqrt(2**n * np.math.factorial(n) * np.sqrt(np.pi) * w0)
    return norm * eval_hermite(n, np.sqrt(2) * x / w0)
                    * np.exp(-x**2 / w0**2)

def compute_mode(m, n, w0):
    x = np.linspace(-1, 1, w)
    y = np.linspace(-1, 1, h)
    mode = np.outer(
    hermite_gaussian(x, m, w0),
    hermite_gaussian(y, n, w0)
).T
    return mode.ravel()

def optimize_mode_coeffs_v2(psf, max_mode=max_mode, w0=w0):
    b = psf.ravel()
    num_modes = max_mode**2

    def mv(x):
        result = np.zeros_like(b)
        count = 0
        for m in range(max_mode):
            for n in range(max_mode):
                mode = compute_mode(m, n, w0)
                result += x[count] * mode
                count += 1
        return result

    def rmv(x):
```

```
        result = np.zeros(num_modes)
        count = 0
        for m in range(max_mode):
            for n in range(max_mode):
                mode = compute_mode(m, n, w0)
                result[count] = np.dot(x, mode)
                count += 1
        return result

    # We use a least square solver to find the mode coefficients
    start_time = time.time()
    A = spla.LinearOperator(
    (b.size, num_modes),
    matvec=mv,
    rmatvec=rmv,
    dtype=np.float64
    )
    coeffs, *_ = spla.lsmr(A, b)
    elapsed_time = time.time() - start_time
    print(f"Optimization Time: {elapsed_time:.2f} seconds")

    mode_keys = [(m, n) for m in range(max_mode) for n in range(max_mode)]
    return {mode_keys[i]: coeffs[i] for i in range(len(mode_keys))}

def reconstruct_psf_v2(optimized_coeffs, max_mode, w0):
    reconstructed = np.zeros(h * w)
    count = 0
    for m in range(max_mode):
        for n in range(max_mode):
            mode = compute_mode(m, n, w0)
            reconstructed += optimized_coeffs[(m, n)] * mode
            count += 1
    return reconstructed.reshape((h, w))
```

Appendix F

Frequency-bin post-processing (entanglement-based scheme)

The full analysis code is provided in [298]. We here highlight some relevant sections.

Listing F.1: Antidiagonal correction due to the exponential decay

```
import numba
#H here is the histogram matrix of the previously computed JTA
@numba.jit(nopython=True)
def create_correction_matrix_antidiagonal(
        shape, step_size, a, b, c, max_correction):
    correction = np.ones(shape)
    rows, cols = shape
    diagonal_value = a + c

    # compute correction factors based on antidiagonal distance
    for i in range(rows):
        for j in range(cols):
            if i != j:
                dt = (j - i) * step_size
                response = a * np.exp(-b * np.abs(dt)) + c
                if response > 0.05 * diagonal_value:
                    corr_factor = diagonal_value / response
                    correction[i, j] = min(corr_factor, max_correction)
```

```
    for k in range(-(rows - 1), cols):
        antidiag_indices = []
        for i in range(rows):
            j = k + i
            if 0 <= j < cols:
                antidiag_indices.append((i, j))

        if not antidiag_indices:
            continue

        max_corrected_value = 0.0
        for i, j in antidiag_indices:
            potential_value = H[i, j] * correction[i, j]
            if potential_value > max_corrected_value:
                max_corrected_value = potential_value

        max_diag_value = 0.0
        for i, j in antidiag_indices:
            if H[i, i] > max_diag_value:
                max_diag_value = H[i, i]
            if j < rows and H[j, j] > max_diag_value:
                max_diag_value = H[j, j]

        if (max_corrected_value > max_diag_value and
        max_corrected_value > 0):
            scale_factor = max_diag_value / max_corrected_value
            for i, j in antidiag_indices:
                correction[i, j] *= scale_factor

    return correction
```

After accounting for the $e^{-\gamma|t_s-t_i|}$ decay from the cavity lifetime, we compute the projections $|P_{s,i}(t_s,t_i)\rangle\langle P_{s,i}(t_s,t_i)|$. To help visualize these projections, we shown overlaid a subsection of the joint temporal amplitude (JTA) depicted in Fig. F.1. Each colored square represents a specific equatorial basis used in the quantum state tomography in Sec. 5.4.1. Although only one dashed square per color is shown in the figure for clarity, the corresponding projectors are periodically applied throughout the JTA to improve the collected statistics. As an example, in the code given below, we calculate the expectation values for

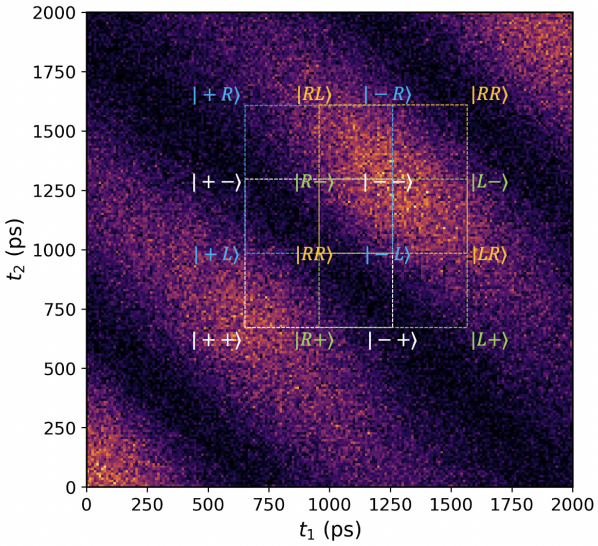


Figure F.1: Conceptual representation of the projectors defined in Eq. 5.3 shown overlaid on a subsection the joint temporal amplitude (JTA) in Fig. 5.6b for illustrative purposes. Each color defines a different equatorial basis considered for the quantum state tomography.

the four bases depicted in Fig. F.1 ($\langle XX\rangle, \langle XY\rangle, \langle YX\rangle, \langle YY\rangle$).

Listing F.2: Projections and expectation values for the equatorial bases depicted in Fig. F.1

```
P = 61  # periodicity in number of bins
Delta = int(np.floor(P / 2))
Del = int(np.floor(Delta / 2))
XX_list, XY_list, YX_list, YY_list = [], [], [], []
XX_err, YY_err, XY_err, YX_err = [], [], [], []

for x in range(P):
    selected_indices = range(x, len(diag), P * 2)
    pp_values, mm_values = [], []

    for i in selected_indices:
        if (i + Del < H_corrected.shape[1] and
            i + P < H_corrected.shape[0] and
            i + P + Del < H_corrected.shape[1]):
```

```
            pp_values.append(H_corrected[i, i + Del])
            mm_values.append(H_corrected[i + P, i + P + Del])

pp = np.sum(pp_values)
mm = np.sum(mm_values)
total_sum = pp + mm

pm_values, mp_values = [], []
for i in selected_indices:
    if (i + Del < H_corrected.shape[1] and
            i + P < H_corrected.shape[0] and
            i + P + Del < H_corrected.shape[1]):
            pm_values.append(H_corrected[i + P, i + Del])
            mp_values.append(H_corrected[i, i + P + Del])

pm_sum = np.sum(pm_values)
mp_sum = np.sum(mp_values)

S = total_sum
C = pm_sum + mp_sum
numerator = S - C
denominator = S + C

if denominator > 0:
    V = numerator / denominator
sigma_V = (1 / denominator) * np.sqrt(
    abs(numerator) + (numerator**2) / denominator
)
else:
    V, sigma_V = 0, 0

XX_list.append(V)
XX_err.append(sigma_V)

# XY and YX terms
pL_values3, mR_values3 = [], []
for i in selected_indices:
    if (i + Del < H_corrected.shape[1] and
```

```
            i + P < H_corrected.shape[0] and
            i + P + Del + Delta < H_corrected.shape[1]):
            pL_values3.append(H_corrected[i, i + Delta + Del])
            mR_values3.append(H_corrected[i + P, i + Delta + Del + P])

    pR_values3, mL_values3 = [], []
    for i in selected_indices:
        if (i + Del < H_corrected.shape[1] and
            i + P < H_corrected.shape[0] and
            i + P + Del + Delta < H_corrected.shape[1]):
            pR_values3.append(H_corrected[i + Delta + Del + P, i])
            mL_values3.append(H_corrected[i + Delta + Del, i + P])

    Rp_values2, Lm_values2 = [], []
    for i in selected_indices:
        if (i + Del < H_corrected.shape[1] and
            i + P < H_corrected.shape[0] and
            i + P + Del + Delta < H_corrected.shape[1]):
            Rp_values2.append(H_corrected[i + Delta, i + Delta + Del])
            Lm_values2.append(
            H_corrected[i + Delta + P, i + Delta + Del + P]
            )

    Rm_values2, Lp_values2 = [], []
    for i in selected_indices:
        if (i + Del < H_corrected.shape[1] and
            i + P < H_corrected.shape[0] and
            i + P + Del + Delta < H_corrected.shape[1]):
            Rm_values2.append(H_corrected[i + Delta + P, i + Delta + Del])
            Lp_values2.append(H_corrected[i + Delta + P, i + Delta + Del])

    # XY
    S3 = np.sum(pL_values3) + np.sum(mR_values3)
    C3 = np.sum(pR_values3) + np.sum(mL_values3)
    numerator3 = S3 - C3
    denominator3 = S3 + C3

    if denominator3 > 0:
```

```
    V3 = numerator3 / denominator3
    sigma_V3 = (1 / denominator3) * np.sqrt(
abs(numerator3) + (numerator3**2) / denominator3
)
else:
    V3, sigma_V3 = 0, 0

XY_list.append(V3)
XY_err.append(sigma_V3)

# YX
S2 = np.sum(Rp_values2) + np.sum(Lm_values2)
C2 = np.sum(Rm_values2) + np.sum(Lp_values2)
numerator2 = S2 - C2
denominator2 = S2 + C2

if denominator2 > 0:
    V2 = numerator2 / denominator2
     sigma_V2 = (1 / denominator2) * np.sqrt(
abs(numerator2) + (numerator2**2) / denominator2
)
else:
    V2, sigma_V2 = 0, 0

YX_list.append(V2)
YX_err.append(sigma_V2)

# YY
RR_values, LL_values = [], []
for i in selected_indices:
    if (
        i + 3 * Delta < H_corrected.shape[0] and
        i + Delta < H_corrected.shape[0]
    ):
        RR_values.append(H_corrected[i + Delta, i + Del])
        LL_values.append(H_corrected[i + Delta + P, i + Del + P])

RL_values, LR_values = [], []
```

```
for i in selected_indices:
    if (
        i + 3 * Delta < H_corrected.shape[0] and
        i + Delta < H_corrected.shape[0]
    ):
        RL_values.append(H_corrected[i + Delta, i + Del + P])
        LR_values.append(H_corrected[i + Del + P, i + Delta])

S4 = np.sum(RR_values) + np.sum(LL_values)
C4 = np.sum(RL_values) + np.sum(LR_values)
numerator4 = S4 - C4
denominator4 = S4 + C4

if denominator4 > 0:
   V4 = numerator4 / denominator4
     sigma_V4= (1 / denominator4) * np.sqrt(
abs(numerator4) + (numerator4**2) / denominator4
)
else:
    V4, sigma_V4 = 0, 0

YY_list.append(V4)
YY_err.append(sigma_V4)
```